University of Kentucky
UKnowledge

Theses and Dissertations--Chemical and Materials Engineering

Chemical and Materials Engineering

2014

The Development and Biocompatibility of Low Temperature Co-Fired Ceramic (LTCC) for Microfluidic and Biosensor Applications

Jin Luo
University of Kentucky, jlu227@uky.edu

Right click to open a feedback form in a new tab to let us know how this document benefits you.

Recommended Citation

Luo, Jin, "The Development and Biocompatibility of Low Temperature Co-Fired Ceramic (LTCC) for Microfluidic and Biosensor Applications" (2014). *Theses and Dissertations--Chemical and Materials Engineering*. 30.
https://uknowledge.uky.edu/cme_etds/30

This Doctoral Dissertation is brought to you for free and open access by the Chemical and Materials Engineering at UKnowledge. It has been accepted for inclusion in Theses and Dissertations--Chemical and Materials Engineering by an authorized administrator of UKnowledge. For more information, please contact UKnowledge@lsv.uky.edu.

STUDENT AGREEMENT:

I represent that my thesis or dissertation and abstract are my original work. Proper attribution has been given to all outside sources. I understand that I am solely responsible for obtaining any needed copyright permissions. I have obtained needed written permission statement(s) from the owner(s) of each third-party copyrighted matter to be included in my work, allowing electronic distribution (if such use is not permitted by the fair use doctrine) which will be submitted to UKnowledge as Additional File.

I hereby grant to The University of Kentucky and its agents the irrevocable, non-exclusive, and royalty-free license to archive and make accessible my work in whole or in part in all forms of media, now or hereafter known. I agree that the document mentioned above may be made available immediately for worldwide access unless an embargo applies.

I retain all other ownership rights to the copyright of my work. I also retain the right to use in future works (such as articles or books) all or part of my work. I understand that I am free to register the copyright to my work.

REVIEW, APPROVAL AND ACCEPTANCE

The document mentioned above has been reviewed and accepted by the student's advisor, on behalf of the advisory committee, and by the Director of Graduate Studies (DGS), on behalf of the program; we verify that this is the final, approved version of the student's thesis including all changes required by the advisory committee. The undersigned agree to abide by the statements above.

Jin Luo, Student

Dr. Richard Eitel, Major Professor

Dr. Thomas Dziubla, Director of Graduate Studies

THE DEVELOPMENT AND BIOCOMPATIBILITY OF LOW TEMPERATURE CO-FIRED CERAMIC (LTCC) FOR MICROFLUIDIC AND BIOSENSOR APPLICATIONS

DISSERTATION

A dissertation submitted in partial fulfillment of the
requirements for the degree of Doctor of Philosophy in the
College of Engineering
at the University of Kentucky

By
Jin Luo
Lexington, Kentucky

Director: Dr. Richard E. Eitel, Professor of Department of Chemical and Materials Engineering

Lexington, Kentucky
2014

Copyright © Jin Luo 2014

ABSTRACT OF DISSERTATION

THE DEVELOPMENT AND BIOCOMPATIBILITY OF LOW TEMPERATURE CO-FIRED CERAMIC (LTCC) FOR MICROFLUIDIC AND BIOSENSOR APPLICATIONS

Low temperature co-fired ceramic (LTCC) electronic packaging materials are applied for their electrical and mechanical properties, high reliability, chemical stability and ease of fabrication. Three dimensional features can also be prepared allowing integration of microfluidic channels and cavities inside LTCC modules. Mechanical, optical, electrical, microfluidic functions have been realized in single LTCC modules. For these reasons LTCC is attractive for biomedical microfluidics and Lab-on-a-Chip systems. However, commercial LTCC systems, optimized for microelectrics applications, have unknown cytocompatibility, and are not compatible with common surface functionalization chemistries.

The first goal of this work is to develop biocompatible LTCC materials for biomedical applications. In the current work, two different biocompatible LTCC substrate materials are conceived, formulated and evaluated. Both materials are based from well-known and widely utilized biocompatible materials. The biocompatibilities of the developed LTCC materials for *in-vitro* applications are studied by cytotoxicity assays, including culturing endothelial cells (EC) both in LTCC leachate and directly on the LTCC substrates. The results demonstrate the developed LTCC materials are biocompatible for *in-vitro* biological applications involving EC.

The second goal of this work is to develop functional capabilities in LTCC microfluidic systems suitable for *in-vitro* and biomedical applications. One proposed application is the evaluation of oxygen tension and oxidative stress in perfusion cell culture and bioreactors. A Clark-type oxygen sensor is successfully integrated with LTCC technique in this work. In the current work, a solid state proton conductive electrolyte is used to integrate an oxygen sensor into the LTCC. The measurement of oxygen concentration in Clark-type oxygen sensor is based on the electrochemical reaction between working electrode and counter electrode. Cyclic voltammetry and

chronoamperometry are measured to determine the electrochemical properties of oxygen reduction in the LTCC based oxygen sensor. The reduction current showed a linear relationship with oxygen concentration. In addition, LTCC sensor exhibits rapid response and sensitivity in the physiological range 1─9 mg/L. The fabricated devices have the capabilities to regulate oxygen supply and determination of local dissolved oxygen concentration in the proposed applications including perfusion cell culture and biological assays.

KEY WORDS: Low temperature co-fired ceramics (LTCC), Oxygen sensor,

Microfluidic, Biocompatibility, Electrochemistry

Jin Luo

Student's signature

April 16, 2014

Date:

THE DEVELOPMENT AND BIOCOMPATIBILITY OF LOW TMEPERATURE CO-FIRED CERAMIC (LTCC) FOR MICROFLUIDIC AND BIOSENSOR APPLICAITONS

By

Jin Luo

Dr. Richard E. Eitel
Director of Dissertation

Dr. Thomas Dziubla
Director of Graduate Studies

April 16, 2014
Date

ACKNOWLEDGMENTS

First and foremost, I want to express my deepest gratitude to my advisor Dr. Eitel for his guidance and support in my research during the entire life at University of Kentucky. I thank him for training me how to think and how to develop critical skills in the research. I especially thank him for kindly encouragement whenever I encounter difficulties in the research. I am also grateful to Dr. Eitel for providing various opportunities to attend conferences.

I would like to thank my committee members, Dr. Kimberly Anderson, Dr. Thomas Dziubla, Dr. Bruce Hinds and Dr. Christine Trinkle for their precious time to attend my dissertation defense. I thank Dr. Kimberly Anderson and Dr. Thomas Dziubla for providing experimental guidance and resources in biocompatibility study. I want to thank Dr. Kimberly Anderson, Dr. Thomas Dziubla and Dr. Bruce Hinds for being the committee members from the beginning and attending the dissertation defense at the very end. I'd like to thank Dr. Bruce Hinds for his service as the committee chair for my doctoral defense. I also want to acknowledge Dr. Christine Trinkle for the effort to serve in my defense.

I especially thank Dr. Yang-Tse Cheng for providing experimental guidance and resources in electrochemical testing. I thank him for taking me into his group and supervising me to finish my research in the last year of my Ph.D study. I also like to thank him for providing helpful advice on many aspects of my research and kindly

encouragement when I was frustrated with the research. I also would like to thank Jiagang Xu, Jie Pan, Qinglin Zhang and Hoffmann Ilona for helping with electrochemical measurement. I really enjoy the study life with them.

I would like to acknowledge my group members at University of Kentucky, Dr. Wenli Zhang and Dr. Serhiy Leontsev in Dr. Eitel lab. I thank them for helping me get familiar with the instruments in the lab. I am very grateful to Dr. Wenli Zhang for sharing his knowledge, experience, unreserved support and assistance when I started my research. I also want to thank Dr. Wenli Zhang for helping me get used to the life in Lexington. I also want to thank Mr. Brian M. Ray for his help in the lab.

I also like to thank William Mercke, David Cochran, Jennifer Fischer and Samantha Meenach, Matt Dickerson, and Jacob Lilly for helping with cell culture experiments. Thanks a lot to William Mercke and Matt Dickerson for training me how to culture cells at the beginning. Thanks to William Mercke for useful discussions and sharing cells with me.

I would like to add my special thanks to Dr. Fuqian Yang for his constant support, guidance and encouragement in my research especially in the last year of my Ph.D life.

I would like to thank the colleagues and friends at UK for their helps and friendship, Dr. Xin Zhan, Mr. Nicolas Briot, Dr. Wei Wen, Dr. Lei Wang, Mr. Zhiqiang Chen, Ms. Xu Jiang, Mrs. Yuan Lu, Mrs. Prachi Gupta, Mr. Paritosh Wattamwar, Mr. Juchuan Li, Mr. Phillip Swartzentruber, Mr. Guangfeng Zhao, Ms. Ruo He, Mr. Jia Ye, Mr. Dali Qian, Mr. Jerry Vice, Ms. Nancy Miller and Mrs. Chelsea Hansing. I have a wonderful Ph.D life at the University of Kentucky with them as company.

I would like to appreciate the financial support from DEPSCOR/ONR and University of Kentucky Center for Clinical and Translational Science (CTSA).

I would like to give my deepest thanks to my husband, my parents and my brother for their endless love, support and encouragement.

Table of Contents

ACKNOWLEDGMENTS iii
Table of Contents vi
List of Tables viii
List of Figures ix
Chapter 1 Introduction 1
1.1 Motivation 1
1.2 Organization of the thesis 4
Chapter 2 Background 7
2.1 Low temperature co-fired ceramics (LTCC) 7
2.1.1 LTCC materials 7
2.1.2 LTCC processing 11
2.1.3. Applications of LTCC based microfluidic system 12
2.2 Ceramic sintering theory 17
2.2.1 Solid state sintering 17
2.2.2 Liquid state sintering 22
2.2.3 Viscous sintering 28
2.2.4 Non-reactive liquid phase sintering 30
2.3 Oxygen sensing for biological and microfluidic applications 34
2.3.1 Luminescent oxygen sensor 35
2.3.2 Electrochemical amperometric sensing: Fundamentals of electrochemistry 41
2.3.3 Electrochemical sensing: Clark-type oxygen sensor 53
Chapter 3 A biocompatible low temperature co-fired ceramic substrate for biosensors 64
3.1 Introduction 64
3.2 Tape casting technique 66
3.3 Biocompatibility of the materials 70
3.4 Experimental Procedure 71
3.4.1 LTCC fabrication and sintering 71
3.4.2 Biocompatibility 73
3.5 Results and discussion 75
3.5.1 LTCC fabrication and sintering 75
3.5.2 Biocompatibility 82
3.6 Conclusion 86
Chaper 4 Sintering behavior and biocompatibility of a low temperature co-fired ceramic for microfluidic biosensors 87
4.1 Introduction: 87
4.2 Master sintering curve 91
4.3 Experimental: 96
4.3.1 LTCC fabrication and sintering 96
4.3.2 Master Sintering Curve Analysis: 98
4.3.3 Microstructure and Co-firing with electrode 99
4.3.4 Biocompatibility: Cytotoxicity assay of LTCC leachate 99
4.3.5 Biocompatibility: Endothelial cell adhesion and growth 101

4.4 Results and discussion: 102
4.4.1 LTCC fabrication and sintering 102
4.4.2 Mater sintering curve study 104
4.4.3 Microstructure of LTCC and Co-firing with electrode 108
4.4.4 Biocompatibility: Cytotoxicity of LTCC leachate 114
4.4.5 Biocompatibility: Endothelial cell adhesion and growth 116
4.5 Conclusion 118
Chapter 5 A low temperature co-fired ceramic (LTCC) microfluidic Clark-type oxygen sensor for real-time oxygen sensing 120
5.1 Introduction 120
5.2 Sintering of LTCC: Self-constrained sintering 123
5.3 Experimental: 124
5.3.1 Geometry and design of microfluidic flow cell incorporating Clark-type electrodes 124
5.3.2 Fabrication of LTCC substrate with Clark-type electrodes 126
5.3.3 Incorporation of solid-state electrolyte and oxygen permeable membrane 126
5.3.4 Fabrication of PDMS channel and its bonding to LTCC substrate 127
5.4 Results and discussion: 129
5.4.1 Theory of operation 129
5.4.2 Cyclic voltammetry of the sensor 130
5.4.3 Oxygen sensing and flow rate effects 131
5.4.4 Medium effects on measured oxygen concentrations 132
5.4.5 Calibration curve 134
5.4.6 Response time 139
5.4.7 Lifetime and stability of the sensor 141
5.5 Conclusion 144
Chapter 6 Summary and future work 146
6.1 Summary 146
6.1.1 Development of a biocompatible low temperature co-fired ceramic substrate using a commercially available soda-lime-silicate glass and Al_2O_3 ceramic filler 146
6.1.2 Sintering behavior and biocompatibility of a low temperature co-fired ceramic developed using an experimentally fabricated calcium alumina borosilicate glass and Al_2O_3 ceramic filler 147
6.1.4 A microfluidic LTCC based Clark-type oxygen sensor for real-time oxygen sensing 148
7.2 Future work 149
Reference 151
Vita 166

List of Tables

Table 1-1: Comparison of key attributes of common microfluidic substrate architectures. (* Component costs of Glass and Silicon assume high volume manufacture, at low volumes capital/setup/yield considerations would increase costs by several orders of magnitude) 3

Table 2-1: Properties of LTCC materials. Modified from the reference[35, 45] 10

Table 3-1: Live cell percent and cell concentration of the cultured cells using fresh medium (control), leachate medium (LTCC Leachate) and on fibronectin coated LTCC substrate (LTCC). 85

Table 4-1 Surface resistance of the co-fired electrode..... 113

Table 5 - 1: Comparison of the properties of LTCC based microfluidic Clark-type oxygen sensor and other Clark-type oxygen sensor. PP: Polypropylene; FEP: Fluorinated ethylene propylene. 144

List of Figures

Figure 2.1: Flow diagram of LTCC preparation processing from green tapes to sintering12
Figure 2.2: (a) Integrated device with inlet, outlet and optical fiber. (b) Inside view of the device with reactor cells and channels. Reprinted from reference[68, 69]. 15
Figure 2.3: LTCC based module for cell analyzer. Reprinted from reference[72]..... 16
Figure 2.4: Six pathways for material transport during the initial stage of sintering (taken from T. A. Ring[76]). 1: Surface diffusion at particle surface; 2: Lattice diffusion at particle surface; 3: Vapor transport at particle surface; 4: Boundary diffusion at grain boundary; 5: Lattice diffusion at grain boundary; 6: Lattice diffusion caused by plastic flow. Pathways 1, 2 and 3 induce coarsening, where pathway 4, 5 and 6 lead to sintering. 20
Figure 2.5: Schematic of the microstructure evolution of the three stages in the liquid-phase sintering (taken from R. M. German[84]). 25
Figure 2.6: The three mechanism for densification during solution-precipitation in liquid phase sintering: (a) contact flattening, (b) Ostwald ripening, (3) solid-state bonding. (taken from R. M. German[84]). 28
Figure 2.7: Microstructure evolution of the three stage in nonreactive liquid phase sintering model proposed by Ewsuk et al. Reprinted from the reference [74].31
Figure 2.8: Densification process of ceramic-filled glass composite by viscous flow. Reprinted from the reference[73]. 34
Figure 2.9: Simplified example setup for intensity-based optical oxygen sensing. Reprinted from the reference[104] 37
Figure 2.10: Illustration of “pulse-and-gate” time-domain luminescence lifetime detection. Reprinted from the reference[104]. 38
Figure 2.11: (a) Illustration of the microfluidic device with integrated optical oxygen sensor, (b) Image of the fabricated device, (c) Microstructure of the microfluidic multiplexor and oxygen concentration gradient generator. Reprinted from the reference[109] 40
Figure 2.12: Concentration profile of species for several times after the start of Cottrell experiment, $DO = 2.1 \times 10 - 5\ cm2/s$..... 48
Figure 2.13: Simulated current response of species O_2 using Cottrell equation, $DO = 2.1 \times 10 - 5\ cm2/s, A = 0.2\ mm2$..... 48
Figure 2.14: Configuration of an electrochemical system under the boundary condition at t=0 and t=∞). 50
Figure 2.15: Concentration response of the simulated diffusion limited electrochemical systems. The boundary conditions are that the concentration at the electrode is zero and the concentration in the sample solution is constant. Diffusion coefficient of Nafion 117 (0.4×10^{-6} cm^2/s) [19] is used, and membrane thickness is 20.54 µm. 52
Figure 2.16: Plot of current response of the electrochemical system under diffusion limited kinetics and specific boundary conditions. Diffusion coefficient of Nafion 117 (0.4×10^{-6} cm^2/s) [19] is used, and membrane thickness is 20.54 µm. It takes 2.5 s for the current to reach 120% normalized steady state current. 53

Figure 2.17: Oxygen electrode structure. Reprinted from reference [123] 56
Figure 2.18: Development of Clark-type electrode. Reprinted from the reference[126]. (a) Working electrode without gas permeable membrane; (b) Working electrode with gas permeable membrane intercalated and fixed between two silicon substrate; (c) Gas permeable membrane formed on a hydrogel containing electrolyte; (d) Electrolyte gel injected in a polyimide pool; (e) Electrolyte gel in an anisotropically etched groove on a silicon substrate; (f) A gas permeable membrane adhered on a microcontainer formed on silicon and glass as substrate and an filled electrolyte solution; (g) A gas permeable membrane adhered on a microcontainer formed on silicon and an filled electrolyte solution. (h), (i) Electrolyte solution filled from the back of the substrate. 57
Figure 2.19: Structure of the miniature Clark-type oxygen sensor. Reprinted from the reference[41]. (a) Glass substrate with cathode and reference anode, (b) expanded view of the Ag/AgCl anode, (c) silicon substrate with the recess for the electrolyte solution, (d) completed oxygen sensor, (e) cross-section of the sensitive area, (f) experimental setup for measuring blood samples. 60
Figure 2.20: The structure of Clark-type oxygen sensor. Reprinted from reference[40]. (a) Glass substrate with three electrode and electrolyte channel made by photoresist, (b) PDMS reservoir with gas permeable membrane. C, R, W refers to counter, reference and working electrode respectively. 61
Figure 2.21: The output current results of the fabricated oxygen sensor with PP, FEP, and PDMS membrane when the sensor changes from the full-oxygen state to the zero-oxygen state. Reprinted from the reference[71] 62

Figure 3.1: Tape casting process. Reprinted from the website[156] 68
Figure 3.2: Flow diagram of tape casting. 70
Figure 3.3: Experimental procedure for biocompatibility testing..... 75
Figure 3.4: DSC and TGA of the green tape with 46 wt% glass at heating rate of 5 ^{O}C/min. 77
Figure 3.5: Densification, open porosity and shrinkage in the x and y directions of the green tape at different sintering temperature..... 77
Figure 3.6: XRD of the LTCC sintered at different temperature..... 78
Figure 3.7: SEM of the LTCC fracture surface 80
Figure 3.8: SEM of the interface between gold electrode and LTCC sintered at 900 ^{O}C. 81
Figure 3.9: Dielectric properties of the LTCC sintered at 900 ^{O}C..... 82
Figure 3.10: Pictures of the cultured cells using fresh medium (control), leachate medium (LTCC leachate) and on fibronectin coated LTCC substrate (LTCC). 83
Figure 3. 11: Relative cell density of LTCC and LTCC leachate compared with control.85

Figure 4.1: TGA and DTA of the green tape at heating rate of 10 ^{O}C/min. 102
Figure 4.2: XRD of the glass, LTCC sintered at 825^{O}C, 850^{O}C for 1 h with 5 ^{O}C/min heating rate, and LTCC sintered at 850^{O}C with 1 ^{O}C/min heating rate and at 900^{O}C with 10 ^{O}C/min heating rate..... 103

Figure 4.3: The densification of the LTCC versus sintering temperature at heating rates of 1^{O}C/min, 3^{O}C/min, 5^{O}C/min and 10^{O}C/min. 105
Figure 4.4: Master sintering curve and averaged residual square vs apparent activation energy. The optimum activation energy is 452.4 kJ/mol. 106
Figure 4. 5: The contour map of the predictions of the sintering time. The dash line is for relative density 95%. 106
Figure 4.6: Densification, open porosity, shrinkage of the LTCC and predicted densification using constructed MSC curve sintered at different sintering temperature for 30 min. 107
Figure 4.7: SEM of the fracture surface of the LTCC sintered at 825^{O}C for 30 min. 109
Figure 4.8: (a): SEM of the polished surface of the LTCC sintered at 825^{O}C for 30 min; (b) and (c): the EDS mapping of the element Al and Ca; (d): the intensity of the Al K_{α} and Ca K_{α} in the EDS across the line from left to right in the SEM image. 110
Figure 4.9: Back-Scattered Electron (BSE) images of LTCC cofired with silver (TC0307, Left) and gold (TC8101, Right) at 825^{O}C for 30 min..... 111
Figure 4.10: Optical images of TC0307 silver (a) and TC8101 gold (b) pattern on LTCC surface after cofired at 825^{O}C for 30 min. 112
Figure 4.11: Dielectric properties of the LTCC sintered at 825^{O}C for 30 min..... 114
Figure 4.12: LIVE/DEAD images of HUVEC cultured for 1 day using: fresh media (Control), media stored in incubator for 5 days (Blank), or leachate media stored with LTCC in incubator for 5 days (LTCC). 115
Figure 4.13: Live cell percent and cell concentration from LIVE/DEAD assay of HUVEC cultured for 1 day using: fresh media (Control), media stored in incubator for 5 days (Blank), or leachate media stored with LTCC in incubator for 5 days(LTCC).(Error bars represent standard error). For ANOVA and Turkey test, *p* is 0.02 between control and blank; *p* is 0.65 between control and LTCC, *p* is 0.14 between blank and LTCC. 116
Figure 4.14: Pictures of the cultured cells on the well plate (control), and on the fibronectin coated LTCC surface (LTCC) for 14 hr and 74 hr. 117
Figure 4.15: Live cell percent and cell concentration of the cultured cells on the well plate (control), and on the fibronectin coated LTCC surface (LTCC) for 14 hr and 74 hr. For ANOVA and Turkey test, *p* is less than 0.001 between control and blank after 14 h cell culture; *p* is less than 0.001 between control and LTCC for 74 h cell culture. 118

Figure 5.1: Image of the HL2000 LTCC with plenty of electrical circuits before and after sintering to demonstrate zero shrinkage in x,y direction. Reprinted from the reference[211]. 124
Figure 5.2: Schematic illustration of the reaction mechanism and conceptual presentation of the microfluidic LTCC based Clark-type oxygen sensor. 125
Figure 5.3 Image of the bonded microfluidic LTCC based Clark-type oxygen sensor.. 129
Figure 5.4: Cyclic voltammetry of the DI water..... 130
Figure 5.5: Chronoamperometry of oxygen saturated DPBS under different flow rate, and chronoamperometry of oxygen depleted DPBS 132

Figure 5.6 Chronoamperometry of the oxygen saturated DI water, DPBS under different flow rate..... 133
Figure 5.7: CA curves (a) of the DI water with different oxygen concentration under static condition, and calibration curve (b) obtained using the results of CA. The Current values in the CA curves of DPBS were shown in the calibration curve for comparison. (Reported oxygen concentrations determined by hand held oxygen meter Milwaukee MW600)..... 135
Figure 5.8: CA curves (a) of the DI water with different oxygen concentration under flow 0.2 ml/min, and calibration curve (b) obtained using the results of CA. The Current values in the CA curves of DPBS were shown in the calibration curve for comparison..... 136
Figure 5.9: CA curves (a) of the DI water with different oxygen concentration under flow 0.5 ml/min, and calibration curve (b) obtained using the results of CA. The Current values in the CA curves of DPBS were shown in the calibration curve for comparison..... 137
Figure 5.10: CA curves (a) of the DI water with different oxygen concentration under flow 1.0 ml/min, and calibration curve (b) obtained using the results of CA. The Current values in the CA curves of DPBS were shown in the calibration curve for comparison..... 138
Figure 5.11: Calibration curves obtained from the results of chronoamperometry of DI water with different dissolved oxygen under flow rate 0.0, .02, 0.5, 1.0 mL/min. 139
Figure 5.12: Response curve of Clark-type oxygen sensor were tested by injection of the zero -oxygen solution, 0.1 M sodium sulfite..... 141
Figure 5.13: Chronoamperometry of the oxygen saturated DI water under static condition and flow rate 1.0 ml/min tested using developed oxygen sensor before and after the sensor stored in DI water for eight days..... 143

Chapter 1 Introduction

1.1 Motivation

Microfluidic systems offer many advantages for biomedical diagnostics. Miniaturized features on microfluidic chips require less volume of solvents, reagents and cells. This is especially important for valuable samples and high-throughput screening. Microfluidic systems also offer the advantages of short reaction time, portability, low cost and integration with other miniaturized systems. This unique capability makes microfluidic technology a potential candidate for portable point-of-care medical diagnostic systems in global public health[1, 2]. The applications of microfluidic systems include separations coupled to mass spectroscopy[3], high-throughput screening in drug development[4], examination and manipulation of a single cell[5] or single molecule[6], bioanalysis[7], cell biology[8], chemical synthesis, disease diagnostics [9-12], and drug testing [13, 14]. Microfluidic systems have also been used to separate deoxyribonucleic acid (DNA) for genetic diagnostics [15].

Glass, silicon, steel have emerged as materials for the fabrication of microfluidic systems that require chemical, thermal and mechanical stability[2]. However, integration of electronic circuitry into those systems are complex and expensive[16]. Polymers, such as plastic and poly(dimethylsiloxane) (PDMS) based microfluidic systems are also fabricated with good mechanical flexibility and transparency. However, polymers can be dissolved in solvent, also not stable in high temperature and pressure[2]. The good

mechanical flexibility of polymers also makes it difficult in precise placement of the devices in tissues without flexing or breaking in medical diagnostics and bedside monitoring.

Low temperature co-fired ceramic (LTCC) technology makes it very convenient to design and manufacture three-dimensional microfluidic ceramic systems with integration of complex functions. Low temperature co-fired ceramics (LTCC) consist of a ceramic substrate and any number of conductive, resistive and dielectric materials, which are assembled un-fired "green" in a layered process and consolidated into a functional device in a co-firing process, at a sintering temperature lower than $1000^{O}C$. LTCC technology has already been well established with low cost, high performance. 3D features including channels, via, cavities and internal electrical components can be created easily in LTCC systems. Mechanical, optical, electrical and fluidic functions have been realized in single LTCC module. The manufacture of the LTCC multilayer modules is a simple and fast process compared to traditional microfluidic silicone/glass micromachining. Miniaturized microfluidic LTCC systems have been used in flow sensors[17, 18], optical detection sensor[19, 20], biosensors[21-23], chemical detection sensors[24-31], and DNA detection[32-34]. The combination of microfluidics and electronics into one single monolithic LTCC systems will enable a wide range of biomedical diagnostic and bedside monitoring. The key aspects of various microfluidic technologies are compared to LTCC in Table 1.1.

Table 1-1: Comparison of key attributes of common microfluidic substrate architectures. (* Component costs of Glass and Silicon assume high volume manufacture, at low volumes capital/setup/yield considerations would increase costs by several orders of magnitude)

Substrate	Physical Patterning speed	Electrical/Functional Integration	Chemical/Physical Durability	Costs: Start-up/Component
MLC	Fast: Direct write, molding, punching	Easy: single step screen printing	High	Moderate/Moderate (~\$1 cm^{-2})
PDMS soft lithography	Fast: molding, punching	Moderate: physical incorporation	Unacceptable	Low/Low (<\$0.10 cm^{-2})
Silicon	Moderate: Chemical Etch, milling	Moderate: Multistep (deposit, pattern, etch)	Chemical: High Physical : Poor	High/High (>\$10 cm^{-2})*
Glass	Moderate: Chemical Etch, EXIMER Laser	Moderate: Multistep (deposit, pattern, etch)	Chemical: High Physical: Moderate	Moderate/Moderate (\$10 cm^{-2})*[35]

Commercial LTCC systems are available from Ferro, DuPont, Hereaus, and others. However, exact compositions of those systems are proprietary[36]. These, commercial LTCC systems have not been designed or approved for biomedical applications. Prior experimental studies by our group have shown that some elements in the commercial LTCCs may be leached out[37]. Some of the leached LTCC elements, such as heavy metals and Ni^{2+}, may be toxic to cells in the cell culture. Dissolved Ni^{2+} can substitute for other divalent metals, such as Ca^{2+}, Mg^{2+} and Zn^{2+}, in enzymes and proteins and change the molecular structure. This may result in cell transformation and chromosome damage[38]. In order to increase the utility and acceptance of LTCC for biomedical applications, LTCC materials specifically designed for their biocompatibility should be developed. In the current work this will be achieved by starting with materials of known composition and biocompatibility.

The critical feature of LTCC technology being exploited for the current work is the possibility of integrating the microfluidic components, such as microchannels and reservoirs, with electronic and electrochemical functionality, including actuators and sensors. In order to demonstrate and advance these capabilities of LTCC technology the materials and methods required to integrate a lab-on-chip oxygen sensor into LTCC technology will be developed. Oxygen consumption is a very important index of the cell activity. It has been used to analyze the physiological response of the cells on exposure of chemical and physical stimulations[39, 40]. The measurement of oxygen concentration can be applied in clinical diagnostics, fermentation monitoring, pharmacological drug screening, tumor chemosensitivity and environmental toxicant monitoring[39-44].

1.2 Organization of the thesis

The key goals of the present thesis are to understand the structure processing property relationships required to synthesize biocompatible LTCC for biomedical applications and to develop the materials and method required to integrate an oxygen sensor into LTCC for future microfluidic biomedical applications.

The specific objectives of this thesis are:

1. Design biocompatible LTCC materials: Commercial LTCC materials are not designed for biomedical applications. Biocompatible LTCC materials are needed which have been developed specifically for applications in the biomedical field. Alumina was used as the ceramic in LTCC, and low temperature glass frit was used as the flux to lower the sintering temperature and bond the alumina grains together. Basic material characterization methods were used to analyze the properties of the

materials. The densification of the green tape, phase evolution, structure characteristic and dielectric properties of the sintered LTCC were characterized. The biocompatibility of the LTCC was also evaluated through leaching the ceramic in cell culture media and cell growth on the surface of the ceramic

2. Device applications: The goal of multilayer ceramic design is to apply the LTCC materials in the microfluidic systems to measure oxygen consumption of cells, which is an important parameter of cell activity. LTCC microfluidic systems were integrated with Clark-type oxygen electrode. The properties of fabricated LTCC based oxygen sensor were analyzed using electrochemical technique.

Specific contents of each chapter are listed below:

Chapter 1 introduce the motivation and organization of this thesis

Chapter 2 provides the literature review of LTCC materials and technique and its application in microfluidic systems. The theoretical mechanism involving in sintering of ceramic is also reviewed. Finally, mechanisms of oxygen sensors involving luminescent sensing and electrochemical sensing techniques and the applications are discussed.

Chapter 3 and 4 present the experimental works on the design and fabrication of biocompatible LTCC materials using ceramic filler and a low temperature glass. In chapter 3, a LTCC material is produced using Al_2O_3 ceramic filler and a commercial available soda-lime-silicate glass. In chapter 4, Al_2O_3 ceramic filler and an experimentally fabricated calcium alumina borosilicate glass are used to fabricate the LTCC material. Phase evolution, sintering properties, microstructure, dielectric properties and *in vitro* biocompatibility of the both developed LTCC material are analyzed.

Chapter 5 describes the design, fabrication and characterization of LTCC based Clark-type oxygen sensors. Solid state proton conductive electrolyte is used, and microfluidic function is realized in this device.

Chapter 6 summarizes the research work of the thesis and future opportunities this research can be related with.

Chapter 2 Background

Theoretical background related with the research work in this thesis is reviewed in this chapter. First, LTCC materials, processing and application in microfluidic systems are introduced. Second, the theories of ceramic sintering, especially sintering mechanisms with relevance to LTCC materials, are presented. Finally, the mechanism and applications of oxygen sensing, including luminescent optical sensing and electrochemical amperometric sensing techniques, are discussed.

2.1 Low temperature co-fired ceramics (LTCC)

Low temperature co-fired ceramics (LTCC) are widely utilized in the fabrication of compact, three dimensional, and highly integrated microelectronic components. Typical applications include military and mobile electronics applications requiring custom, hermetic, and/or high reliability packaging[17, 19, 45, 46]. These characteristics also make LTCC attractive for use in microfluidic and biomedical application[19, 20, 26].

2.1.1 LTCC materials

Low temperature co-fired ceramics (LTCC) are a glass-ceramic composites with densification temperature lower than 1000^{O}C. The LTCC was originally developed from high temperature co-fired ceramics (HTCC) in order to achieve low loss, high speed and high density package[47]. HTCC technology was originally developed in the late 50s and based on the technologies used in the substrate fabrication for current process, including green sheet fabrication technology, via forming technology, and multilayer laminate technology using the doctor blade[48, 49]. The HTCC was usually co-fired at the high

temperature of 1600 ^{O}C. Alumina insulating materials and conductor materials of Mo, W and Mo-Mn were used. However, materials with low electrical resistance, such as Cu, Au and Ag, were preferred in order to improve high speed transmission of signal[50]. LTCC materials were developed to be co-fired at low temperature, which is compatible with the sintering temperature of metals with low electrical resistance. The typical conductive metals used in the LTCC have high electric conductivity, including Ag, Cu, Au and their alloys (for example Ag-Pd, Ag-Pt, Au-Pt etc.)[47]. In addition, LTCC can be co-fired with support structure, resistive and dielectric materials in a furnace at the same time with sintering temperature lower than 1000^{O}C.

LTCC materials are available commercially in tape format (50-350 μm) and produced by tape casting of a ceramic slurry onto a polymer substrate such as Teflon®, Mylar®, or cellophane[51]. LTCC green (unfired) tapes are composed of ceramic particles, organic binder and fluxing materials. Organic binder is used to hold ceramic particles together, and make the green tape flexible. The fluxing materials are used to lower the sintering temperature. The most common ceramic filler is alumina, and nearly all commercial LTCC green tapes contains more than 50 vol% glass matrix, most between 63 to 85 vol%[46]. The glass matrix in LTCC not only binds the ceramic together but also lowers the sintering temperature of the ceramic filler. Other ceramic fillers, were added to system to obtain LTCC with specific properties, such as high thermal conductive beryllia (BeO)[52], ferroelectric barium strontium titanate ($Ba_{0.7}Sr_{0.3}TiO_3$)[53], and dielectric magnesium calcium titanate ($MgCaTiO_3$)[54]. Standard ceramic processing is used to manufacture LTCC green tape, including ceramic powder preparation, colloidal processing, and tape casting technique[55].

There are three possible approaches to formulate LTCC materials. The first way is based on a mixture of low melting temperature glass and high temperature ceramic filler. There is little reaction between the glass and ceramic powder, and the glass mainly acts as a binding agent between the ceramic grains. The second approach is through recrystallization. For example, the commercially available green tape Ferro A-6 is made of a crystallizable glass phase with low softening point. The glass recrystallizes to form the low loss dielectric ceramic wollastonite[56]. The third method is also a mixture of glass and ceramic powder, but the glass and ceramic will react with each other at the sintering temperature to form dense ceramic. An example of this kind of LTCC formulation is the Hereaus CT2000 system [57]. This system consists of crystalline Al_2O_3, and a reactive B_2O_3, K_2O, SiO_2, CaO, SrO, and BaO glass phase. TiO_2 has been added to acts as nucleating agent and dielectric anorthite-type crystalline is formed at the sintering temperature[57]. The glass phase helps densification of the ceramic.

The recent trend in the LTCC development has been through the third type of reactive glass-ceramic systems. Typical glass systems used in LTCC include lime silicate[58], borosilicate, lead borosilicate, and alkali earth borosilicate[56, 57, 59]. Many ceramic materials, such as ferroelectric perovskite, ferromagnetic spinels[46], have been used depending on the required properties. Dielectric microwave ceramic has also been added as ceramic filler in LTCC for high frequency applications in wireless technology[59, 60]. The ratio of ceramic and glass can be changed to obtain favorable sintering temperature and properties. Less glass can be added to retain the properties of the ceramic filler, and more glass can be added to lower the sintering temperature[61]. Table 2-1 lists the properties of commercial LTCC materials.

Table 2-1: Properties of LTCC materials. Modified from the reference[35, 45]

Properties	DuPont DP 951	DuPont DP 943	Ferro A6M	Heraeus CT 2000	Heraeus HL2000
Dielectric constant	7.85	7.5	5.9	9.1	7.3
Dissipation factor	0.0045	0.001	0.002	0.002	0.0026
Breakdown voltage (V/25 µm)	> 1000	> 1000	> 1000	> 1000	> 800
Resistance (Ωcm)	$> 10^{12}$	$> 10^{12}$	$> 10^{12}$	$> 10^{13}$	$> 10^{13}$
Thickness – green (µm)	50, 112, 162, 250	125	125, 250	25, 50, 98, 127, 250	131
Thickness – fired (µm)	42, 95, 137, 212	112	92, 185	20, 40, 77, 102, 200	87-94
Shrinkage x,y (%)	12.7±0.3	9.5±0.3	14.8±0.2	10.6±0.3	0.16±0.24
Shrinkage z (%)	15.0±0.5	10.3±0.3	27±0.5	16.0±1.5	32
CTE (ppm/K)	5.8	4.5	7	5.6	6.1
Thermal cond. (W/m.K)	3	4.4	2	3	3
Density (g/cm^3)	3.1	3.2	2.45	2.45	2.45
Youngs Modulus (GPa)	152	-	92	-	-
Flexural Strength (MPa)	320	230	>170	310	>200
Phase Structure	α- Al_2O_3 $Ca(Si,Al)_4O_8$	α- Al_2O_3 $(Ca)Al_2B_2O_7$ $Ca(Si,Al)_2O_8$	$CaSiO_3$ $MgSiO_3$ SiO_2 CaB_2O_4	α- Al_2O_3 $CaAl_2Si_2O_8$ $CaSiO_3$	α- Al_2O_3 $CaAl_2Si_2O_8$ $CaSiO_3$

2.1.2 LTCC processing

The fabrication of LTCC based devices starts from LTCC green tapes. LTCC green tapes are first cut into specific size in the standard LTCC process. Via holes and channels are patterned using mechanical punching or laser cutter. Electrical circuitry and interconnects, utilizing conductor, resistor and dielectric pastes, are produced by screen printing. Conducting holes (vias) providing electrical connectivity between tape layers are also filled with conducting pastes at this stage. The individual layers are then aligned, stacked together and laminated using uniaxial press under specified pressure and temperature. The laminated stack is co-fired to certain temperature to burn out organics and sintered at temperatures lower than 1000^{O}C. The shrinkage (typically 10-15%) of the LTCC during the co-sintering should be carefully controlled and compensated in the design process.

The sequence in the standard LTCC process is usually fixed, and more complex procedures are required to make mechanical microstructures in the LTCC. The sequence of the process is dependent on the structure of the LTCC and always contains some loops among mechanical processing, thick film printing and isostatic or uniaxial lamination. More than one step lamination is needed in most cases. Good workability is achieved in the “green” state, but mechanical processing in sintered LTCC is not feasible. Figure 2.1 shows the LTCC preparation process.

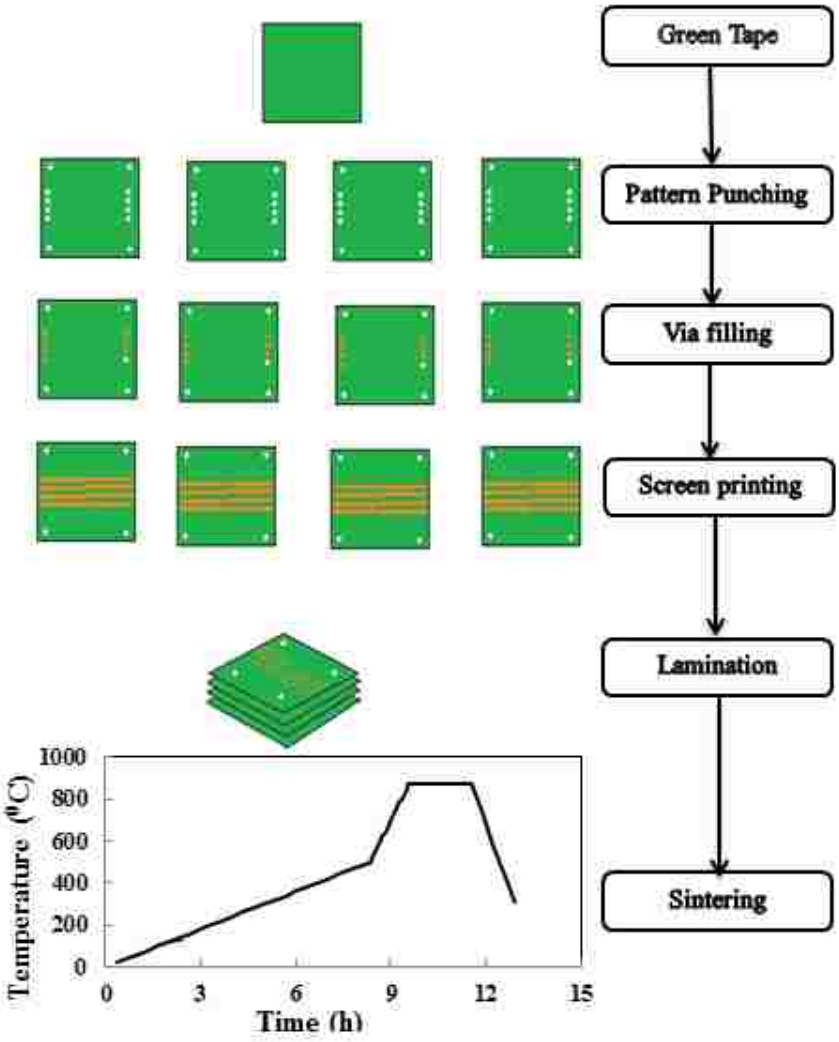

Figure 2.1: Flow diagram of LTCC preparation processing from green tapes to sintering

2.1.3. Applications of LTCC based microfluidic system

The LTCC technology is commonly used for applications that require high packaging density and reliability, such as automotive and RF[62]. The LTCC technology has been used in the application of military, avionics and automotive areas, as well as in multi-chip modules (MCMs) for communications and computer applications in the last 30 years[46]. In most applications, the LTCC substrate works as a passive substrate for

electronic functions. However, the workability in the "green" non-sintered stage and flexibility of the layered manufacturing process allows integration of non-electronic functions very effectively. One of the important features of LTCC technique is the capability of fabricating three dimensional structures by stacking layers of green tapes. Features needed for a specific application can be designed on each layer of the green tape, including vias, cavities, channels, and electrical elements such as capacitors, resistors and conductors. Finally each layer of the green tape is stacked in a proper order. The design and manufacture of the LTCC substrate can be customize according to the applications.

Silicon integrated circuit technology has been extensively used to combine microelectronics and micro-electromechanical systems (MEMS). The key advantage is the ability to densely fabricate and integrate micro and nano scale electrical and electromechanical components. However it requires costly purpose build facilities and equipment, and costs do not scale well for low volume production and/or large area macroscale devices[46]. The LTCC technology is widely used in the electronics for both specialty and high-volume fabrication of densely integrated multilayer printed circuit boards. The advantages of the LTCC processing methodology enables its' application for the development and production of miniaturized total analysis systems (íTAS). These advantages includes: 1) inexpensive and direct fabrication of three-dimensional features, 2) integration with passive electronic component, and 3) multilayer assembly[16, 17, 46, 63-65]. In certain applications (such as moderate volume or large area device), LTCC processing techniques can be a viable alternative to silicon micromachining. Additional advantages compared to traditional microfabrication substrates and methods (such as glass, silicon or polymers) including no need of special fabrication conditions (as clean room), no need to

hermetically seal elements, “moldless” forming, rapid prototyping, and highly scalable manufacturing[16].

One of the important advantages of LTCC technology is the easy integration of the three dimensional structures required for microfluidic components, such as microchannels, valves and chambers. LTCC has been previously demonstrated and commercialized in microfluidic systems for a variety of applications.

Characteristics including high thermal isolation, chemical inertness, and integration of dense microfluidic networks has led to the successful development of LTCC based microfluidic systems in microreactor applications, including polymerase chain reaction (PCR) systems[32-34, 66, 67]. PCR is a powerful technique that can be used to copy DNA fragments through a sequential thermal cycling process, which can be further used to identify genetic diseases, cancer type, and human samples[32]. Microreactors for PCR require integration of multiple functionalities including mixing, heatering and temperature sensing. LTCC based PCR systems have been successfully developed and used for DNA measurement and amplification[32-34].

The 3D capability of LTCC processing also allows integration of multiple functions for microreactors. Microreactor systems developed by Smetana *et al.*, not only contain a spherical reactor cell and channel for accumulation and mixing of reagent but also sensor arrays for monitoring hydrogen ions, oxygen, temperature and iodide as shown in Figure 2.2[68, 69]. LTCC-based devices have also been used for chemical detection and analysis[20, 24-31] including heavy metals[26], pesticides[25], organic compounds[31], and toxic ions or

compounds in water[27-30]. A chromatographic apparatus for gas separations have also been developed in the LTCC substrate[70].

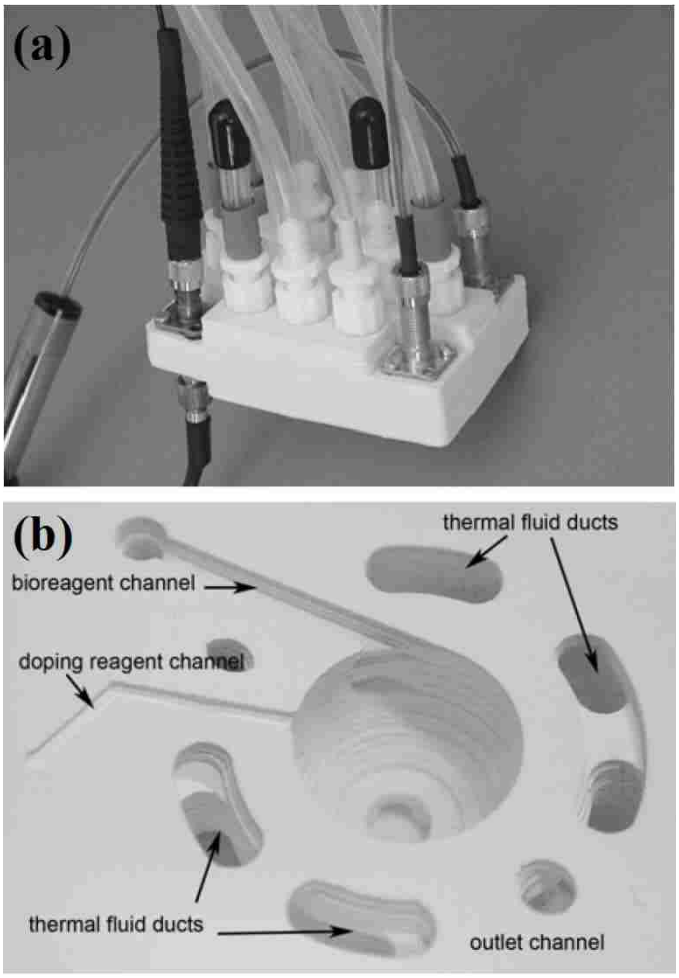

Figure 2.2: (a) Integrated device with inlet, outlet and optical fiber. (b) Inside view of the device with reactor cells and channels. Reprinted from reference[68, 69].

Microfluidic devices are also widely used in biosensing. Biosensors are used for detection and quantification of a wide range of various biological markers of health and disease. The sensitive and specific detection of biomarkers often relies on biological recognition through the integration of antibodies, enzymes, receptor proteins, nucleic acid, or cells used in the sensing elements. The easy integration of microfluidic functions with

electrical and mechanical components in the LTCC modules facilitates the development of suitable platform for biosensing systems. LTCC based biosensors have been developed to continuously monitor the glucose[21] and to detect urea in biological fluids[22]. Antibodies and enzymes have also been immobilized on screen-printed LTCC and HTCC electrodes for electrochemical detection[23].

Microfluidic cell culture can provide important information for growth dynamics and the possibility of investigating physiological function and properties under application of mechanical and chemical stimuli. LTCC based microelectrode arrays have been used to monitor the change of media, growth of different species and toxicity level during cell culture[71]. An LTCC-based micro cell analyzer integrating a fluorescence-activated detection flow cytometer has also been developed for detection and counting of bioparticles as shown in Figure 2.3[72].

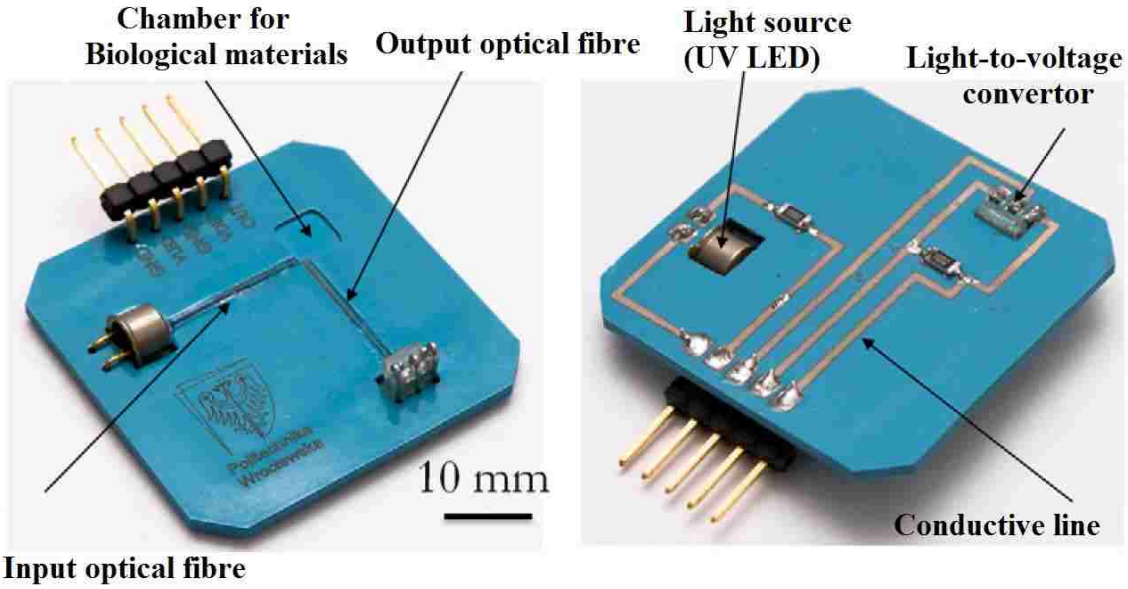

Figure 2.3: LTCC based module for cell analyzer. Reprinted from reference[72].

2.2 Ceramic sintering theory

This section describes current theory and mechanisms of ceramic sintering, and it includes four parts: solid state sintering, liquid state sintering, viscous sintering and non-reactive liquid phase sintering. The sintering of glass-ceramic composite with a large volume of glass phase, such as LTCC, is controlled by the viscous flow of glass phase at the high temperature. Theories of both viscous sintering and non-reactive liquid phase sintering have been used to study the sintering mechanism of LTCC materials[73-75].

2.2.1 Solid state sintering

Driving force for sintering

The driving force for solid state sintering, DF_{STS}, is the reduction in the total free energy of the system[76]:

$$\Delta G_T = \Delta G_V + \Delta G_{gb} + \Delta G_s \tag{2.1}$$

where ΔG_V, G_{gb}, and ΔG_s represents the change in free energy related with the volume, grain boundary, and surfaces of the grains respectively. If only the solid-vapor interface is removed during the sintering, the change in the surface free energy is described as

$$\Delta G_T = \Delta G_s = \gamma_{sv}\times(\text{Final surface area-Initial surface area}) \tag{2.2}$$

where γ_{sv} is the solid-vapor interfacial energy. For spherical particles, the initial surface area per unit volume is given by $3/a$, where a is the mean radius the ceramic particles. The driving force, defined as the force per unit area, is given by

$$DF_{STS} = 3\gamma_{sv}\left(\frac{1}{a'} - \frac{1}{a}\right) \tag{2.3}$$

where a' is the mean radius of curvature after the sintering. In addition, local differences in free energy also lead to diffusion during sintering. Diffusion happens from a region with positive surface curvature to a region with a less positive, zero, or negative surface curvature. For the fully dense body, $3\gamma_{sv}/a$ can be used to estimate the motivation for sintering [77].

In hot pressing and hot isostatic pressing, an external compressive pressure is applied. This pressure provides extra driving force and enables sintering at lower temperature or fast sintering at constant temperature. The effect of the applied pressure on the driving force is given by

$$DF_{STS} \propto P_{applied} - 3\gamma_{sv}\frac{1}{a} \tag{2.4}$$

Stages of sintering

The ceramic green body is heated up to the temperature approaching the melting point of ceramic during the sintering. Grains and pores change in size and shape during the sintering. Elimination of pores results in densification or sintering of the ceramic. However pore shape change without an increase of the density only leads to coarsening. In case of densification, the average interparticle separation distance decreases. If the interparticle separation distance remains the same, coarsening happens. In classical sintering theory, sintering can be simplified and considered as three distinct stages: an initial stage, an intermediate stage and a final stage.

The driving force for the initial stage is the curvature difference between the particle surface and that of the neck. A more accurate assessment of the sintering driving force is described by the Gibbs free energy[78]. The change of the Gibbs free energy of the ceramic body at constant temperature without applied pressure, chemical reaction or phase evolution is given by

$$\Delta G = \Delta\left(\gamma_{gb} A_{gb}\right) + \Delta(\gamma_{sv} A_{sv}) \tag{2.5}$$

where γ_{gb}, γ_{sv} are the interfacial energies of the grain boundary (subscript gb) and solid-vapor surface (subscript sv). And A_{gb} and A_{sv} refers to the area. The delta means the final state minus the initial states. The initial and final curvature of neck and particles surface gives the sintering driving force as described in the equation. The characteristic change occurring during the initial stage is neck formation. The initial stage also includes particle surface smoothing and rounding of pores. Grain boundaries form and only open pores exist. The six distinguishable diffusion paths of material transport, as shown in Figure 2.4, are the most probable mechanisms for neck growth. But not all these mechanism decrease the interparticle separation leading to densification. Surface diffusion, lattice diffusion and vapor transport at particle surface cause coarsening. Boundary diffusion, lattice diffusion at grain boundary, and plastic flow can lead to densification. The initial stage lasts until the neck reaches ~0.4-0.5 of the particle radius and there is an increase of the density to 65% of the theoretical density[77].

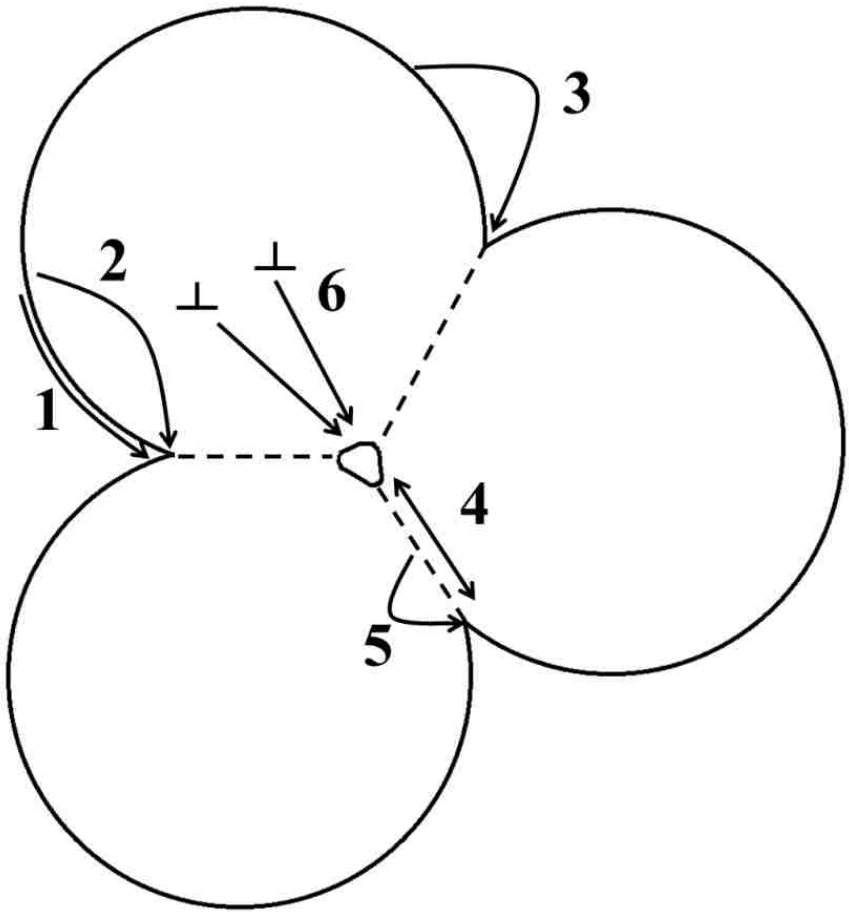

Figure 2.4: Six pathways for material transport during the initial stage of sintering (taken from T. A. Ring[76]). 1: Surface diffusion at particle surface; 2: Lattice diffusion at particle surface; 3: Vapor transport at particle surface; 4: Boundary diffusion at grain boundary; 5: Lattice diffusion at grain boundary; 6: Lattice diffusion caused by plastic flow. Pathways 1, 2 and 3 induce coarsening, where pathway 4, 5 and 6 lead to sintering.

Intermediate stage starts after the pores reach their equilibrium shapes. In this stage, pores form continuous cylindrical channels at all three grain intersections. The cylindrical pore simply shrinks to reduce the cross section resulting in densification in this stage. When the length to radius ratio exceeds a critical value, the cylindrical pore breaks up into isolated pores and the intermediate stage ends; this triggers the beginning of the final stage. Major densification occurs in this stage with density reaching ~90% of the theoretical value. Densification mechanism includes lattice diffusion and grain

boundary diffusion at grain boundary. Plastic flow is not considered to lead to a significant effect in single phase ceramic systems in the absence of a liquid phase.

The final sintering stage consists of the removal of these closed pores. The removal of the pores will decrease the energy of the system. As the curvature of the pore increases, the driving force increases. The curvature of the pore is dependent on the dihedral angle and number of grains the pore contacts. The dihedral angle, ψ, has a relationship between γ_{gb} and γ_{sv} :

$$\frac{\gamma_{gb}}{2\gamma_{sv}} = cos\frac{\psi}{2} \tag{2.6}$$

The dihedral angle is only dependent on the interfacial energy[79]. As the dihedral angle increase, the curvature of the pore increase. As the grain growth occurs, the number of grains around pores decreases so the curvature of the pores increase and the pores will shrink leading to densification. However, the diffusion path increases resulting in slow shrinkage process. Lattice diffusion and grain boundary diffusion at the grain boundary play an important role in the pore reorganization. The isolated pores will migrate into the region with lowest energy. The intersection of four grains has the lowest energy in three dimensions. The pores at the intersection of four grains can disappear in a stable way during the sintering. However, grain growth at expense of others, discontinuous grain growth, traps the holes inside a grain. Once a pore is trapped, it is difficult to eliminate. Then the final density is less than the theoretical value. The final stage sintering is the most important for ceramic applications as it determines ultimate properties of the material.

2.2.2 Liquid state sintering

Liquid phase sintering has been frequently used to lower the sintering temperature of ceramics. The presence of a liquid phase in the system can enhance densification. First, if the liquid can wet the ceramic surface and spreads around the ceramic particle, there will be a liquid bridge between ceramic particles. The friction between the ceramic particles can be greatly reduced, and rearrangement of the ceramic particle can be improved. Second, the liquid provides a faster pathway for matter transport. The liquid bridge between the ceramic particles is many time larger than grain boundary in solid state and the diffusion in the liquid phase is much faster than in solids.

The basic requirement for liquid phase sintering is a good wetting of the solid by the liquid. The degree of wetting is controlled by the contact angle θ, which is related with the interfacial energy, γ, for the solid-vapor (sv), solid-liquid (sl), and liquid-vapor (lv) interfaces[80]:

$$\gamma_{sv} = \gamma_{sl} + \gamma_{lv} cos\theta \tag{2.7}$$

The spreading of liquid is governed by[80]:

$$S_{l/s} = \gamma_{sv} - \gamma_{sl} - \gamma_{lv} \tag{2.8}$$

where $S_{l/s}$ is the spreading coefficient. When $S_{l/s}$ is positive, spreading occurs.

Densification during liquid phase sintering is dependent both on the contact angle and dihedral angle. The dihedral angle, ψ, is defined by [81]:

$$cos\frac{\psi}{2} = \frac{\gamma_{ss}}{2\gamma_{sl}} \tag{2.9}$$

It has also been used to estimate the liquid penetration of the grain boundary and the shape of the liquid and the grains. For $\frac{\gamma_{ss}}{\gamma_{sl}} \geq 2$, the dihedral angle equals to 0^O, and the liquid will penetrate through the grain boundary, all grains will be separated by the liquid phase. For $\sqrt{3} < \frac{\gamma_{ss}}{\gamma_{sl}} < 2$, the dihedral angle takes the value between 0^O and 60^O, the liquid will penetrate through all three-grain boundary junctions but partially penetrate through the two grain interfaces. For $1 < \frac{\gamma_{ss}}{\gamma_{sl}} \leq \sqrt{3}$, the dihedral angle is from 60^O to 120^O, and isolated liquid phase forms and partially penetrates through the three-grain junctions. If $\frac{\gamma_{ss}}{\gamma_{sl}} < 1$, and then the dihedral angle is larger than 120^O, and isolated liquid phase only forms at the four-grain junctions.

The chemical reactions between glass and ceramic particles are relatively weak in most liquid-phase sintering systems, so the interfacial energies are the dominant factors that control sintering. The driving force for liquid phase sintering is the reduction of the liquid-vapor interfacial area. For liquid bridge between two grains, the pressure difference is[76]:

$$\Delta p = -\frac{2\gamma_{lv}cos\theta}{d} \tag{2.10}$$

where d is the distance between the grains. The pressure within the liquid is less than the external pressure. This pressure difference exerts a compressive force on the ceramic body. This compressive force is responsible for the particle rearrangement. For a spherical pore with radius, r, the pressure difference becomes:

$$\Delta p = -\frac{2\gamma_{lv}}{r} \tag{2.11}$$

The pressure difference also generates a compressive capillary force on the particles, and provides substantial driving force for sintering.

Stages of sintering

There are three stages in the liquid-phase sintering: liquid redistribution and particle rearrangement, solution-precipitation and final densification as shown in Figure 2.5.

The glass phase melts as the sintering temperature increases, and capillary pressure causes the liquid flow, leading to the redistribution of the liquid and particle redistribution. The ceramic particles initially slide over one another, and then a glass bridge is built up between grains. Substantial particle rearrangement will take place to achieve a maximum packing and a minimum pore surface. The rearrangement is difficult when the liquid volume is small. Kingery[82, 83] describes the rearrangement happens initially by viscous flow and is followed by plastic flow with an effective yield point, and derives the relationship of the shrinkage of the composite with time:

$$\frac{\Delta L}{L_0} = \frac{\Delta V}{3V_0} \sim t^{1+y} \tag{2.12}$$

where t is time, ΔL and ΔV are the change in length and volume, L_0 and V_0 are the original length and volume, y is positive constant with value less than one. Full densification can be achieved through rearrangement if sufficient liquid is present. Complete densification requires additional sintering process for systems with less than 35 vol% glass phase[82].

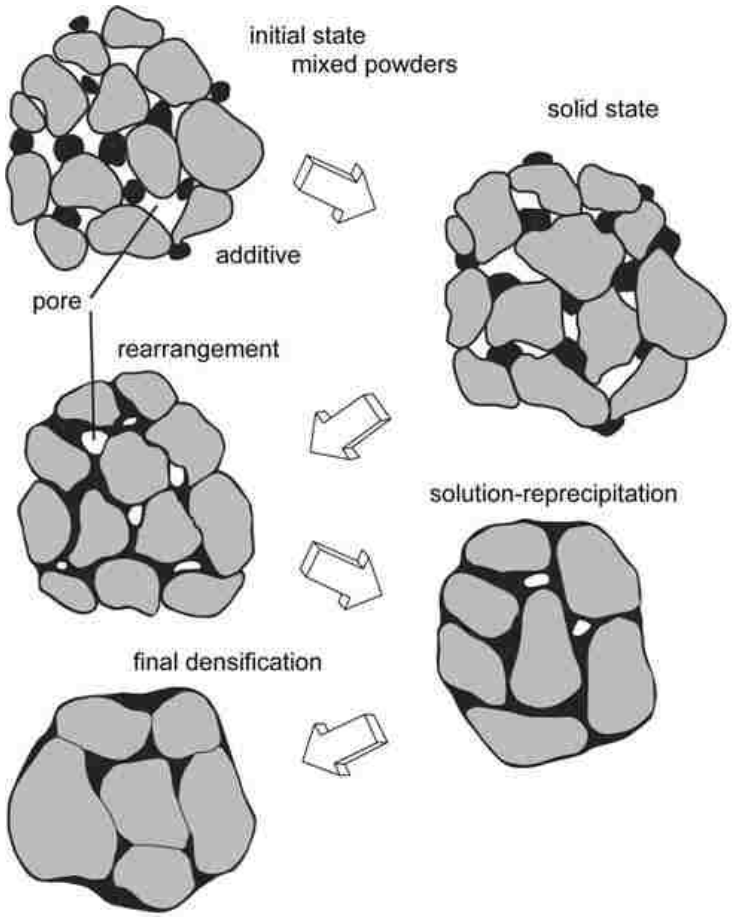

Figure 2.5: Schematic of the microstructure evolution of the three stages in the liquid-phase sintering (taken from R. M. German[84]).

Once rearrangement has been significantly slowed, the solution-precipitation process becomes dominant mechanism if the solid is soluble in the liquid. If there is insufficient liquid, further densification is dependent on the solid diffusion through the liquid. If the solid is not soluble in the liquid, then diffusion happens through solid-state densification. For solution precipitation, the solid first dissolves into the liquid, preferentially from high energy region, and the dissolved solid diffuses through the liquid phase. Finally, the dissolved solid precipitates on the concave region, or large grains. Pores remains in the composite after the first stage especially for systems with low volume of glass. Solution-precipitation is the most important step to reach full

densification. There are three mechanisms for densification in this stage as shown in Figure 2.6. The first one is contact flattening described by Kingery[82]. The compressive capillary force exerted by a wetting liquid pull the grains together. The chemical potential or solubility at the contact point is significantly higher than that at other solid surfaces, and this provides a driving force for matter transport away from the contact points, leading to reduced center-center distance and densification. The second mechanism for densification is Ostwald ripening[77], which involves dissolution of small grains and precipitation of large grain. Ostwald ripening does not lead to densification, however, grain shape accommodation occurs via Ostwald ripening, which improves the grain packing and reduces overall interfacial energy. The third mechanism involves growth of the intergrain contact through diffusion along the liquid wetted grain boundary[84]. The increased intergrain contact changes the grain morphology and increase the density.

In the intermediate stage, if mass transport is controlled by interfacial events, it is reaction controlled solution-precipitation. The sintering shrinkage given by Kingery[82] is described as:

$$\left(\frac{\Delta L}{L}\right)^2 = \frac{g_1 k \Omega \gamma_{lv} t C}{RTG^2} \tag{2.13}$$

where g_1 is geometric constant, k is the reaction rate constant, t is the time, C is the solid concentration in the liquid, γ_{lv} is the liquid–vapor surface energy, Ω is the atomic volume of the solid, R is the gas constant, T is the absolute temperature, G is the solid grain size. If the matter transport is controlled by diffusion in the liquid, it is diffusion controlled solution-precipitation. The sintering shrinkage from Kingery[82] is given by:

$$\left(\frac{\Delta L}{L}\right)^3 = \frac{g_2 \delta_l \Omega \gamma_{lv} D_s t C}{RTG^4} \tag{2.14}$$

where δ_l is the liquid layer thickness, D_s is the diffusivity of the solid in the liquid, g_2 is the geometric constant.

The final stage of liquid phase sintering is driven by the residual porosity in the liquid, however, the densification rate decreases significantly. Microstructural coarsening by the Ostwald ripening becomes the dominant process. In the final stage, the porosity is less than 8%. If the pores are treated as isolated near spheres, the densification rate is given by[85]:

$$\frac{d\rho}{dt} = \frac{12\Omega D_s C}{RTG^2}\beta\left(\frac{4\gamma_{lv}}{d_P} - P_G\right) \tag{2.15}$$

where ρ is the relative density, β is the pore density factor, P_G is the gas pressure, d_P is the pore size.

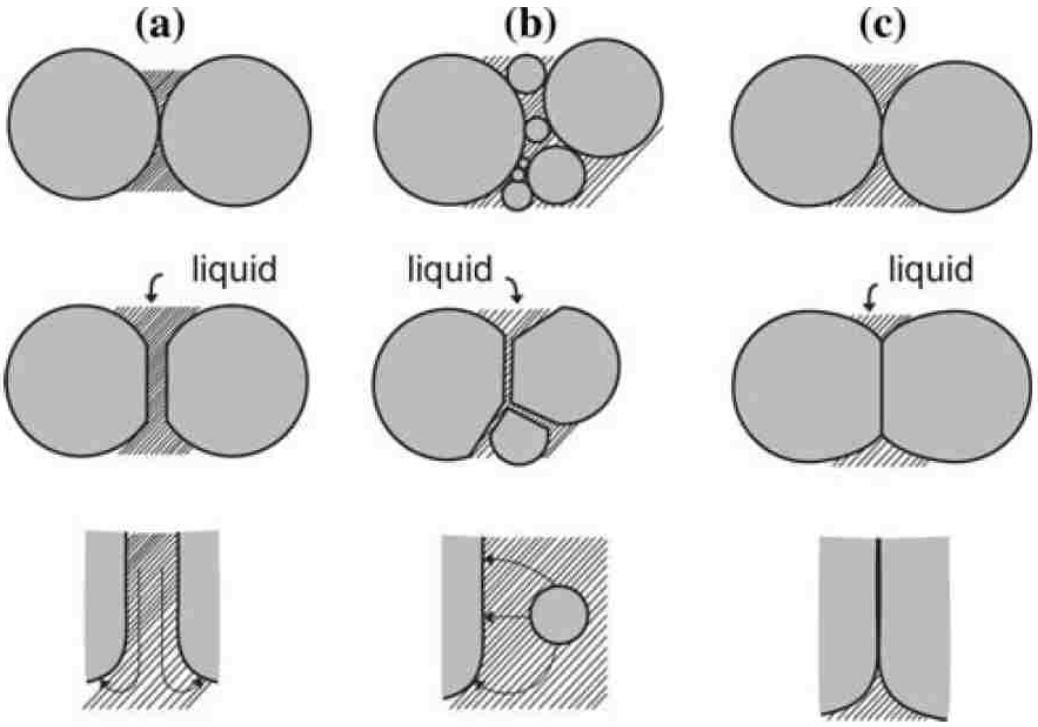

Figure 2.6: The three mechanism for densification during solution-precipitation in liquid phase sintering: (a) contact flattening, (b) Ostwald ripening, (3) solid-state bonding. (taken from R. M. German[84]).

2.2.3 Viscous sintering

For sintering of glassy materials, the mechanism of viscous flow is most significant[86]. The definition of viscous flow is given by[87]:

$$f = \eta\dot{\varepsilon} \tag{2.16}$$

where f is the acting stress, η is the viscosity, $\dot{\varepsilon}$ is the strain rate. For the occurrence of viscous flow, the stress is produced by surface tension. In the case of metals, viscous flow may not be observed, and the rate of sintering by the mechanism of viscous flow is much slower than that by volume diffusion. In the case of glass materials, the viscosity is very low at high temperature, and the sintering rate due to viscous flow should be much faster.

To model the sintering process analytically, three stages are used to define the process: initial stage, intermediate stage, and final stage. In the sintering of amorphous materials, the initial stage is characterized by rapid interparticle neck growth. Those sharp neck regions become smoothed with a network of inter-connected pores in the intermediate stage. In the final stage, only a uniform fluid with isolated pores exists[88]. Frenkel[89] introduces a two spheres model for the initial stage regarding the neck growth rate between two spherical particles in contact. Frenkel has shown that if the bonding of two spheres occurs by viscous flow, the rate of initial neck growth is given by

$$\frac{x}{R} = \left(\frac{3\gamma}{2\eta r}\right)^{1/2} (t)^{1/2} \tag{2.17}$$

where R is the radius of the sphere, x is the distance between the center of the sphere and contact line, t is the time, r is the negative radius of the curvature in contact of the two spheres. The shrinkage rate is determined by:

$$\frac{\Delta V}{V_0} = \frac{3\Delta L}{L_0} = \frac{9\gamma}{4\eta R} t \tag{2.18}$$

Scherer[90, 91] introduced a cylindrical model for the intermediate stage. An ideal cubic array of cylinders densifies by viscous flow driven by the reduction of surface energy in his model, which can be applied for sintering of materials with initial low density. The theory of viscous flow of Frenkel has been developed in the works of Mackenzie and Shuttleworth[86, 92]. Mackenzie and Shuttleworth consider an ideal large body with closed spherical pores in the final stage, and the relationship with the time and density are derived as:

$$\frac{\gamma n^{\frac{1}{3}}}{\eta}(t - t_0) = \frac{2}{3}\left(\frac{3}{4\pi}\right)^{1/3} \int_0^{\rho} \frac{d\rho}{(1-\rho)^{\frac{2}{3}}\rho^{\frac{1}{3}}} \tag{2.19}$$

where n is number of pores per unit volume, ρ is the relative density, t_0 is an arbitrary chosen constant corresponding to $\rho = 0$.

2.2.4 Non-reactive liquid phase sintering

Ewsuk et al. proposes a non-reactive liquid-phase sintering model to explain to sintering behavior of low temperature sintering ceramic filled glass composites [74, 75]. According to this model, the densification process includes three stages: glass redistribution, grain rearrangement and viscous sintering. The microstructure evolution of the three stages is shown in Figure 2.7.

The driving force in all three stages is to reduce the total volume free energy of the system. In the first stage, the driving force is the reduction of higher energy solid-solid and solid-vapor interface and creation of lower energy solid-liquid interfaces. The sintering stress or driving force, DF, in glass redistribution is described as:

$$DF_{Redis} = \frac{\gamma_{lv} cos\theta}{r} \tag{2.20}$$

where r is the radius of the curvature of the cylindrical pore channels. γ_{lv} is the glass surface tension. θ is the wetting angle.

As shown in Figure 2.7, the glass becomes liquid in the first stage and fills the capillary pore channels between the ceramic particles in the ceramic-rich region. No densification occurs in this stage. For a glass with viscosity, η, the time, t, required to

infiltrate the cylindrical pore channels with radius, r, a distance, h, in the initial stage is defined as:

$$t_{Redis} = \left[\frac{h\pi}{2}\right]^2 \left[\frac{2\eta}{r\gamma_{lv}cos\theta}\right] \tag{2.21}$$

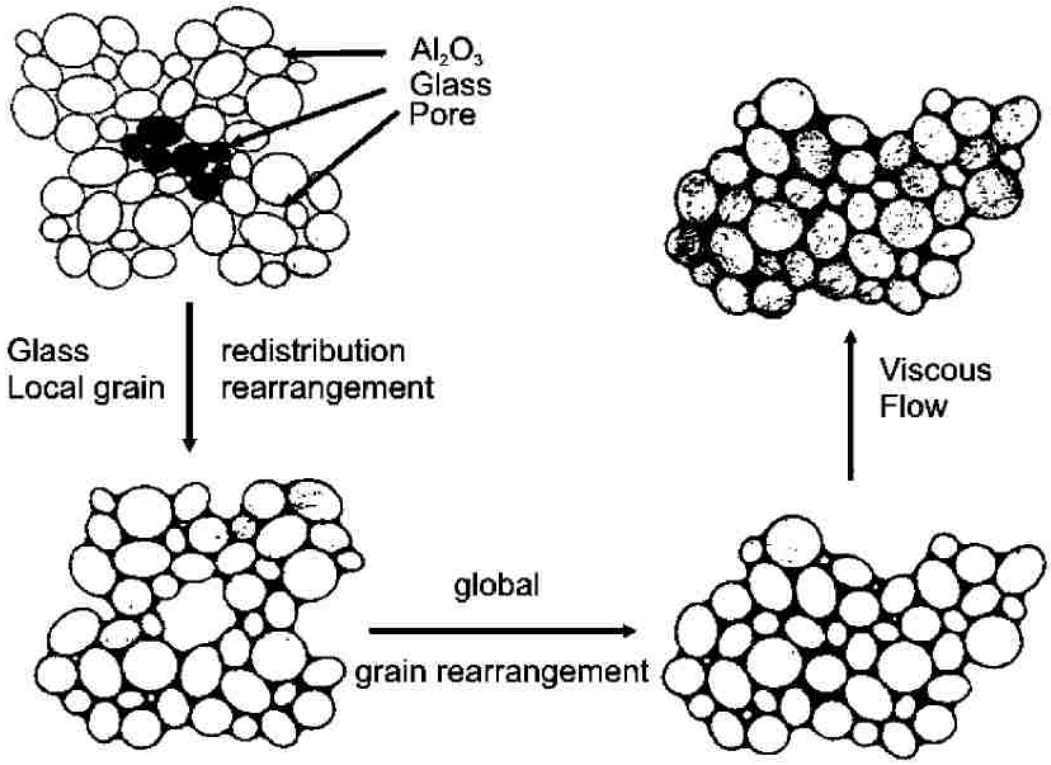

Figure 2.7: Microstructure evolution of the three stage in nonreactive liquid phase sintering model proposed by Ewsuk et al. Reprinted from the reference [74].

The driving force in the intermediate stage is to balance the force on the filler particles caused by solid-vapor, solid-solid and liquid-vapor interfaces. The grain rearrangement force, F_{grain}, equals to the force drawing the ceramic filler into glass, F_1, minus the force drawing the particle into adjacent pores, F_2:

$$F_{grain} = F_1 - F_2 = 2\pi\gamma_{lv}Rsin(\varphi + \theta) - 2\pi\gamma_{lv}\frac{R^2}{r}sin\varphi \tag{2.22}$$

where R is ceramic particle radius, and φ is the geometric factor related with the solid-vapor-liquid intersection.

When $\varphi = 90^o$, the maximum force F_{grain} is achieved. At the onset of the intermediate stage, strong grain rearrangement force favors pores closure. In a composite containing a good wetting glass, at the end of intermediate stage, the glass encompass the ceramic filler and only gross pores exists with φ reaching to 0^O eventually. The intermediate stage is responsible for the main densification, and the density increases from 65% to ~90% of theoretical density and the gross pores are closed.

In the final stage, only glass incorporated pores exist and there is no solid-vapor interface. The driving force for the first and intermediate stages disappears. The densification is controlled by viscous flow. The driving force for elimination of spherical pores is defined as:

$$DF_{viscous} = \frac{2\gamma_{lv}}{r} \tag{2.23}$$

where r is the radius curvature of the assumed spherical pores. For ceramic filled glass with dispersion viscosity, η_s, the time required to eliminate the spherical pores, $t_{viscous}$, has the expression:

$$t_{viscous} = \frac{2r\eta_s}{\gamma_{lv}} \tag{2.24}$$

The relationship between the dispersion viscosity and fraction packing density of the filler particles, $\emptyset$, is described by:

$$\eta_{relative} = \frac{\eta_s}{\eta} = \left(1 + \frac{k}{\frac{1}{\emptyset} - \frac{1}{\emptyset_{max}}}\right)^2 \tag{2.25}$$

where $\emptyset_{max}$ is the maximum packing density of the ceramic filler, and k is a constant. The dispersion viscosity plays essential role in the time required to eliminate the residual 10% enclosed pores. To ensure high densification, glass with low viscosity is required for

ceramic filled glass with high filler concentration. Likewise, glass with high viscosity is acceptable for composites with low filler concentration.

In this model, both low viscosity and low wetting angle are necessary to obtain high densification for ceramic filled glass. The glass wets the filler in the first and second stage of sintering and low viscosity glass fills the gross pores in the final stage. The viscous flow is only responsible for the final stage during the sintering. For non-wetting behavior ($\theta > 90^{O}$), and then $\cos\theta < 0$, and it further leads to repulsion force $DF_{Redis} < 0$, which indicates the glass can't fill the capillary pores between the filler ceramic. Glass redistribution will not occur for non-wetting glass, and therefore no shrinkage takes place; instead of that, swell may happen. Ewsuk et al. described a composite with a non-wetting behavior exhibits poor densification in comparison with a glass with good wetting behavior [75].

Kemethmuller et al. 's work[73] explains densification for glass-ceramic composite occurs by viscous flow although the glass does not wet the ceramic filler in the entire temperature range. For sintering of glass-ceramic composite with glass volume higher than 60%, the effect of the capillary force can be neglected and the wetting behavior is not decisive for the densification. The sintering process is predominantly controlled by the viscosity of the glass independent of the wetting behavior of the glass on the filler. The glass grains melt at first with sintering temperature increase, and then the glass fills the pores by viscous glass flow. The viscosity of the glass during sintering is the most important parameter for full densification. The schematic densification mechanism is shown in Figure 2.8.

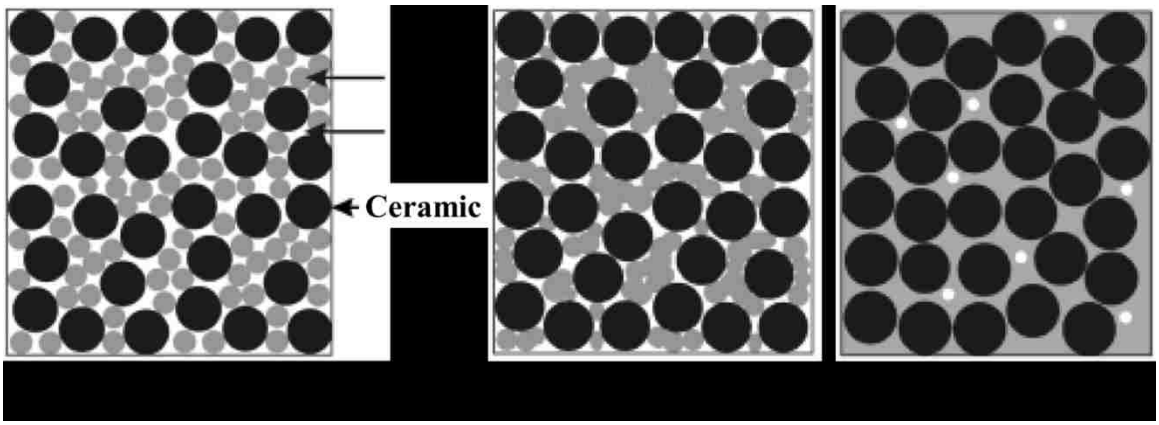

Figure 2.8: Densification process of ceramic-filled glass composite by viscous flow. Reprinted from the reference[73].

2.3 Oxygen sensing for biological and microfluidic applications

Cells consume the nutrients and oxygen to produce cellular energy, so oxygen consumption is a very important index of the cell activity. Microfluidic oxygen sensing has been used to analyze the physiological response of the cells on exposure of chemical and physical stimulations[39, 40]. Nutrients and oxygen supply are also very important for tissue engineering which emerges for the needs of the replacement of damaged or repaired tissues. Assessment of oxygen consumption and demand for the tissue is also of great importance[93]. Two common microfluidic techniques to detect dissolved oxygen in small sample volumes are luminescent optical sensing and electrochemical sensing. The mechanism of the optical oxygen sensors is based on the fact that the luminescent light emitted from the sensor is quenched in a concentration-dependent manner[94]. Fluorescent oxygen sensors have been introduced for real-time monitoring of the oxygen distribution in aqueous solutions and in tissue[95]. Electrochemical sensing mainly manifests as Clark-type oxygen sensor. Clark-type oxygen sensor is a kind of oxygen sensor containing Clark oxygen electrode which takes advantage of electrochemical reaction involving

oxygen. It has been used to monitor and analyze respiration of mitochondria oxidative enzymes, and oxygen partial concentration in blood, *in vitro* organ respiration, respiration of aquatic organisms and photosynthesis of aquatic plants[39, 40, 96-99].

2.3.1 Luminescent oxygen sensor

One type of optical oxygen sensor is based on the quenching of fluorescence of the fluorescent dyes in the presence of the oxygen. The processes involved in the fluorescence-quenching systems are in the following processes[100]:

$$M + h\nu \rightarrow M^* \quad \text{Photon absorption } (I_a) \tag{2.26}$$

$$M^* \rightarrow M + h\nu \quad \text{Luminescence } (k_r) \tag{2.27}$$

$$M^* \rightarrow M + \Delta \quad \text{Nonradiative decay } (k_{nr}) \tag{2.28}$$

$$M^* + O_2 \rightarrow M + O_2^* \quad \text{Collisional quenching, no emission } (k_q) \tag{2.29}$$

The presence of a quencher O_2 will consume the molecule in the excited state M*, which will results in the more rapid depletion of the excited-state population. It manifests as either a decrease in the steady-state luminescent intensity or as a shorter emission decay time. The change of fluorescence intensity and lifetime can be used to quantify the concentration of analyte.

For luminescent oxygen sensor, the oxygen molecule acts as a quencher. Stern-Volmer equations describe the relationship between the fluorescence intensity I or lifetime τ as the following equations[101-103]:

$$\frac{I_0}{I} = 1 + K_{SV}^{S}[O_2] = 1 + K_{SV}^{G} pO_2 \tag{2.30}$$

$$\frac{\tau_0}{\tau} = 1 + K_{SV}^{S}[O_2] = 1 + K_{SV}^{G} pO_2 \tag{2.31}$$

$$K_{SV}^{S} = k_d^s \tau_0 \qquad K_{SV}^{G} = k_d^G \tau_0 \tag{2.32}$$

where K_{SV}^{S} and K_{SV}^{G} are the Stern-Volmer quenching coefficient for solution and gas respectively; $[O_2]$ is the oxygen concentration; pO_2 is the partial pressure of oxygen gas; I_0 and τ_0 are the fluorescence intensity in absence of the oxygen respectively; k_d^S and k_d^G are the bimolecular quenching constants for solution and gas respectively.

The operation of luminescent based oxygen sensor is based on the phenomena of luminescent quenching by oxygen. Since the oxygen quenches the luminescence in the intensity and lifetime, there are two inherently different methods to measure the oxygen concentration by the luminescent probes.

The first method to determine the oxygen concentration is through measuring the luminescent intensity directly. Figure 2.9 shows simplified example setup for intensity-based optical oxygen sensing. The luminescent dye is excited by the filtered light from excitation source, which is matched with the excitation spectrum of the luminescent dye. The emitted luminescence passes through a filter to remove the extraneous light, and is detected by the detector probe. The advantages of this technique are simplification of the setup and compatibility with standard fluorescent microscopy equipment and techniques. However, intensity-based sensing has several disadvantages, which include sample absorption or scattering, detection optics and excitation light, susceptibility to

photobleaching and leaching, intensity dependence on dye layer concentration, film thickness, light-source intensity and the efficiency of transmission optics[100, 104, 105].

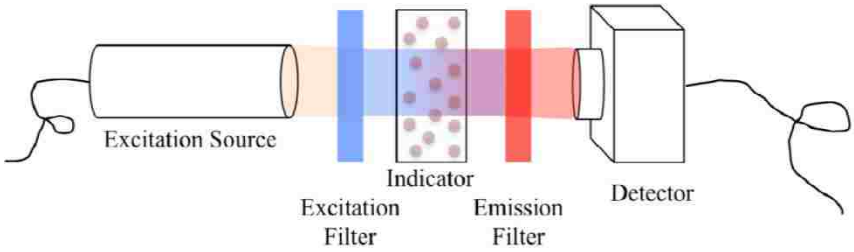

Figure 2.9: Simplified example setup for intensity-based optical oxygen sensing. Reprinted from the reference[104].

The second method is based on the detection of the luminescent lifetime in either time domain or frequency domain. The advantage of the luminescent lifetime measurement is inherent stability. The most commonly used lifetime-based detection method is based on the "pulse to and gate" method as shown in Figure 2.10.

In general, the excitation light is applied by a square-wave pulse. And the lifetime of the luminescence in time domain is determined by the equation[104]:

$$\tau = \frac{t_2 - t_1}{ln\left(\frac{A_1}{A_2}\right)} \tag{2.33}$$

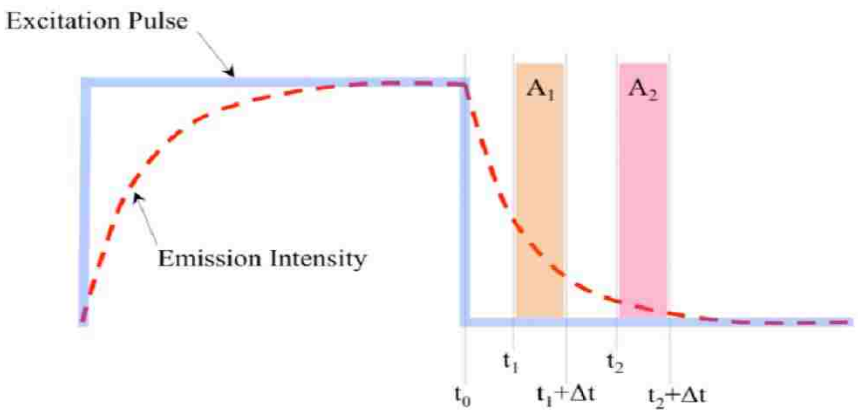

Figure 2.10: Illustration of "pulse-and-gate" time-domain luminescence lifetime detection. Reprinted from the reference[104].

The fluorescent lifetime can also be determined in frequency domain by the calculation the phase shift (θ) between the reference signal (modulated excitation light) and the fluorescent detection signal via phase-based fluorescent lifetime detection. The lifetime τ and phase shift (θ) are related by the equation[106]:

$$\tan(\theta) = 2\pi v\tau \tag{2.34}$$

where v is the modulation frequency. This method uses one window during the excitation pulse and the other after the pulse to determine the phase shift. The optimal modulation frequency can be determined from the τ_0 and τ (unquenched and quenched lifetime) using the equation[104]:

$$2\pi v = \frac{1}{\sqrt{\tau_0 \tau}} \tag{2.35}$$

The disadvantages of the frequency-domain lifetime measurements are the need for the emission filter and incapability to separate the luminescent background.

This assay has been used to monitor the viability of the cells under the treatment of the toxic agents and under the influence of the physiological inducer such as cell death[107]. The method can be used to determine cell viability and cell growth as a predictable, reliable, and fast high-throughput technique[107]. The optical oxygen sensor has also been designed to monitor the respiration rate of cells in localized environment, such as microwell, or microchannel, a wide range of biological applications in cell-based biosensing, toxicology, and drug discovery[106, 108]. Microfluidic functions for cell culture can be integrated with luminescent oxygen sensor through the technique of soft lithography, which includes casting transparent and biocompatible PDMS structures with closed microfluidic channels and chambers bonded to another substrate[109]. Those kinds of microfluidic device has been used to culture different types of cells in interconnected chambers, trap single cell in defined environment to evaluate the oxygen consumption rate[110, 111], provided a platform for simulating animal testing under chemicals and pharmaceuticals[112], control and quantify the oxygen gradient in the cells' environment[109, 113]. Oxygen gradients in engineered tissue have also been determined by using a fluorescent sensor[94]. Figure 2.11 shows an illustration of the microfluidic device with integrated optical oxygen sensor.

The advantages of this optical oxygen sensor are lack of electrical connection, no consumption of oxygen molecule, and longtime stability due to inherent properties when using luminescence lifetime detection technique[114].

However, the optical oxygen sensor requires setup of optical detection systems. In most cases, the luminescent indicator for optical oxygen sensor uses shortwave excitation and suffers from small Stroke shift, which leads to requirement of complex measurement

instrumentation[115]. The optical oxygen sensors also require the immobilization of the appropriate reagent (luminescent dye) on or near the optical fibre or waveguide. Those methods for immobilization are often complex, in most case, lack of reproducibility[116]. A general technique for fabricating low cost, reliable oxygen sensor needs to be developed.

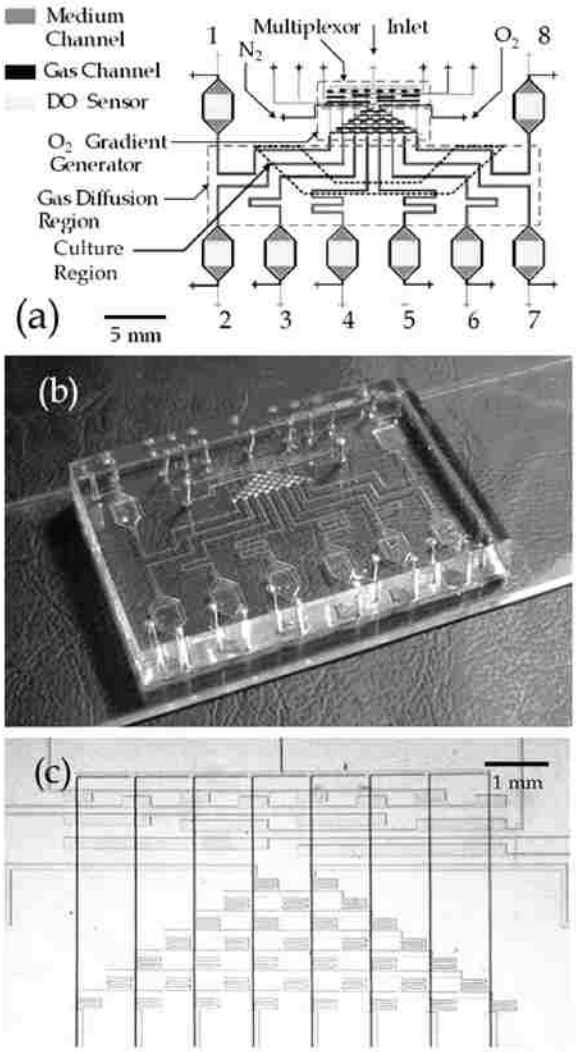

Figure 2.11: (a) Illustration of the microfluidic device with integrated optical oxygen sensor, (b) Image of the fabricated device, (c) Microstructure of the microfluidic multiplexor and oxygen concentration gradient generator. Reprinted from the reference[109].

2.3.2 Electrochemical amperometric sensing: Fundamentals of electrochemistry

Electrochemical analysis has been studied for centuries. It has been used to study the relationship between electricity and chemistry, or measure the electrical quantities, such as current, potential, and charge, and their relationship to chemical parameters, such as rate constants, equilibrium values, ionic concentration, and reaction mechanism of numerous chemical systems[117, 118].

Electrochemical reactions takes place at the electrode-solution interface, and the electrode surface is the junction between an ionic conductor and an electronic conductor. Electrochemical measurement systems typically contain three electrodes: a working electrode, a counter electrode and a reference electrode. The working electrode corresponds to the targeted analytes. The size is usually kept the smallest, so the current density is highest at the working electrode and most of the potential drops at the vicinity of working electrode. The potential of reference electrode is constant and independent of the solution. Measurement of electrochemical system is usually based on three electrode configurations in order to reduce parasitic contributions of the electrode system, including resistive drop in the media due to current or polarization of electrode surface. Since there is no or little current flow between working electrode and reference electrode, the potential measured between those two electrodes is mainly the potential drop at the working electrode. The voltage potential between the working electrode and reference electrode is controlled by dynamically adjusting the potential across working electrode and counter electrode[119].

Two principal types of the electroanalytical measurements with three electrode configurations are potentiometric and potentiostatic[117]. The potentiometric method measures the resultant voltage between the working electrode and reference electrode by forcing a current from working electrode to the counter electrode. The controlled-potential (potentiostatic) technique is based on a dynamic situation, and the resultant current due to an electron-transfer reaction is measured under the electrode potential drive. The current response is related to the concentration of the targeted analyte.

The study of electrochemical systems is based on the basic principles of thermodynamics and fluid mechanics. Thermodynamic is used to study the chemical potential at different states, and fluid mechanic is to determine the transport of the analytes. The basic reaction of electroactive species is either oxidation or reduction according the following redox process:

$$\mathrm{O} + ne^{-} \leftrightarrows \mathrm{R} \tag{2.36}$$

where O and R are the oxidized and reduced forms, respectively. ne^{-} reperents the number of transferred electrons during each reaction. Such reaction will occur in the potential region that makes the electron transfer thermodynamically favorable.

If the electrochemical systems obey the law of the thermodynamics, the potential of the electrode can be used to determine the concentration of the electroactive species at the electrode surface according to the Nernst equation:

$$E = E^{0} + \frac{2.3RT}{nF} log \frac{C_o(0,t)}{C_R(0,t)} \tag{2.37}$$

where E^0 is the standard potential for the redox reaction. R is the universal gas constant (8.314 $JK^{-1}mol^{-1}$). T is the Kelvin temperature. F is the Faraday constant (96,487 coulombs). $C_o(0,t)$ and $C_R(0,t)$ are the concentration of the oxidized species O and reduced species R at the electrode surface at time t. The Nernst equation describes the relationship of the equilibrium potential of the electrochemical systems with the concentration of the ions in the systems. This equation has been used to exploit the fabrication of pH sensor where the equilibrium potential is linearly related with the log of the ratio of the hydrogen ions in the inner and outer solutions across the membrane.

The mass transport of electroactive species can occur by three different mechanisms: diffusion, convection and migration. Diffusion is the spontaneous transport of the species from regions of high concentration to the region of low concentration under the influence of the concentration gradient. Convection is the movement of species to the electrode under a physical influence such as stirring or flowing the solution, rotating or vibration the electrode. Migration is the movement of the charged species within an electrical field. The overall flux (J) for the transport of the chemical species at a fixed point (x) and time (t) is determined by a differential equation[117]:

$$J(x,t) = -D\frac{\partial C(x,t)}{\partial x} - \frac{zF}{RT}DC\frac{\partial \Phi(x,t)}{\partial x} + C(x,t)V(x,t) \qquad (2.38)$$

where D is the diffusion coefficient (cm^2s^{-1}), z and C are the charge and the concentration respectively. $\partial C/\partial x$ is the concentration gradient. $\partial \Phi/\partial x$ is the potential gradient. $V(x,t)$ is the hydrodynamic velocity in the x direction. The current (i) is directly proportional to the flux (J):

$$i = -nFAJ \tag{2.39}$$

where A is the electrode surface.

If the transport of electroactive species is limited by the diffusion, the flux equation is reduced to a simplified equation only dependent on the concentration gradient, which is Fick's first law:

$$J(x,t) = -D\frac{\partial C(x,t)}{\partial x} \tag{2.40}$$

Many electrochemical systems are controlled by the diffusion process.

If the diffusion coefficient is independent of the spatial position, the Fick's second law for species O is presented as:

$$\frac{\partial C_O(x,t)}{\partial t} = D_O\frac{\partial^2 C_O(x,t)}{\partial x^2} \tag{2.41}$$

Fick's second law has been extensively used to predict the spatial distribution of species concentration with time in one dimensional case. This equation can provide specific solution for situation constrained by boundary conditions.

Diffusion limited response under semi-infinite boundary condition

For an experiment in which the potential instantaneously changes from a value where only electrolysis occurs to a value where the current is controlled by mass transport, the current-time response can be predicted qualitatively by solving Fick's second law using constrained boundary conditions. If planar electrode and unstirred

condition is assumed, the diffusion-limited current (i) and the concentration profile ($C_o(x,t)$) according to the equation 2.41 can be quantified under the three boundary conditions:

$$C_O(x,0) = C_O^* \tag{2.42}$$

$$\lim_{x\to\infty} C_O(x,t) = C_O^* \tag{2.43}$$

$$C_O(0,t) = 0 \quad (for\ t > 0) \tag{2.44}$$

The first constrained condition (2.42) describes the homogeneity of the solution at the beginning of the experiment at $t = 0$. The second condition (2.43) expresses it is semi-infinite condition, and the concentration of species O is constant in a region distant from the surface of the working electrode. The third expresses condition (2.44) is that all analytes reaching the working electrode are consumed immediately and the concentration at the working electrode is zero. In this case, if a large enough electrical potential is applied to the working electrode, the reaction at the electrode is limited only by the diffusion of the analyte to the electrode.

The equation 2.41 can be solved using boundary condition from equation 2.42 to 2.44. The concentration profile of species O is described as[118]:

$$C_O(x,t) = C_O^* \left\{1 - erfc\left[\frac{x}{2(D_O t)^{1/2}}\right]\right\} \tag{2.45}$$

Or

$$C_O(x,t) = C_O^* erf\left[\frac{x}{2(D_O t)^{1/2}}\right] \tag{2.46}$$

The current-time response is determined by:

$$i(t) = -nFAD_O \left[\frac{\partial C_O(x,t)}{\partial x}\right]_{x=0} \tag{2.47}$$

Finally, the calculated current is:

$$i(t) = -\frac{nFA{D_O}^{1/2}C_O^*}{\pi^{1/2}t^{1/2}} \tag{2.48}$$

which is known as Cottrell equation. The Cottrell equation is particularly useful to determine the current-time response in unstirred conditions. The current gradually decreases at a rate proportional to the inverse square root of time. The reaction for the current to decrease is that the collection area remains constant but the transport distance for species to reach the working electrode is increasing with time. Figure 2.12 shows concentration profile for several time points. The concentration gradient near the electrode surface is time-dependent and gradually decreases, which also leads to the decreasing current with time. The Figure 2.13 shows the current response calculated using Cottrell equation.

In a finite, one-dimensional electrode of length L, the value of constant current after the transient state has passed can be determined by solving the following equation[120]:

$$\frac{\partial^2 C_O(x)}{\partial x^2} = 0 \tag{2.49}$$

The boundary conditions are:

$$C_O(0) = 0 \tag{2.50}$$

$$C_O(L) = C_O^* \tag{2.51}$$

The solution under the limited conditions is:

$$C_O(x) = \frac{C_O^*}{L} x \tag{2.52}$$

$$i(t) = -\frac{nFAD_0 C_O^*}{L} \tag{2.53}$$

The limiting time t_l, after which the transient time ceases can evaluated by comparing the temporary current in one-dimensional model (2.48) with the constant current given in (2.53), which gives:

$$t_l = \frac{L^2}{\pi D_0} \tag{2.54}$$

The limiting time is proportional to the square of the length and inversely proportional to the diffusion coefficient. This equation can be used to determine the limiting time for the electrode with a recess.

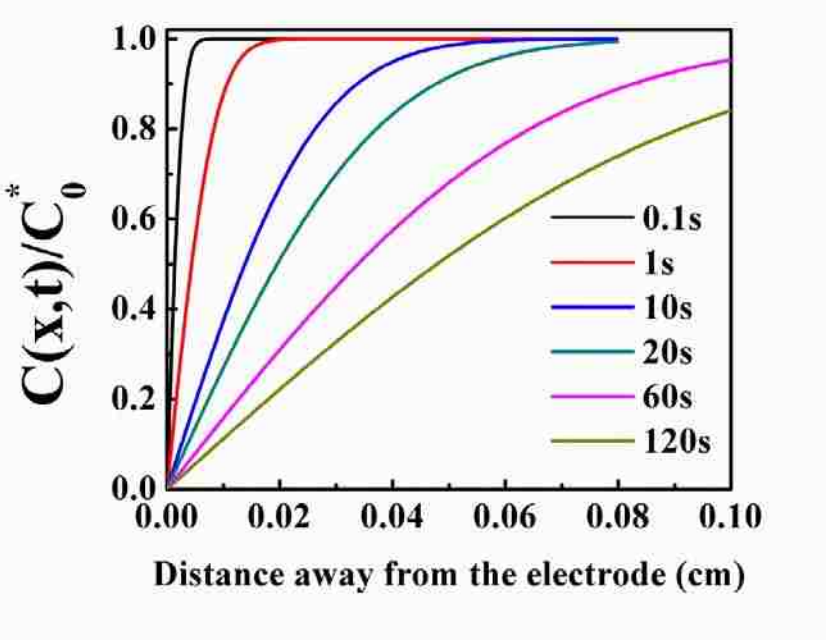

Figure 2.12: Concentration profile of species for several times after the start of Cottrell experiment, $D_O = 2.1 \times 10^{-5}\ cm^2/s$.

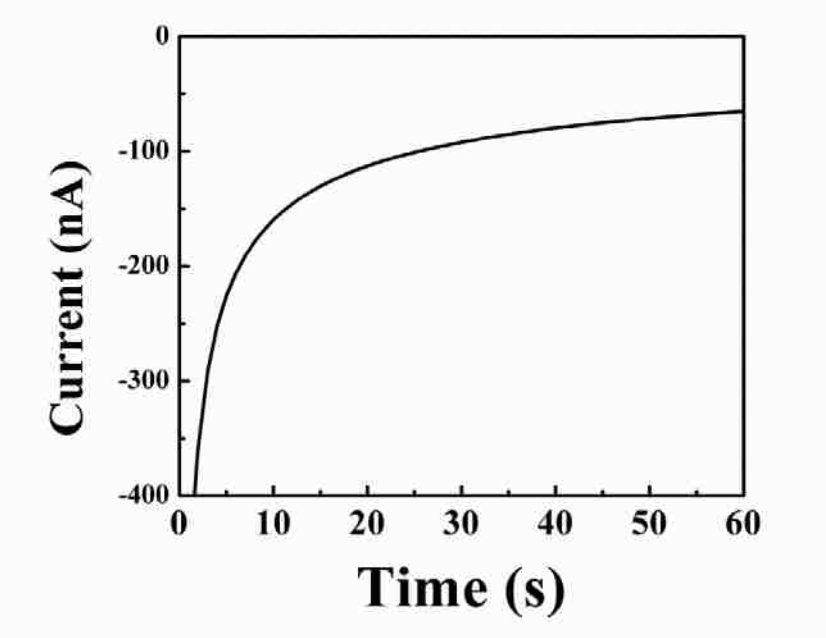

Figure 2.13: Simulated current response of species O_2 using Cottrell equation, $D_O = 2.1 \times 10^{-5}\ cm^2/s$, $A = 0.2\ mm^2$

Diffusion limited response under non-infinite boundary condition

This section will consider the response of the electrochemical systems under the condition where the electrode is undisturbed, but the stirring of the solution occurs at some fixed distance from the electrode. Transportation of electroactive species to a fixed position away from the electrode is considered, so modification of the boundary condition is needed to study the steady state current. This configuration more closely resembles the electrochemical process in the Clark-type oxygen sensor[119].

The configuration of a classic Clark-type oxygen sensor contains electrolyte underneath the gas permeable membrane, which separates the electrolyte and sample solution. This construction can be simplified as a system in which the sample solution is directly contact with the electrolyte. In this system the electrolyte has a fixed thickness and a known diffusion coefficient, while the sample solution has a different diffusion coefficient. The configuration of this model is shown in Figure 2.14.

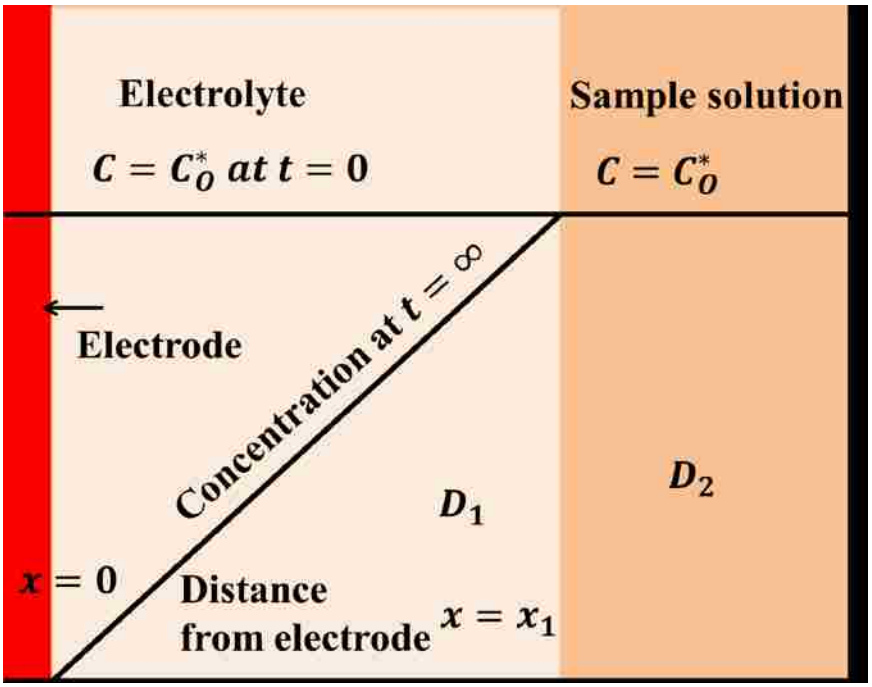

Figure 2.14: Configuration of an electrochemical system under the boundary condition at t=0 and t=∞).

Two assumptions are made for this model. The first assumption is that the flux of species to and from electrode is controlled by diffusion only within the electrolyte. The second assumption made is that the concentration of the sample in the solution is kept constant. The second condition can be realized by continuous flow of fresh sample solution or stirring the media to increase the flux of the species to the surface of the gas permeable membrane above the working electrode.

The boundary conditions of this model are listed in the following equations:

$$C_O(x, 0) = C_O^* \tag{2.55}$$

$$C_O(x = x_1, t) = C_O^* \tag{2.56}$$

$$C_O(0, t) = 0 \quad (for\ t > 0) \tag{2.57}$$

The first condition (2.55) describes that the concentration of the species in the electrolyte and sample solution is uniform (C_O^*) at $t = 0$. The second condition (2.56) expresses that the concentration at the boundary of electrolyte and sample solution is kept constant during the whole electrochemical process. The third boundary condition (2.57) states that the species is consumed immediately at the surface of the electrode and concentration is zero. The general solution for this system can be obtained through combination of the boundary conditions and the Fick's second law.

The final form of the concentration profile of the electroactive species for this system with boundary conditions in the time interval $0 < t < \infty$ and the spatial interval $0 < x < x_1$ is presented in the following equation[119]:

$$C_O(x,t) = C_O^*\left(\frac{x}{x_1}\right) + \sum_{n=1}^{\infty} \frac{2C_O^*}{n\pi} e^{-\left(\frac{n\pi}{x_1}\right)^2 D_1 t} sin\frac{n\pi x}{x_1} \tag{2.48}$$

where x_1 is the thickness of the electrolyte, D_1 is the diffusion coefficient in the electrolyte. C_O^* is the initial concentration of the species in the electrolyte and the concentration in the sample solution.

Figure 2.15 shows the simulated concentration response at different time intervals using the derived equation. The results indicate the concentration profile can reach a steady state in less than 5 s for a 20.54 μm thick Nafion 117 membrane.

The physical parameter corresponded to the concentration that can be measured is the current measured at the working electrode, which is proportional to the slop of the

concentration profile, or species flux. The expression for the time dependent current is obtained as the derivative of the concentration equation[98, 119]:

$$i(t) = -nFAD_1\left[\frac{\partial C_O(x,t)}{\partial x}\right]_{x=0} = -nFAD_1\left(\frac{C_O^*}{x_1} + \sum_{n=1}^{\infty}\frac{2C_O^*}{x_1}e^{-\left(\frac{n\pi}{x_1}\right)^2 D_1 t}\right) \quad (2.59)$$

where n is the number of electrons that transfers to the electrode per each molecule, and A is the cross section area of the electrode.

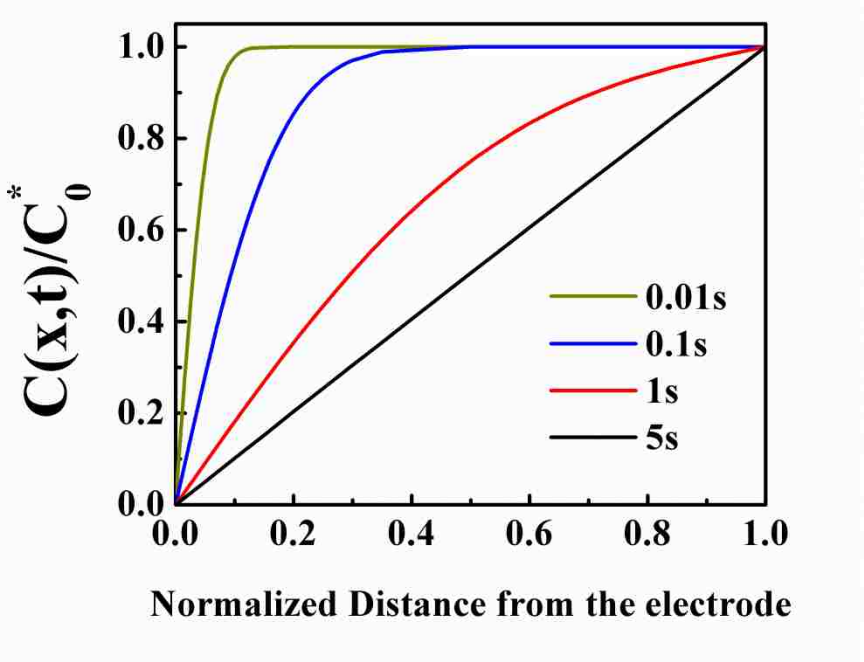

Figure 2.15: Concentration response of the simulated diffusion limited electrochemical systems. The boundary conditions are that the concentration at the electrode is zero and the concentration in the sample solution is constant. Diffusion coefficient of Nafion 117 (0.4×10^{-6} cm^2/s) [19] is used, and membrane thickness is 20.54 μm.

This equation can be used to evaluate the current response of the electrochemical systems in which the concentration of the species is at equilibrium state throughout the media before step voltage is applied. A simulation of the current response is shown in Figure 2.16. The current decreases fast at the beginning when the step voltage is applied,

which is due to the depletion of the active species at the sensitive area of working electrode. And the current gradually becomes constant, which is because the concentration profile of active species reaches a steady state with time.

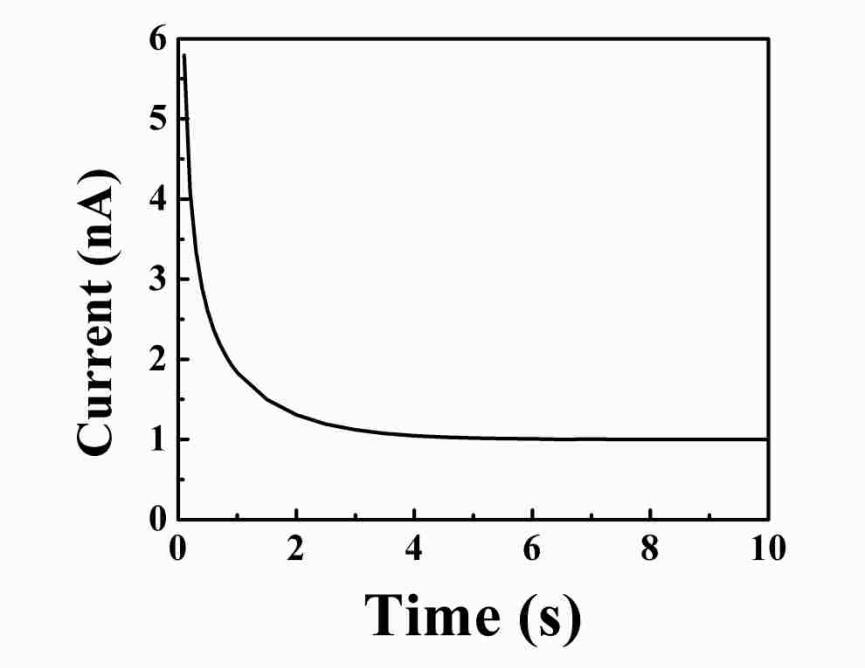

Figure 2.16: Plot of current response of the electrochemical system under diffusion limited kinetics and specific boundary conditions. Diffusion coefficient of Nafion 117 (0.4×10^{-6} cm^2/s) [19] is used, and membrane thickness is 20.54 μm. It takes 2.5 s for the current to reach 120% normalized steady state current.

2.3.3 Electrochemical sensing: Clark-type oxygen sensor

The operation of the Clark-type oxygen sensor is based on the electrochemical reduction of the dissolved oxygen and measurement of the reduction current which is proportional to the oxygen concentration. The main advantage of this sensor is that the electrode and electrolyte required for operation are encapsulated within or underneath an oxygen gas permeable membrane. This unique configuration can prevent the interference of other species in the sample solution from giving additional reduction current signal

and improve accuracy of the measurement. Usage of this membrane also allows its application in delicate biological species such as blood[41].

Various Clark cell designs include both two electrode and three electrode configurations. In both cases, dissolved oxygen is transported through the gas permeable membrane and is reduced at the working electrode. In a voltage step measurement, the reduction is carried out at high enough voltage so the reduced current is controlled by the diffusion kinetics. To minimize the time for the diffusion of dissolved oxygen to the working electrode, the working electrode should be as close as possible to the gas permeable membrane. In the two electrode configuration, the materials used for electrode should be electrochemically stable in the aqueous electrolyte under applied voltage range. However, the lifetime is still limited by the consumption of anode, and failure of this sensor occurs once the anode materials have been consumed completely[121]. The three electrode configuration has a separate counter electrode and reference electrode. This structure is used to reduce the offsets caused by parasitic potentials within the system. Although very little current exist between working electrode and reference electrode, the lifetime of this structure is still limited by the dissolution of reference electrode[122].

The electrochemical equation (2.59) derived from the fixed boundary conditions under diffusion limited condition predicts that the current is directly proportional to the species concentration when the equilibrium state is reached during the testing, as shown in the following simplified equation:

$$i(t) = -nFAD_1 \frac{C_O^*}{x_1} \tag{2.60}$$

If the species is the dissolved oxygen, we can tell the reduced current is proportional to dissolved oxygen concentration.

In 1956, the first Clark-type electrode was developed by L.C. Clark in order to continually monitor the oxygen tension of blood circulating in the heart-lung machine [123]. In this sensor, a two electrode configuration was used to detect the electrochemical signal, a platinum cathode and a silver wire as anode. A polyethylene membrane was used as the gas-permeable membrane. The cathode was pressed against the membrane to reduce the diffusion time of dissolved oxygen with a potassium chloride electrolyte as shown in Figure 2.17. The electrode gives a linear response in current flow with respect to oxygen content.

At the early stage of the development, sensors with Clark-type electrodes were fabricated in a container or glass electrode holder with a gas-permeable membrane[120], and it was difficult to further reduce the size of the sensor. In the last three decades, due to the progress of semiconductor and micromachining techniques, various miniaturized microfabricated Clark-type oxygen sensor have been developed with planar structures, as shown in Figure 2.18(b). Each microfabricated Clark cells must integrate the gas-permeable membrane, electrolyte layer and detecting electrodes. One early to incorporate the gas permeable membrane in the sensor was by intercalating a gas permeable membrane between two silicon substrates and fixing them with an adhesive[124], as shown in Figure 2.18(b).

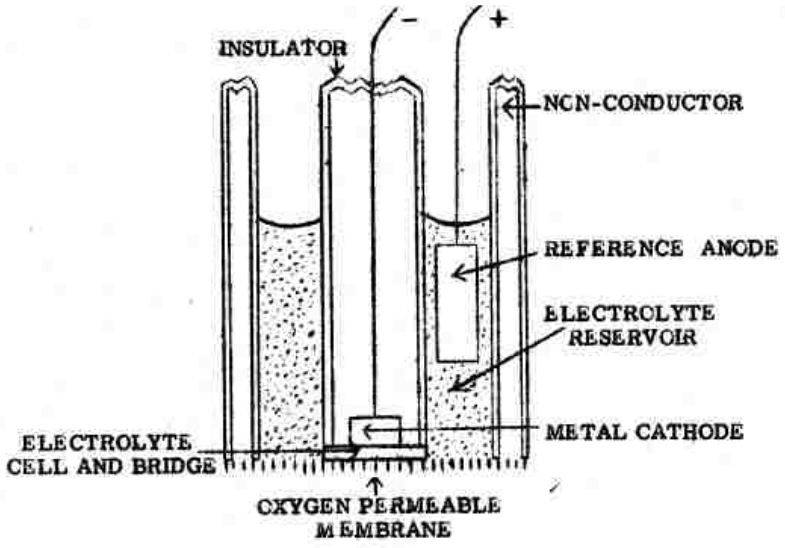

Figure 2.17: Oxygen electrode structure. Reprinted from reference [123]

The first complete microfabricated Clark-type oxygen chip was demonstrated by Koudelka using standard micro fabrication techniques[125]. The sensor was fabricated on a Si/SiO_2 substrate. It consisted of an Ag cathode and Ag/AgCl reference anode. To realize the planar structure, a hydrogel (poly 2-hydroxyethyl methacrylate, pHEMA) was used as electrolyte, and a silicone rubber membrane was used as gas permeable membrane as shown in Figure 2.18(c).

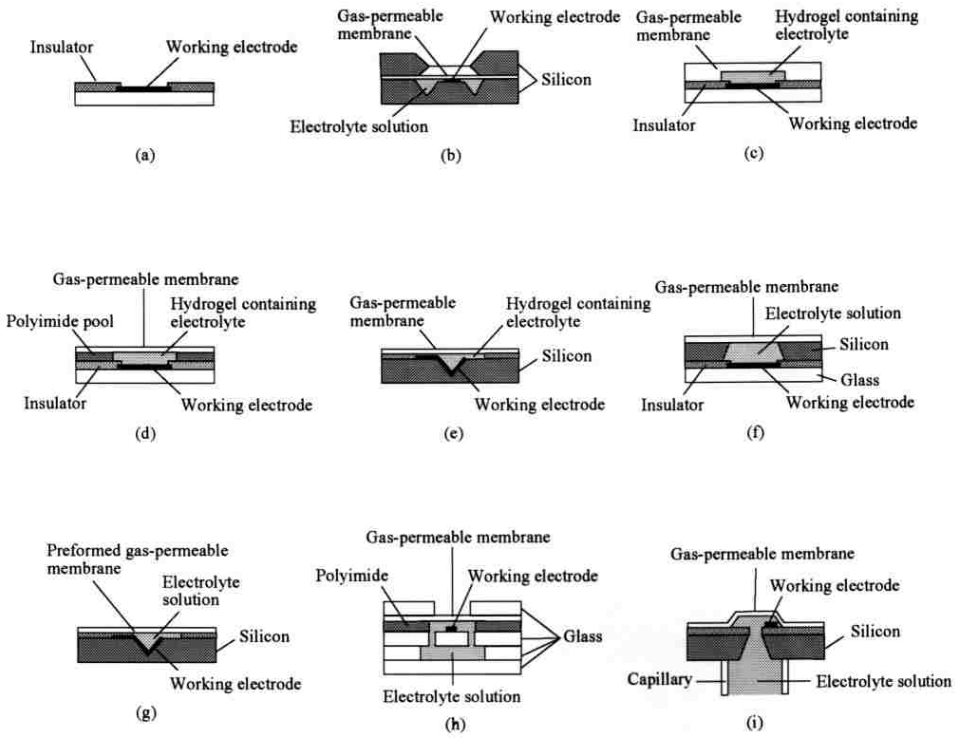

Figure 2.18: Development of Clark-type electrode. Reprinted from the reference[126]. (a) Working electrode without gas permeable membrane; (b) Working electrode with gas permeable membrane intercalated and fixed between two silicon substrate; (c) Gas permeable membrane formed on a hydrogel containing electrolyte; (d) Electrolyte gel injected in a polyimide pool; (e) Electrolyte gel in an anisotropically etched groove on a silicon substrate; (f) A gas permeable membrane adhered on a microcontainer formed on silicon and glass as substrate and an filled electrolyte solution; (g) A gas permeable membrane adhered on a microcontainer formed on silicon and an filled electrolyte solution. (h), (i) Electrolyte solution filled from the back of the substrate.

Suzuki and his co-worker made extensive progress in this silicon-based fabrication process and improved this chip by incorporating several new features[41, 122, 127-132]. They used micromachining and photolithographic techniques to fabricate miniature sensors with the three electrode configuration[127]. The stability of the sensor was improved, with the residual current reduced to less than 7%, compared with a residual current ~20% for two electrode configuration[127]. To improve the capability of steam sterilization for the sensor, fluorinated ethylenepropylene (FEP) as gas permeable membrane was bonded to the chip through thermal etching, which provides good adhesion and temperature

tolerance[130]. Electrochemical cross talk between electrodes in miniature structure always resulted in unwanted residual current and extended response time, and made the reference electrode unstable. To minimize the crosstalk, grooves only over the electrode area were made with a long narrow channel connecting the electrode[130]. They also proposed a microfabricated Ag/AgCl reference electrode structure with improved stability and lifetime[122, 131], and a polyimide protecting layer with a slit structure was coated on the center of silver electrode as shown in Figure 2.19.

To form gas the permeable membrane on an aqueous electrolyte solution, a frequently used method was incorporation of hydrogel, such as calcium alginate gel containing potassium chloride electrolyte[128], to hold the electrolyte solution[125, 128, 133-135]. In this case, the electrolyte layer and gas permeable layer were originally formed in a completely dry state, incorporation of water into the electrolyte is essential for the operation. Water can be introduced directly by osmosis just immersing the electrode in the water at room temperature. The electrode was instead activated by subjecting it to sterilization in an autoclave[136]. This structure has also been used extensively in other electrochemical sensors. A different method was to fabricate the miropool in the sensor with a polymer such as polyimide [Figure 2.18(d)][137, 138] or in a etched groove on the silicon substrate [Figure 2.18(f)][132] allowing the aqueous electrolyte solution to be filled into the recess after bonding the sensors. Some variation in the shape of the container for electrolyte solution can be seen in Figure 2.18 (i-j)[122, 130, 139-141]. The criterions to design the shape of the recess for the electrolyte solution were to minimize the crosstalk between electrodes and reduce the response time. Because the size of the container was very small, the effects of the reaction products at the working electrode and counter electrode on the

performance were depended on the distance between the electrodes and geometries of the electrodes and container. The crosstalk resulted in the extended response time, unwanted residual current and a shift of the output current. A balance between miniaturization of the sensor and minimization of the crosstalk should be considered to design the shape of the sensors.

For further miniaturization of the Clark-type oxygen sensor, a solid state proton conductive electrolyte was used to replace the aqueous electrolyte-filled compartment. The advantage was the simplicity and scalability of the fabrication and packaging procedures. The incorporation of solid state electrolyte not only lowered the size of chip but also reduced the cost and improved consistency.[44, 98].

Silicon rubber has been used predominantly as the gas permeable membrane with practical level of performance and reliability[125, 126, 135]. It shows excellent adhesion to the underlying layer or substrate and good oxygen permeability. The negative photoresist has also been used as gas permeable membrane. However, it suffered from a problem in oxygen permeability[133]. Thin PDMS membranes exhibit good oxygen permeability, and have also been used as the gas permeable membrane[39, 40, 43, 142].

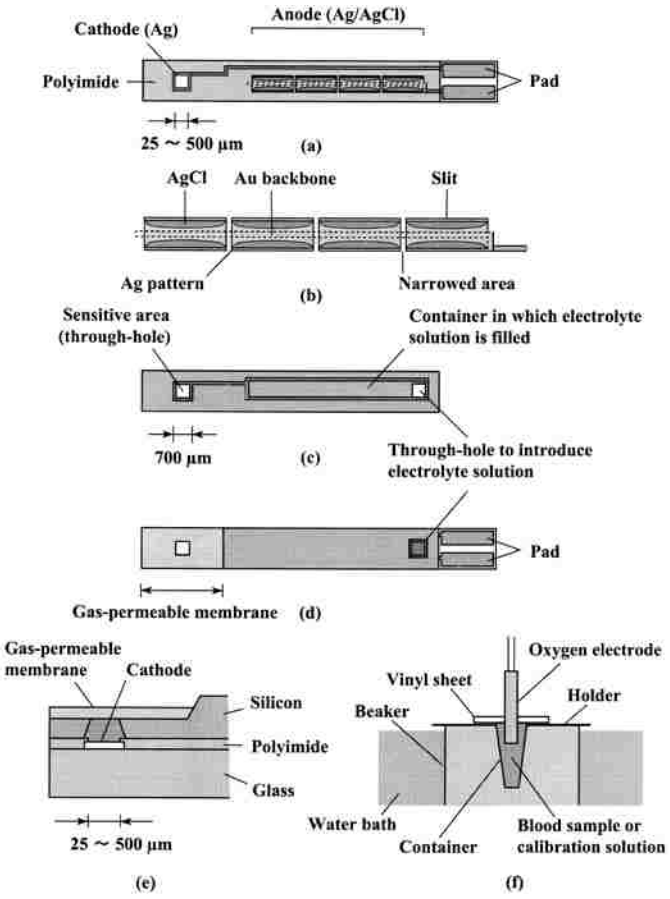

Figure 2.19: Structure of the miniature Clark-type oxygen sensor. Reprinted from the reference[41]. (a) Glass substrate with cathode and reference anode, (b) expanded view of the Ag/AgCl anode, (c) silicon substrate with the recess for the electrolyte solution, (d) completed oxygen sensor, (e) cross-section of the sensitive area, (f) experimental setup for measuring blood samples.

Recently Wu et al. constructed a glass-based Clark-type oxygen chip by incorporation of glass substrate with functional Clark-type electrode to the polydimethylsiloxane (PDMS) gas permeable membrane immobilized with a PDMS reservoir as shown in Figure 2.20[39, 40]. A photoresist was used to construct the electrolyte groove on top of glass substrate and acted as insulator at the same time. A PDMS slab with a hole was bonded to a thin PDMS gas permeable membrane by oxygen plasma, and it was placed on top of the glass substrate as reservoir for sample solution. Elements to

control temperature have also been integrated into the planar to provide constant temperature environment for measuring cellular oxygen consumption rate.

The advantage of the use of PDMS is the capability of irreversible bonding to PDMS and glass under oxygen plasma treatment, which enables good adhesion of the gas permeable membrane to glass substrate and realization of PDMS reservoir for holding sample solution. The disadvantage of PDMS as gas permeable membrane was susceptible to mechanical failure, which resulted in complete malfunction of the devices.

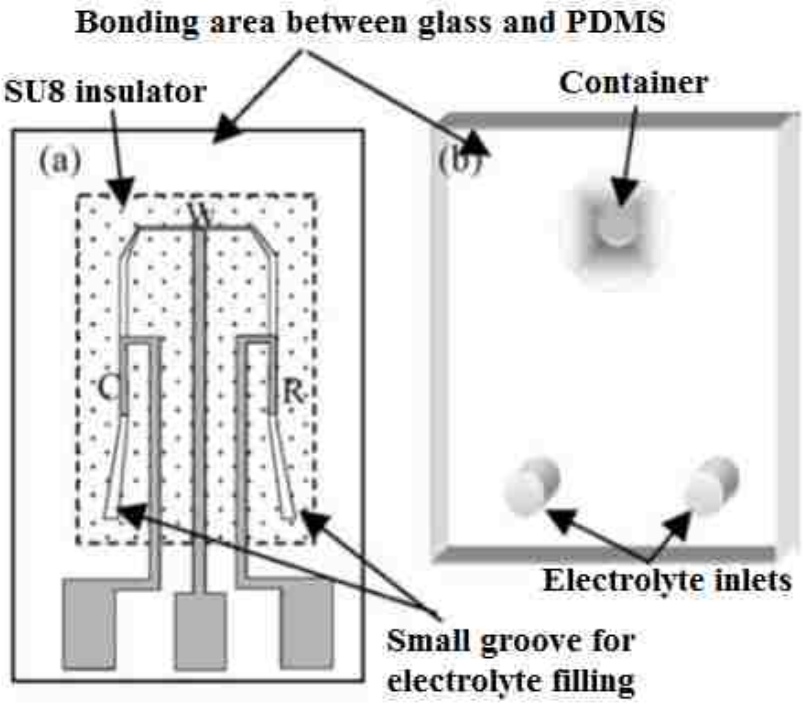

Figure 2.20: The structure of Clark-type oxygen sensor. Reprinted from reference[40]. (a) Glass substrate with three electrode and electrolyte channel made by photoresist, (b) PDMS reservoir with gas permeable membrane. C, R, W refers to counter, reference and working electrode respectively.

Gas permeable polypropylene (PP) and fluorinated ethylene propylene (FEP) polymer membranes have also been used in the Clark-type oxygen sensors[43, 130]. These

two membranes shows lower oxygen permeability compared with PDMS, and the oxygen permeability of PP, FEP, and PDMS were 1.6, 5.9, and 600 (where 1 Barrer is 1×10^{-11} $cm^3cmcm^{-2}s^{-1}mmHg^{-1}$, respectively[71]. PP, FEP membrane had longer response time as shown in Figure 2.21. Bio-inert polytetrafluoroethylene (PTFE) has also been chosen as oxygen permeable membrane, and the bonding to solid state electrolyte (Nafion) was through pulsed plasma deposition technique. It showed good oxygen permeability[98].

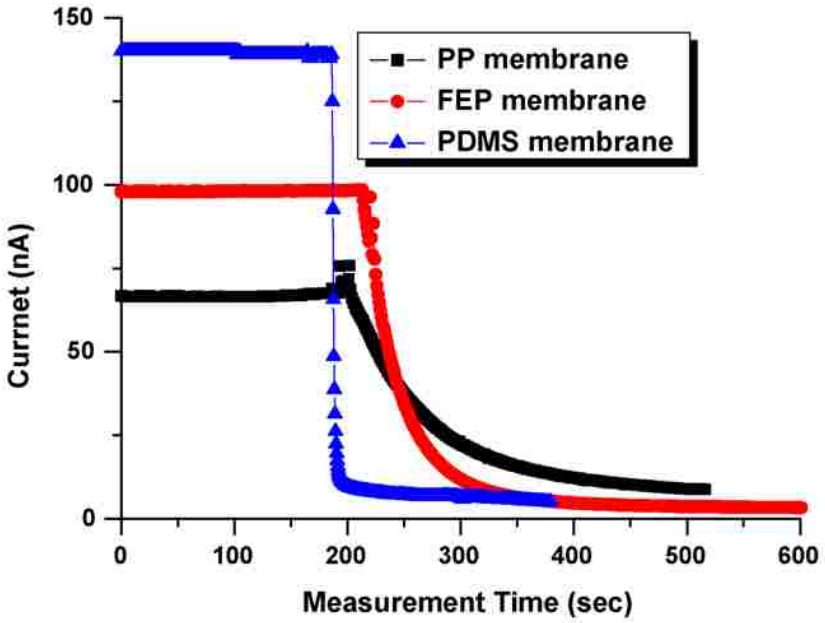

Figure 2.21: The output current results of the fabricated oxygen sensor with PP, FEP, and PDMS membrane when the sensor changes from the full-oxygen state to the zero-oxygen state. Reprinted from the reference[71].

The incorporation of a gas permeable membrane enables the use of the Clark-type oxygen sensor in the delicate and complex biological environment. Miniature sensors have been used for real-time monitoring of pO_2 in human whole blood[41, 120]. The accuracy of the values obtained was within 8% compared with a commercial blood gas analyzer[41]. In addition, the fabrication of Clark-type oxygen sensor has been integrated

with other sensing modules, such as pCO_2 electrodes and pH electrodes[134, 135, 138, 143]. This type of sensors has been used to simultaneously monitor pO_2, pCO_2, and pH at the same time in the human blood.

The Clark-type oxygen sensors have also been used to measure the oxygen consumption rate of tumor cells *in vitro*, and showing unique opportunities to demonstrate the effects of a given treatment on the respiratory rate. They have also exhibited high sensitivity in studying enzyme and chemical reactions involving consumption of oxygen[144]. In Wolf's studies, a Clark oxygen electrode was externally inserted into the fluid exit port of a cell chip to measure the respiration rate of tumor cells under drug exposure. Another sensor was also integrated into the cell chip to monitor the cellular metabolism and pH value[145-147]. Heimburg et al. integrated a Clark-type sensor in a thermostatic chamber to investigate the oxygen consumption rate of cells in undifferentiated and differentiated states. The results indicated the differentiated cells had higher oxygen consumption than immature ones[148]. The respiratory rate of cells in suspension or attached cells with or without influence of chemicals, such as Carbonyl cyanide p-(trifluoromethoxy) phenylhydrazone (FCCP), was successfully demonstrated using Clark-type oxygen sensors[39, 40, 43, 142].

Chapter 3 A biocompatible low temperature co-fired ceramic substrate for biosensors

3.1 Introduction

Microfluidics offer many advantages such as portability, low cost, fast response time and integration with other miniaturized features. The capability of microfluidic systems fills the technological requirement for portable point-of care medical diagnostic systems in global public health[1, 2]. Glass, silicon, polymer, and multilayer ceramic substrates and processing methods have all successfully been applied for the development of commercialized of microfluidic systems. The continued development of LTCC over the last two decades has resulted in a promising alternative technology for the fabrication of the microfluidic devices. LTCC materials are chemically inert, possess high temperature stability, exhibit high mechanical strength, allow the fabrication of three dimensional features, and are able to integrate functional components[46]. A variety of microfluidic LTCC devices have been successfully fabricated and reported for applications in biosensing[33, 34] environmental sensing[26, 27], and in point-of-care diagnostic systems. LTCC materials of various compositions from commercial suppliers have significantly different properties which can be vary dramatically between compositions[68]. Specifically, the chemical stability and leaching behavior of commercial LTCC materials in aqueous solutions can vary drastically[37]. In the current work, the key characteristics and advantages of LTCC materials are extended to include biocompatibility.

Biocompatibility is neither a universal property nor innate characteristic of a material or component. Rather it defined as the suitability of a material for use in a specific biological application. In the current work, biocompatibility is evaluated as the suitability of the material to perform as a substrate for the sustained in-vitro culture of endothelial cells. The intended application is for the development of biosensors incorporating live endothelial or other adherent human cell lines for cell based or cell enabled biosensing applications. In this context, the biocompatibility of the current LTCC formulation is expected to be dependent on the elemental composition, solubility, crystalinity, and atomic structure[149]. In addition, the substrate surface must support the attachment and proliferation of a target cell line. The compositional and microstructural complexity of commercial LTCC formulations makes it difficult to understand and tailor the biocompatibility of these materials. For these reasons, a custom LTCC formulation has been developed specifically with the specified application in mind.

LTCC materials are primarily glass-ceramic composites, and several methods to fabricate LTCC have been reported in the literature. These methods include recrystallizable glasses[56, 58] and mixtures of ceramic with a low melting temperature glass[57, 60]. LTCC materials are developed specifically for their ability to be cofired with low resistivity metal electrode materials, such as gold and silver, therefore LTCC sintering temperatures must be lower than the melting temperature of these metals. In addition, the LTCC and electrode materials must be nonreactive and exhibit similar sintering behavior to prevent defects caused by differential shrinkage during the sintering possess. Full densification of LTCC is also essential to achieve required mechanical

properties and avoid penetration of the electrode into the defects. The other requirements for LTCC substrates are low dielectric constant and dielectric loss.

The prospective research goal is to design and develop biocompatible LTCC by starting with well-known biocompatible raw materials. The developed materials are targeted for use in microfluidic chips as in vitro/in vivo devices for real time monitoring, portable diagnostics and bedside analysis. In this paper, a new LTCC system has been reported through sintering a low-melting glass and alumina ceramic. The microstructure, dielectric properties and compatibility with electrode metal are reported. In addition, cytotoxicity results from both indirect leaching and direct attachment cell culture studies with human umbilical vein endothelial cells (HUVECs) are evaluated to assess the biocompatibility of sintered LTCC substrates.

3.2 Tape casting technique

Tape casting is a low cost and simple forming technique for shaping thin, flat ceramic. This method is originally developed for electronic ceramic in industry, including insulating substrate materials for electronic circuits, multilayered ceramic packages and multilayer ceramic capacitors[150]. The multilayer package is to laminate several individual layers with metallization and via interconnections together, which can be co-fired into a monolithic structure. The advantages of multilayer technique involves the capability to fabricate electronic circuit with relative short length, which leads to high speed computer; excellent thermal dissipation and structural strength; the ability to operate at high temperature. Other kind of electronic ceramic materials which act as resistor, sensors,

electrooptics, or magnetics are also dependent on tape casting for forming thin and flat electronic components.

Tape casting has also been extensively used in construction of fuel cell components. The thin stabilized zirconia film which acts as the electrolyte in the solid state fuel cell is fabricated by tape casting[151]. All components in molten carbonate fuel cells including electrodes and electrolyte are manufactured by tape casting[152]. Tape casting has also been applied in fabricating and developing structural membranes and laminates. Shearing action under the doctor blade tends to orientate the grains in the slip, and highly ordered colloidal crystal membranes have been developed as a results of this process[153, 154]. Functional of gradient materials have been developed by lamination of materials with different compositions[152].

In tape casting, the slurry is spread over a surface covered with a removable sheet of paper or plastic using a carefully controlled blade referring to as doctor blade as shown in Figure 3.1. The dispersant is the very important organic addictive in that it serves to lower the viscosity of the slurry, and stabilize the slurry against flocculation by increasing the repulsion between the particles, thereby allowing the use of a high particle concentration. Another important selection is the binder-plasticizer combination. Binders are typically long chain polymers that serve the primary function of providing strength to the green body by forming bridges between the particles. However, the glass transition temperature T_g must be relatively low to aid the deformation of the binder during forming. A reduction in T_g involves essentially reducing the resistance to motion of the polymer chains. Plasticizer is generally organic substances with a lower molecular weight than the binder. The primary function of the plasticizer is to soften the binder in the dry

state, thereby increasing the flexibility of the green body. The binder-plasticizer must provide the required strength and flexibility of the green tape and must easily be burnt out prior to the sintering of the tape[155]. The process of tape casting is shown in Figure 3.2.

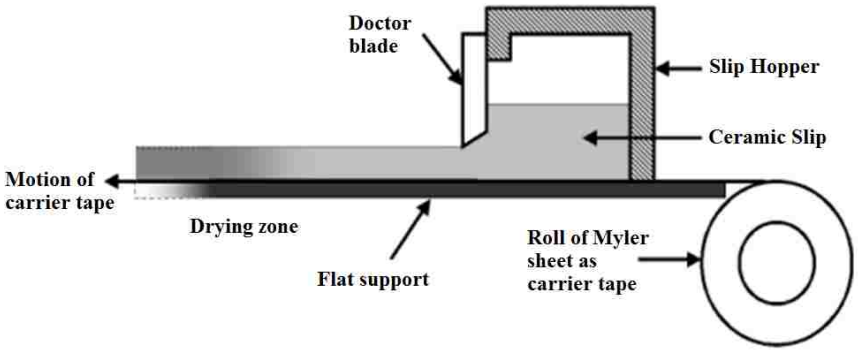

Figure 3.1: Tape casting process. Reprinted from the website[156]

Preparation of water based slurries is less expensive and toxic. But water elimination is big issue for the aqueous tape casting using water based slurries, so only very thin green tape layer is prepared. For water based binder, Latexes, polyvinyl alcohols (PVA), cellulose ethers such as hydroxyethyl cellulose (HEC), hydroxypropylmethyl cellulose (HPMC)[157-159] are frequently used. It is very difficult to prepare high concentration PVA and cellulose ethers in water with low viscosity. The solid loads after adding binder is always lower the 40 vol%. Latex is defined as a stable colloidal dispersion of a polymer substance in aqueous mediums. The volume fraction of polymer can reach from 40% to 70%. The polymer particle is always spherical with surfactant surrounding the polymer. The surfactant can be anionic, nonionic and cationic. For aqueous tape casting, the polymer are often acrylic and the common surfactant is anionic. The surfactant can stabilize the emulsion and reduce the foam formation. And the surfactant can strong absorbed to the ceramic surface and inactivated during the

whole process. However, the common way to perform tape-casting is to use slurries with organic based solvents, such as ethanol, methanol, toluene, xylene, methyl ethyl ketone. One of the considerations in the selection of organic solvent is due to capability of highly volatilization, so less solid loading are requirement to prevent cracks. In order to dissolve the wide variety of the addictive in the slip, including dispersant, binder and plasticizer, it is common to use more than one solvent. Menhaden fish oil is one of the most common dispersants in organic solvent based tape casting, and it contains more than twenty different kinds of fatty acids. Fish oil primarily act as a kind of steric deflocculants. Oxidized brown menhaden fish oil develops active polar ester group, and it is a rather good deflocculant for oxide systems[152]. Majority of the binders fall into two main: polyvinyl and polyacrylate. Polyvinyl alcohol is typically used as binder in aqueous tape casting. Po1yvinyl butyral (PVB) as polyvinyl resin is commonly used in the organic solvent cast casting.

The thickness of green tape has been theoretically analyzed. It is assumed that the slurry is Newtonian viscous and only laminar flow occurs during the tape casting. The thickness of dry tape, h_d, is determined by[77, 160]:

$$h_d = \frac{\alpha}{2}\frac{\rho_w}{\rho_d} h_0 \left(1 + \frac{h_0^2 \Delta p}{6\eta U L}\right) \tag{3.1}$$

where α (< 1) is correction factors, ρ_w and ρ_d are the densities of the slurry and the dry tape, h_0 and L are the height and length of the doctor blade respectively, η is the viscosity of the slurry, U is the velocity, Δp is the pressure difference determined by the height of the slurry in the reservoir. According to the equation, the thickness of the dry tape is

proportional to the height of the doctor blade if the second term, $h_0^2 \Delta p / 6\eta UL$, is much less than 1.

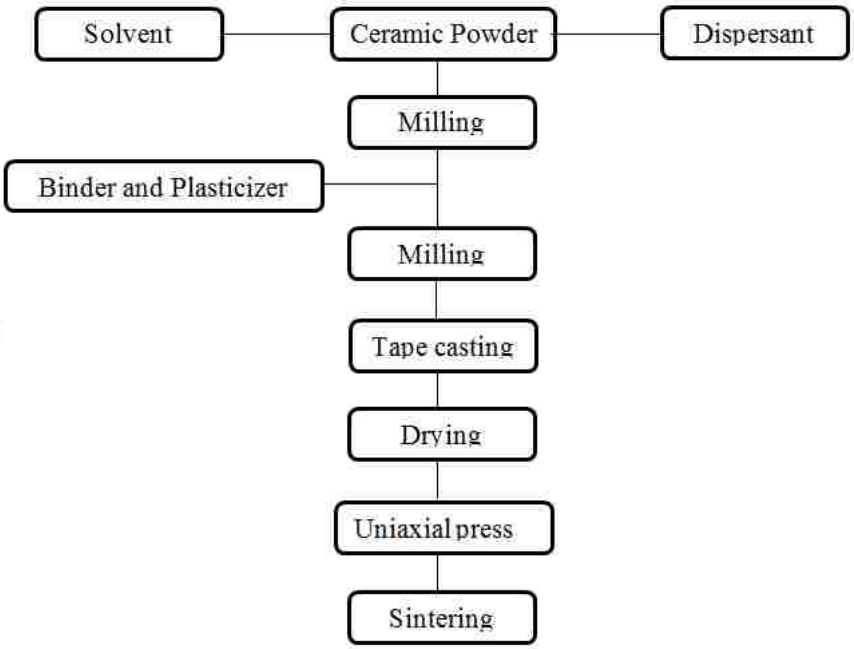

Figure 3.2: Flow diagram of tape casting.

3.3 Biocompatibility of the materials

Biomaterials are defined as "a nonviable material used in a medical device, intended to interact with biological systems"[161]. Many synthetic materials have been applied in medical applications such as prostheses, implants[162] and tissue engineering matrices[163]. One big problem is the foreign-body reaction when a synthetic biomaterial implanted into human body. All kinds of protein absorbed to the surface when the synthetic materials contact with the physiological environment. Then cells attack the materials, and form giant cells, and finally dense vascular collagen capsule is formed to

exclude the foreign materials, which may further cause infections, local tissue waste, implant encapsulation, thrombosis and embolization[164]. Biocompatibility has been defined as "the ability of a material to perform with an appropriate host response in a specific application"[165]. The concept of biocompatibility can be divided into two principles: biosafety and biofunctionality. Biosafety are related with adverse effects, such as carcinogenic effects, when cells contact with the materials or the release of the materials contents[166]. Biofunctionality is concerned with the performance of a given materials contacted with a particular tissue.

Cytotoxicity of materials is to evaluate the toxicity of the materials. Cytotoxicity evaluation can be performed by using direct contact with a layer of cells. In addition to the direct test, another widely used in vitro cytotoxicity testing method is the extraction test. The test material is extracted with a liquid, which can be cell culture medium, saline solution, vegetable oil, or another solvent that are relevant to the application of the test materials. The biofunctionality can be evaluated by criteria such as cell adhesion, cell spreading, cell proliferation, etc.

3.4 Experimental Procedure

3.4.1 LTCC fabrication and sintering

A soda-lime silicate glass frit (Schott B 270 Superwite, MO-SCI, Rolla, MO) with major components CaO, Na_2O, K_2O, Al_2O_3, and SiO_2 was used in this experiment. The glass frit has a glass transition temperature (T_g) 533^{O}C, softening temperature 724^{O}C, and density 2.55 g/cm^3. The mean particle size and Brunauer–Emmett–Teller (BET) specific surface area of the glass are 320 nm and 11.68 m^2/g respectively. The ceramic filler is

alpha alumina (HP-DBM, Baikowski Malakoff, Inc., Malakoff, TX) with particle size 300 nm, and BET specific surface area 6.99 m^2/g.

The slip formulation for tape casting consisted of a glass and alumina mixture in a ratio of 46:54 wt%. This mixture was first ball milled with zirconia media for 24 hr in a xylene/ethyl alcohol solvent with menhaden fish oil dispersant. Then a binder (polyvinyl butyral) and plasticizers (polyalkalene glycol and butyl benzyl phthalate) dissolved in solvent were added for another 24 hr ball-milling. The total solid loading of the slurry was about 45 wt%.

The slip was tape cast onto a silicone-coated Mylar film (R.E Mistler, Yardley, PA) using a bench-top caster with a single doctor blade (TTC-1200; R.E. Mistler, Yardley, PA). The thickness of the resulting green tape was about 110±15 μm. Several layers of green tape were aligned and laminated together at 6.9 MPa at $70^{O}C$ for 20 min using a uniaxial press (3851, Carver, Wabash, IN). Then the green tape was cut into square size using a CO_2-laser milling system (VLS 3.50, Universal Laser Systems, Scottsdale, AZ). The green tapes were first burnt out through 1 ^{O}C/min heating up to $450^{O}C$ with a 1 hr dwell time then sintered at different temperatures with 5 ^{O}C/min heating rate. Thermogravimetry (TGA) and differential scanning calorimetry (DSC) of the green tape was measured using a Netzsch STA 449C. Phase evolution of the sintered ceramic was analyzed using X-ray diffraction (XRD, Model-D500, Siemens, Munich, Germany). The shrinkage of the green tape as a function of sintering temperature was analyzed by measuring the dimensional change in the x and y directions. The stability of green tape with gold was also tested by co-firing the green tape with screen printed gold pattern with line width 0.5 mm and length 12 mm, using TC8101 paste (Heraeus, Thick Film

Division, West Conshohocken, PA). Ten layers of green tape with width 8.5 mm and length 10.9 mm were laminated together and total thickness of the lamination was 1.06 mm. The microstructure was analyzed using a scanning electron microscope (SEM, S-4300, Hitachi, Tokyo, Japan). For measuring the dielectric characteristics, one surface of the sintered LTCC with thickness 0.5 mm was printed with conductive Ag electrode paste (DuPont 6160, Research Triangle Park, NC) and the opposite surface was printed with a circle with diameter 7.8 mm. Then it was post fired at 850^{O}C for 10 min. The dielectric properties were obtained by measuring the capacitance and loss at room temperature using a precision LCR meter (Agilent E4980A, Agilent, Santa Clara, CA).

3.4.2 Biocompatibility

HUVECs were used to evaluate cytotoxicity. HUVECs were cultured in culture flasks with endothelial growth medium-2 (EGM-2) (Lonza, Allendale, NJ) and maintained in incubator with 5 % CO_2 at 37^{O}C. Figure 3.3 shows the experimental procedure.

For the leaching study, the LTCC were sintered at 900^{O}C for 2h. The LTCC coupons were sterilized by sonicating in DI water for 5 min, isopropanol (IPA) for 5 min, and autoclaving at 121^{O}C for 30 min. Then the LTCC leachate medium was obtained by soaking the LTCC in 1 ml of EGM-2 per square centimeter of LTCC surface area (1 mL/cm^2 EGM-2) in a cell culture incubator at 37 ^{O}C for 7 days. The resulting medium (LTCC Leachate) was pipetted off and stored for later use.

For the adhesion study three LTCC discs were sintered at 900^{O}C for 2h, followed by soaking in Dulbecco's phosphate-buffered saline (DPBS) for 1 day to eliminate any

easily leachable components. The DPBS used in the experiment was generated by adding 4 g NaCl, 0.5 g Na_2HPO_4, 0.1 KCl and 0.1 g KH_2PO_4 to 500 ml de-ionized water. The discs were then sterilized by sonicating in water for 5 min, IPA for 5mins, and autoclaving at $121^{O}C$ for 30 min. Finally the LTCC discs were dried, sprayed with ethanol, and placed under the hood in UV light for 1 hr. Then the ceramics were placed into three wells in a twelve well cell culture plate, and 0.5 mL 25 μg/mL of fibronectin solution (Invitrogen, Carlsbad, CA) was added and placed in an incubator for 2 hr to allow the fibronectin adsorb to the LTCC surface. After 2 hr the fibronectin solution was removed by pipetting and the LTCC discs were rinsed with 1mL DPBS three times.

For the final study, HUVEC cells were seeded into nine standard polystyrene cell culture wells at concentration of 25,000 cells/cm^2. Fresh medium was used for three wells as "controls" and for three wells containing the fibronectin coated LTCC discs. The LTCC leachate medium was used to culture the cells in the remaining three well. The medium was changed after one day incubation. For leachate study, the leachate medium was used to change the medium. After two days incubation, Calcein-AM (Invitrogen, Carlsbad, CA), a green-fluorescent LIVE cell stain; and Ethidium homodimer I (EthD-I) (Invitrogen, Carlsbad, CA), a red-fluorescent nucleic acid or DEAD stain, were used to stain the live and dead cells respectively. Digital images were taken using fluorescence microscope with the appropriate fluorescent filter cubes. The number of number of LIVE cells, DEAD cells and total cell number were counted using automated image analysis software.

To determine if there was a significant difference between cytocompatibility data, results were analyzed using Student's T-test. Results were reported to be significant when the P-value was equal to or lower than 0.05.

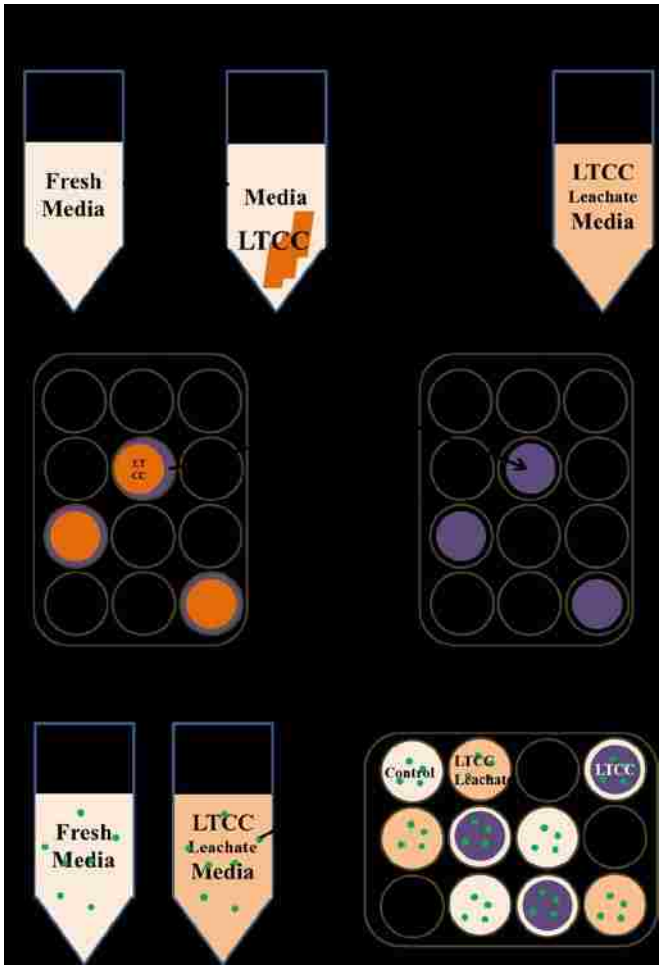

Figure 3.3: Experimental procedure for biocompatibility testing

3.5 Results and discussion

3.5.1 LTCC fabrication and sintering

A preliminary sintering study using dry pressed pellets was performed to identify the appropriate amount of glass frit addition required to reduce the sintering temperature

into the range compatible with LTCC materials and processing. On the basis of these results a composition with 46% by weight of glass frit in alumina was selected for the preparation of LTCC tapes. Figure 3.4 presents the TGA and DSC curves of the prepared green tape. There was a large initial burnout of organic additives from 200^{O}C to 320^{O}C, followed by a slow burnout process up to 460^{O}C. The burnout process was completed by 460^{O}C with total weight loss 25 wt%. At temperatures lower than 600^{O}C, the exothermic peaks were attributed to organic additive burnout. Only one crystallization peak was observed with the onset point of crystallization (T_c) at 940^{O}C. The sintering profile was created based on the TGA results. A slow heating rate of 1^{O}C/min up to 450^{O}C with a 1 hr dwell time was applied to ensure complete burn out the organic additives. A heating rate of 5^{O}C/min was employed up to the final sintering temperature with a 2 h dwell time at the sintering temperature.

The density and linear shrinkage without metallization of the LTCC tapes sintered at different temperatures is shown in Figure 3.5. The density of the LTCC initially increases with sintering temperature, and the density is found to be higher than 95% theoretical density for sintering temperatures from 850^{O}C to 950^{O}C. The density then decreases with further increase in sintering temperature. The shrinkage of the green tape stays in the range of 20% at sintering temperatures higher than 800^{O}C. Open porosity measured by the water immersion' method was also substantially decreased with values less than 0.2% at sintering temperatures higher than 800^{O}C. The highest density was achieved at a sintering temperature of 900^{O}C. These results confirm high density ceramic with 46 wt% glass and 54 wt% Al_2O_3 formulation can be obtained with sintering temperature lower than 950^{O}C.

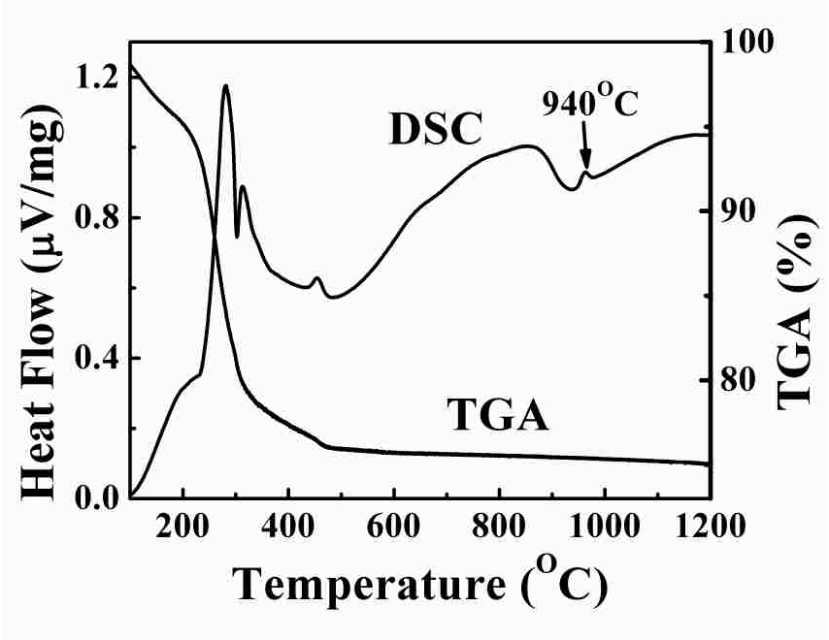

Figure 3.4: DSC and TGA of the green tape with 46 wt% glass at heating rate of 5 ^{O}C/min.

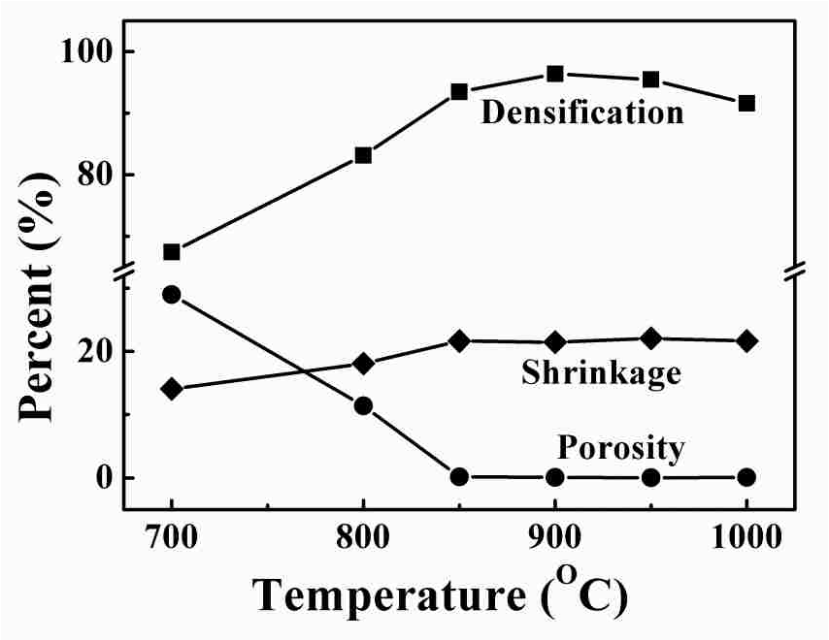

Figure 3.5: Densification, open porosity and shrinkage in the x and y directions of the green tape at different sintering temperature.

XRD patterns of the glass frit and the LTCC sintered at different temperatures are shown in Figure 3.6. No crystalline peaks were observed in the XRD pattern of the raw glass frit, indicating complete vitrification and no recrystallization of the glass phase. In the tapes sintered at 850^{O}C, all observed peaks can be indexed as alumina. In addition an amorphous hump was observed in the region 20 to 35^{O} two theta. As the sintering temperature increased to 900^{O}C, a second crystalline phase nucleated (identified as anorthite $CaAl_2Si_2O_8$, PDF No: 41-1486) and the area of the amorphous peak was also decreased. This is consistent with the reaction of the glass phase with alumina resulting in second phase formation. The crystallization behavior in XRD results was also consistent with the DSC curve, and the exothermic peak at 940 ^{O}C in the DSC result was subsequently attributed to anorthite crystallization.

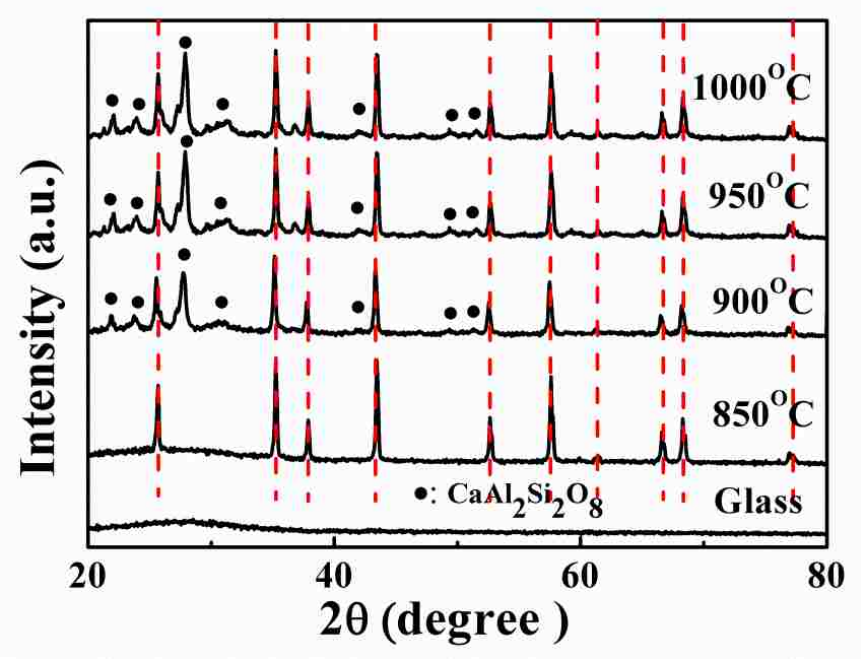

Figure 3.6: XRD of the LTCC sintered at different temperature.

A dense glass ceramic microstructure was observed in SEM images of the fracture surface of the LTCC sintered at 900 ^{O}C, as shown in Figure 3.7. The glass formed an interconnected matrix phase, almost completely encapsulating the alumina particles. For sintering temperatures greater than or equal to 900 ^{O}C, isolated spherical pores were observed in lower magnification micrographs. The size of the pores was less than 5 μm. These pores were attributed to glass bloating due to over sintering, and were not observed for sintering temperatures less than 900 ^{O}C. This is consistent with the gradual decrease in density observed for tapes sintered above 900^{o}C.

Many common LTCC formulations are composed of a mixture of a high temperature ceramic filler and a low-melting temperature glass. In these cases the sintering of the LTCC occurs primarily by viscous flow due to the large volume of glass utilized in such formulations.

Ewsuk and colleagues proposed a non-reactive liquid phase sintering model, in which the densification follows a three stage sintering process, including glass redistribution, grain rearrangement, and viscous flow[74, 75]. Good wetting behavior between the glass and ceramic phases play an important role in the first and second stage. Poor densification or swelling would occur due to poor wetting between the glass and ceramic phases. Elimination of the residual pores (~10%) occurs in the final stage. Densification in the final stage is independent of the wetting behavior, occurring by viscous flow. The ceramic filler increases the relative viscosity of the glass-ceramic composite. Glass with low viscosity is required to fill the closed pores for LTCC with high ceramic filler concentration. Low ceramic filler concentration is required to eliminate closed pores for glass with high viscosity[73-75]. The glass chosen in this

experiment has the alkali oxides, Na_2O and K_2O present as the network modifiers. The alkali oxides reduce viscosity of the glass, and the volume percent of ceramic filler in this experiment can reach as high as 44 %.

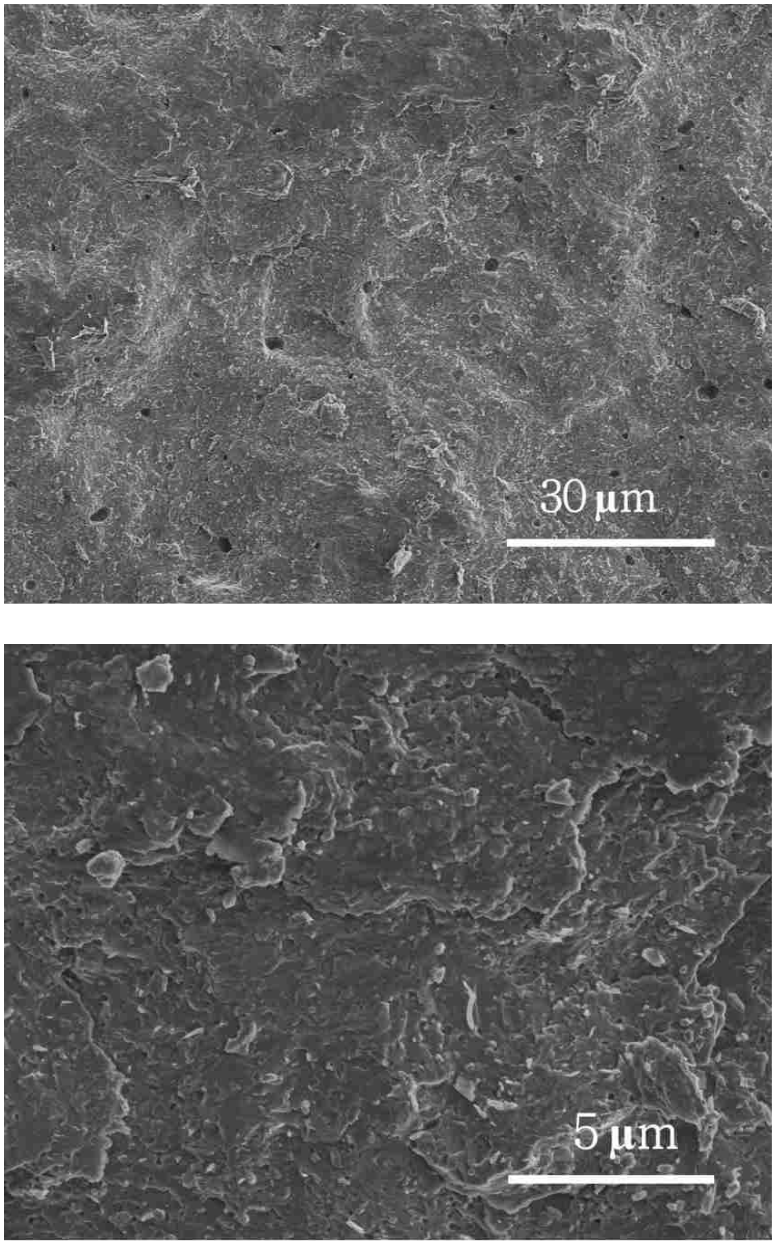

Figure 3.7: SEM of the LTCC fracture surface

The low sintering temperature of LTCC is intended so as to allow cofiring of high conductivity, low melting temperature metal electrodes, including Au, Ag and Cu. In this experiment commercial gold ink paste (TC8101, Heraeus, Thick Film Division, West Conshohocken, PA) was co-fired with the LTCC at 900^{O}C. Figure 3.8 shows the resulting interface between the electrode gold and the LTCC. There was a clear interface between the LTCC and gold, which confirms the gold was stable and no reaction occurred when co-fired with the LTCC. In addition no cracking, camber or delamination was observed.

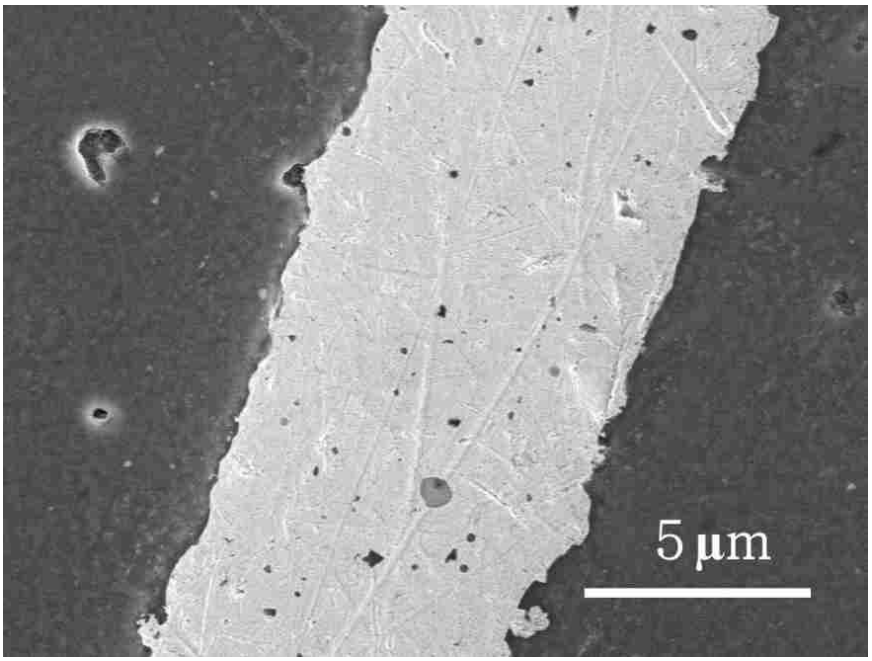

Figure 3.8: SEM of the interface between gold electrode and LTCC sintered at 900 ^{O}C.

The dielectric constant of LTCC sintered at 900^{O}C was stable with value ~ 9.3 and at frequency from 1 kHz to 2 MHz as shown in Figure 3.9. The dielectric loss decreased with increasing frequency, with value less than 0.5% in the frequency range from 1 kHz to 2 MHz. The dependency of dielectric loss on the frequency may be due to hopping

conductivity of alkali ions in the glass phase[167]. The anorthite phase has a low dielectric constant ~5, and the formation of anorthite from the glass reduces the amount of alkaline earth, and it is an advantage for LTCC microelectronic application[168]. The dielectric properties are comparable to the reported typical values specified for the low dielectric constant LTCC formulations[169].

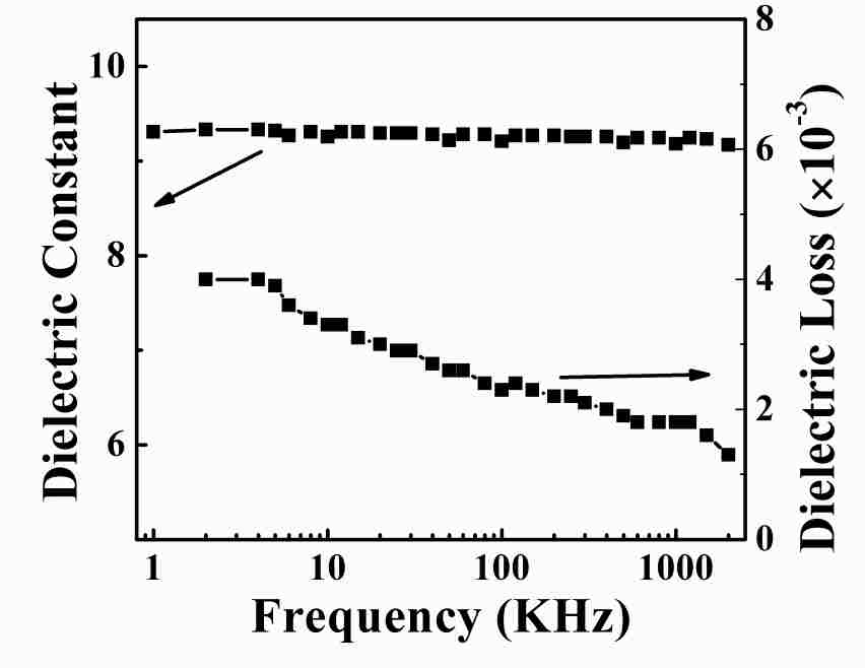

Figure 3.9: Dielectric properties of the LTCC sintered at 900 ^{O}C.

3.5.2 Biocompatibility

In this work, two different methods were used to evaluate the biocompatibility for the intended application. The first method is indirect cytocompatibility assessed by exposing HUVECs to leachate obtained by soaking the LTCC substrates in cell culture medium. In the second experiment cells were directly seeded and cultured on fibronectin coated LTCC coupons.

Figure 3.10 shows example images obtained from a LIVE/DEAD assay conducted after 48 hours, in which live cells appear green and dead cells appear red. The resulting images correspond to HUVECs seeded on standard tissue culture coated cell culture wells (Control), cells grown on fibronectin coated LTCC substrates (LTCC), and cells cultured on tissue coated wells using LTCC leachate medium (Leachate). Table I summarizes quantitative image analysis the LIVE/DEAD assay.

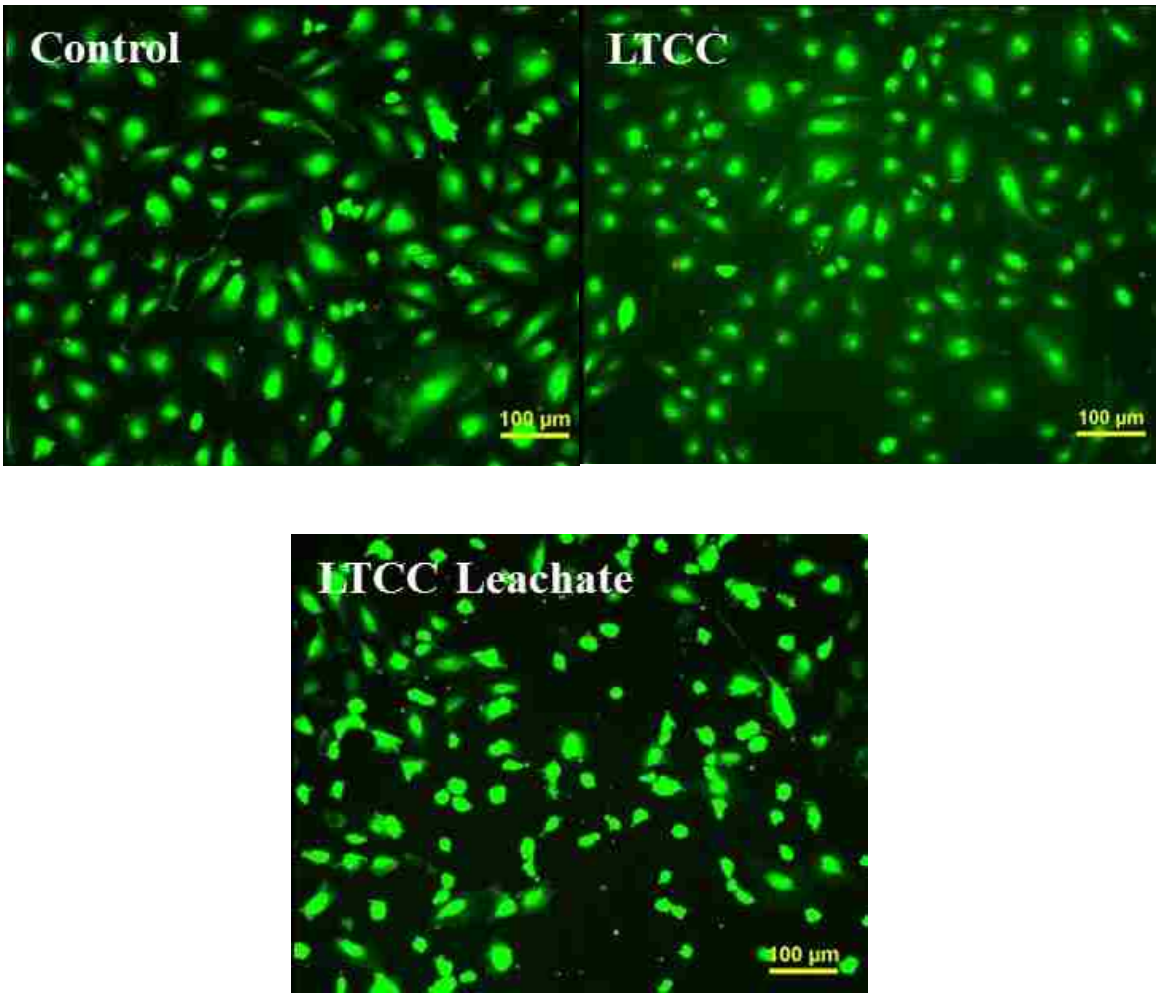

Figure 3.10: Pictures of the cultured cells using fresh medium (control), leachate medium (LTCC leachate) and on fibronectin coated LTCC substrate (LTCC).

Figure 3.11 shows telative cell density of LTCC and LTCC leachate compared with that of control. The cells attached and spread in the LTCC leachate and on the fibbronectin coated LTCC surface as shown in Figure 3.10. Some of the cells in the three groups have cobblestone-like morphology. The cells were not fixed in this experiment, and the morphology of some cells changed to a spherical shape during the staining and imaging process. Other than that, no abnormal morphology was observed.

The percent of live cells in the control, the LTCC surface and LTCC leachate medium were all higher than 99%. The cell density observed in the LTCC leachate solution and on the LTCC surface was a little lower than that of the control, 80%±6% and 87%±7% of the value in control respectively. However, no significant differences ($p > 0.05$) were observed among the control, the LTCC leachate medium and fibronectin coated LTCC. On this basis it has been established that no significant cytotoxicity of the LTCC was observed in this experiment.

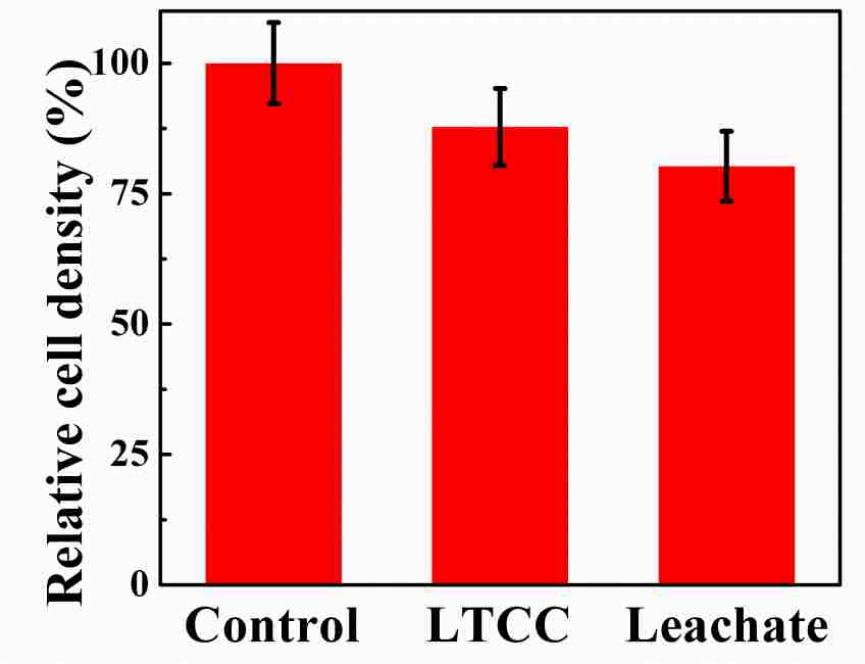

Figure 3. 11: Relative cell density of LTCC and LTCC leachate compared with control.

Table 3-1: Live cell percent and cell concentration of the cultured cells using fresh medium (control), leachate medium (LTCC Leachate) and on fibronectin coated LTCC substrate (LTCC).

	Control	**LTCC**	**LTCC leachate**
Live cells	99.8±0.1%	99.5±0.1%	99.5±0.1%
Cell density (Cells/cm^2)	32000±2500	28000±2400	26000±2100
Relative cell density	100±7%	87±7%	80±6%

Commercial LTCC substrate, such as DP 951 (DuPont), has been reported to exhibit congenial surface for mammalian cell culture growth[71, 170], however, DP 951 has also been reported to contains lead[171]. The advantage of this LTCC is free of lead, cadmium, cobalt and nickel to reduce the potential toxicity to living cells and meet

environmental registration[36, 38]. The biocompatibility study of this LTCC with HUVECs indicates developed LTCC also provide hospitable surface for living cells.

3.6 Conclusion

The current work describes the preparation and evaluation of a biocompatible LTCC. The best formulation of glass and ceramic for tape casting was found to contain 46 wt% glass and 54 wt% ceramic. The density of the developed LTCC initially increases with sintering temperature, and then decreases at higher temperature. The density of LTCC sintered at temperature from 850^{O}C to 950^{O}C is higher than 95% of theoretical density. The co-firing results of the LTCC and gold electrode indicates the ceramic layer is compatible with the gold electrode layer. The material also exhibits dielectric properties typical of a low dielectric constant LTCC material. HUVECs were observed to readily attach and spread on the surface of fibronectin coated LTCC and in the LTCC leachate, and the cell density and percentage of live cells on fibronectin coated LTCC substrate and LTCC leachate are comparative with those of control. There is no significant difference among the control, LTCC leachate and fibronectin coated LTCC. The results confirm that the developed material is biocompatible and will provide a suitable LTCC substrate for microfluidic and lab-on-chip applications utilizing live cell sensing.

Chapter 4 Sintering behavior and biocompatibility of a low temperature co-fired ceramic for microfluidic biosensors

4.1 Introduction:

The prospective goal of the current study is to design and fabricate biocompatible LTCC, using well-known biocompatible raw materials as a starting point. The potential application for this material is in the rapid prototyping and custom manufacture of cell based microfluidic sensors for both scientific research and clinical portable diagnostic applications. Borosilicate glass has been reported to exhibit biocompatibility for joint and cortical implantation and has also been most extensively used as cell culture coverglass, plate, dishes and tubing[172, 173]. Alumina is highly mechanical and chemical stable, nontoxic and biocompatible[174, 175]. Based on these considerations, borosilicate glass and alumina ceramic were chosen as raw materials with composition based on the report by Muller. R.[176]. In this paper, the densification behaviors and sintering properties were analyzed using MSC theory. The microstructure, dielectric properties and compatibility with electrode Ag and Au were also investigated. In addition, the biocompatibility of the sintered LTCC was examined through the human umbilical vein endothelial cell (HUVECs) proliferation in LTCC leachate medium and on cell culture coated LTCC substrates.

Microfluidic devices provide powerful tools for biological analysis and biomedical research such as clinical diagnostics, toxicity monitoring, DNA, cellular and protein analysis because of small volume of sample and reagent utilized in these devices. They have been considered as promising candidates for portable point-of-care medical diagnostic systems in global public health[177, 178]. Glass, silicon, polymers and ceramic have been extensively used to develop microfluidic devices. However, the selections of substrate materials have profound effects on the design and functionality of the microfluidic devices. The cytocompatibility, immunogenicity, biodegradability and wetting properties, in particular for biological samples such as cells, are important[179]. Low temperature co-fired ceramics (LTCCs) have emerged as potential alternative materials for development of microfluidic devices. The advantages of the LTCC include chemical inertness, high temperature stability, high mechanical strength and easy fabrication of systems with microfluidic functional components[46]. Microfluidic devices developed using LTCC technology have been successfully applied in biosensing, environmental sensing, and point-of-care diagnostic systems[26, 27, 33, 34, 180]. However, commercially available LTCCs are optimized for microelectronic applications and the biocompatibility of these materials generally unknown[68]. The biostability and leaching behavior of commercial LTCC materials in biological fluids can also vary drastically[37, 149]. It is very difficult to understand and modify the biocompatibility of commercial LTCCs because of their use of complex and generally proprietary formulations. For these reasons, a custom LTCC formulation has been fabricated specifically considering biocompatibility.

Biocompatibility is “the ability of a material to perform with an appropriate host response in a specific situation[181].” This definition advances the understanding that “biocompatibility” is not a universal set of characteristics and that biomaterials must be considered and designed as an active and integral component of each specific biological system. For implantable devices, biocompatibility includes features such as the immune and inflammatory response. For cell based biosensors used outside human body, biocompatibility comprises the feasibility of sustaining cell cultures on the material surface, and the absorption of the intended analyte such as antigen or bioreceptor such as DNA and antibodies on the devices surface[180]. The developed LTCC substrate in this work is targeted for biosensor incorporating live endothelial or other adherent human cell based biosensing applications. In this context, biocompatibility of developed LTCC is that the LTCC surface supports the attachment and proliferation of the targeted cell line without toxicity effects from the leachate elements.

LTCCs are generally glass-ceramic composites and several methods to develop and formulate LTCC systems have been reported in the literature including recrystallizable glasses,[56, 58] mixtures of low melting temperature glass and ceramic[57, 60, 167]. Perhaps the most common is the second which combines a low melting temperature glass and with a high temperature ceramic filler. In this approach low temperature glass frits function as a flux, which serves to reduce the sintering temperature of the ceramic filler. In addition to the glass frit, the advantages of this second method are the capability to control the sintering temperature, and modify electrical and mechanical properties by adjusting the ratio of glass phase and ceramic. This is the approach taken in the current work.

The master sintering curve (MSC) concept proposed by Su and Johnson has been used to predict and optimize the densification behavior quantitatively in practical sintering processes[182]. The MSC curve and the activation energy for sintering can be estimated empirically using sintering data obtained through either isothermal sintering at different temperature or constant heating rate sintering at different heating rate. Once the MSC curve is constructed, and it can be further applied to predict the densification behavior for any combination of sintering time and temperature. It also allows identification of the dominant densification mechanism[183]. The MSC was originally developed to analyze the solid-state sintering with isotropic sintering behavior, and it has been further extended to study the anisotropic sintering behavior by liquid-phase sintering and viscous flow sintering[184-187]. LTCC contains high volume of glass phase, and sintered by viscous flow[73]. The accurate prediction of LTCC densification behavior using the MSC can enable process optimization and reproducibility.

Co-firing ceramic with high-electrical-conductivity metals, such as gold and silver, is one of the most important steps in the development of low temperature ceramic packages. The LTCC materials and electrode are required to be nonreactive. For example, lime borosilicate glass has been reported nonreactive with electrode and has been extensively used in fabrication of LTCC[176, 188, 189]. The sintering temperature of LTCC should also match that of electrode. Low sintering temperature may cause incomplete densification of the electrode. High sintering temperature may induce metal diffusion and migration at the interface leading to current leakage and dielectric breakdown[190]. In addition, mismatch between the sintering behaviors of LTCC and electrode could cause undesirable co-firing defects including delamination, cracking and camber[191-193].

Therefore, the co-firing and microstructure of the internal metal electrode and ceramics should be carefully controlled for reliable performance in LTCC devices. The other requirements for LTCC substrate are low dielectric constant and dielectric loss.

4.2 Master sintering curve

Sintering is considered as a complicated process. It is very difficult to interpret the sintering behavior quantitatively because the sintering always involves microstructure evolution due to several different diffusion mechanisms. Early studies define the sintering process into three stages and use well defined geometric models to analyze only one of the three stages[194, 195]. Only in special cases, the geometric approximation results are consistent with the experiments[196]. There is a considerable interest to generate a model to predict the densification during the entire sintering process. The master sintering curve (MSC) proposed by Su and Johnson is a new approach to quantitatively predict the sintering process of practical powder[182, 197].

The formulation and construction of MSC model is derived from combined stage sintering model[182, 198]:

$$-\frac{dL}{Ldt}=\frac{d\rho}{3\rho dt}=\frac{\gamma\Omega}{kT}\left(\frac{\Gamma_v D_v}{G^3}+\frac{\delta\Gamma_b D_b}{G^4}\right) \tag{4.1}$$

where L is the sample dimension, t is sintering time, ρ is the relative density, γ is the specific surface energy, Ω is the atomic volume, k is the Boltzmann constant, T is the absolute temperature, G is the average grain diameter, δ is the width of the grain boundary, D_v and D_b are the coefficient of volume diffusion (subscript v) and grain

boundary diffusion (subscript b), Γ is the individual component of the lumped scaling parameter, which is related with the driving force, mean diffusion distance, and other geometry features of the microstructures, such as mean grain size.

If G and Γ are only functions of density and only one diffusion mechanism dominates during the sintering, the equation can be simplified, rearranged and integrated as follows:

$$\int_{\rho_0}^{\rho} \frac{(G(\rho))^n}{3\rho\Gamma(\rho)}\, d\rho = \int_0^r \frac{\gamma\Omega D_0}{kT(t)} exp\left(-\frac{Q}{RT(t)}\right) dt \tag{4.2}$$

where ρ_0 is the green density of the powder composite, Q is the apparent activation energy for sintering, $D_0 = (D_v)_0$ and $n = 3$ when volume diffusion dominates, $D_0 = (D_b)_0$ and $n = 4$ when grain boundary diffusion dominates during the sintering. The left side of this equation is only related with density, and the right side is related with the temperature-time trajectory. Further rearrangement of the equation makes the equation became:

$$\Phi(\rho) \equiv (\frac{k}{\gamma\Omega D_0} \int_{\rho_0}^{\rho} \frac{\big(G(\rho)\big)^n}{3\rho\Gamma(\rho)}\, d\rho \tag{4.3}$$

and

$$\Theta(t, T(t)) \equiv \int_0^r \frac{1}{T(t)} exp\left(-\frac{Q}{RT(t)}\right) dt \tag{4.4}$$

where

$$\Phi(\rho) = \Theta(t, T(t)) \tag{4.5}$$

The relationship between ρ and $\Phi(\rho)$ is defined by master sintering curve (MSC). The MSC is unique for a given powder and green-body process independent of sintering path. A simple way to construct the MSC is to use the equation. The integration of equation (4.4) can be calculated for any arbitrary sintering path as long as Q is known or estimated. Otherwise a series of experiment with different sintering time and/or temperature is needed to construct a MSC.

Several assumptions are made to generate this model. First of all, MSC model is only applied to the same green power, green-body process and green density. Different powder results in difference in particle size, particle size distribution. Green-body process causes difference in pore-size distribution and packing properties and green density. Those quantities will affect densification process. Secondly, MSC model also assumes the microstructure evolution, both particle size and geometry, is only dependent on the density independent of the sintering temperature and heating rate. Another assumption is that only one diffusion mechanism, either volume or grain boundary diffusion, dominates during the sintering process. Surface diffusion and vapor transport causes coarsening without increase of the density, and they also retard the densification. The MSC may be not applied in these cases when surface diffusion and vapor transport dominate. However, the surface diffusion typically dominates at the beginning of sintering at low temperature, and it is insignificant compared with grain boundary diffusion over wide sintering temperature. Vapor transport dominates at high temperature approaching melting point, which is not expected at sintering temperature in most cases. This assumption to construct MSC model can be generally satisfied[197].

Su and Johnson originally use polynomial function to fit the data point of ρ and $\Phi(\rho)$. The best estimate of Q is found when the mean of the residual squares of the data points with respect to the fitted line is minimum[182]. The mean residual square (MSS) is given by:

$$MSS = \frac{1}{n}\sum_{i-1}^{n}(\rho_i - \rho)^2 \tag{4.6}$$

where ρ_i is the experimentally measured relative density, and ρ is the predicted relative density, n is the number of data points.

A sigmoid function also provides a good fit between ρ and $\Phi(\rho)$ [183, 199]:

$$\rho = \rho_0 + \frac{1-\rho_0}{1+\exp(-\frac{(ln\Theta - a)}{b})} \tag{4.7}$$

where ρ_0 is the green density of powder composite at the start of sintering, a and b are constant defining the curve.

A different sigmoid function has also been used to define the MSC[200]:

$$\rho = \rho_0 + \frac{a}{\left[1+\exp(-\frac{(ln\Theta - ln\Theta_0)}{b})\right]^c} \tag{4.8}$$

where ρ_0 is the green density of powder composite at the start of sintering, a, b and c are constant, $ln\Theta_0$ is the abscissa coordinate of the reflection point of the curve.

The MSC has also been modified to analyze the grain growth by Ostwald ripening with time and temperature in Park et al.'s work[201]. Two assumptions are made to modify

the MSC. First, microstructure evolution, both grain size and geometry, is only dependent on the density. Secondly, the apparent activation energy, Q, is a constant during the sintering. Then the equation of grain growth is transformed into the MSC form given by:

$$G = \sqrt[3]{G_0^3 + 3\Theta} \tag{4.9}$$

$$\Theta = \int_0^t \frac{kD_0 C\Omega\gamma}{RT(t)} \mathrm{f}(\mathrm{V}_l)\exp(-\frac{Q}{RT(t)})dt \tag{4.10}$$

where G_0 is the initial grain size, G is the mean grain size, D_0 is the pre-exponential factor of the diffusivity of the grain atoms in the matrix, $\mathrm{f}(\mathrm{V}_l)$ is a function of the liquid volume fraction V_l, k is a constant, t is the sintering time, C is the grain atoms' solubility in the matrix, R is the gas constant, and T is the absolute temperature. The grain size in the MSC curve is only dependent on the initial grain size, independent of the sintering cycle path. The experiment results also show that the grain sizes lie on a single curve regardless of sintering time and temperature.

The MSC is originally developed for powder composite systems that exhibit solid state sintering with isotropic sintering behavior [182]. The MSC concept has been further extended to analyze the liquid phase sintering and viscous sintering with anisotropic sintering behavior[183, 184, 187, 199, 202, 203]. The MSC has been used to predict and control the sintering in practical applications, and the predicted density by the MSC is consistent with the experimentally measured sintered densities[202], which verifies the validity of the MSC. Another powerful tool of MSC is to analyze the apparent activation energy for densification, Q[183, 204]. Comparisons of the apparent activation energy calculated by the

MSC with the reported in the literature for grain boundary or volume diffusion allows verification of dominated diffusion mechanism, and it also allows the detection of any change in the dominate diffusion mechanism. The MSC is also a powerful tool for quantifying sintering process which involves phase changes in multiphase sintering systems[183]. Grain boundary diffusion tends to dominate for powder with a small particle size, where volume diffusion tends to dominate for composites with a large particle size. Effects of the particle size on the diffusion mechanism can be observed readily by the MSC in practical sintering[204]. The MSC has also been applied to study the sintering kinetics of LTCC, although LTCC are glass based composite with high volume of glass phase and the sintering of LTCC occurs by viscous flow. The apparent activation energies obtained by MSC are consistent with the values achieved by master viscosity curve on isothermal data[184, 187], which indicates the validity of the MSC application to LTCC systems.

4.3 Experimental:

4.3.1 LTCC fabrication and sintering

A calcium alumina borosilicate glass frit with composition 38.3CaO-4.5Al_2O_3-49.8SiO_2-7.5B_2O_3 (mol%) was prepared by the rapid melt quenching method. A stoichiometric mixture of SiO_2 (Kentucky Mudworks, Lexington, KY), $Al(OH)_3$ (Kentucky Mudworks), $CaCO_3$ (Sigma-Aldrich, St. Louis, MO) and B_2O_3 (Acros Organics, Pittsburgh, PA) was mixed in an agate and melted in a covered alumina crucible at 1500^{O}C for 1 hr. The melt was subsequently quenched into cold de-ionized water in a steel pot. The glass powder was dried in an oven and grounded into fine

powder. The powder was vibratory milled in alcohol using magnesia-stabilized zirconia cylinders (US Stoneware, Mahwah, NJ) on a vibratory mill (ML16-5, Sweco, Florence, KY) for 36 hr. There was less than 1% weight loss of zirconia media observed after the milling step. The images of the glass powder was taken using scanning electron microscope (SEM, S-4300, Hitachi, Tokyo, Japan), and the particle size was analyzed to be around 2.9 μm using Image-Pro Plus 6.0 software. Brunauer–Emmett–Teller (BET) specific surface area, 2.1 m^2/g was determined by BET surface area analyzer. (TriStar 3000, Micromeritics, Gosford, NSW, AUS). The glass transition temperature, T_g=680^{O}C at heating rate of 5^{O}C/min, was evaluated using differential thermal analysis (DTA, STA 449C, Netzsch, Burlington, MA). The glass density, ρ=2.741 g/cm^3, was obtained by pycnometry (AccuPry^{TM} 1330, Micromeritics, Gosford, Australia). The ceramic filler was alpha alumina (LS-DBM, Baikowski Malakoff, Inc., Malakoff, TX)) with averaged particle size 1.3 μm, BET specific surface area 3.5 m^2/g.

The slurry formulation for tape casting contained 75 vol% glass and 25 vol% alumina, based on the formulation described in the report by Muller. R.[176] . Xylene and ethyl alcohol in 1:1 volume ratio was used as organic solvent. The mixture of glass and alumina were first ball milled with zirconia media for 24 hr in the solvent with menhaden fish oil dispersant (R.E. Mistler, Yardley, PA). Then a binder, polyvinyl butyral (R.E. Mistler), and plasticizers, polyalkalene glycol (R.E. Mistler) and butyl benzyl phthalate (R.E. Mistler), dissolved in solvent were added into the slurry for another 24 hr ball-milling. The total solid loading of the slurry was 58 wt%.

A bench-top tape caster with single doctor blade (TTC-1200; R.E. Mistler, Yardley, PA) was used to cast the slurry onto a silicone-coated Mylar film (R.E Mistler) at a speed

of 5.3 cm/min. The resulting green tape had a thickness of about 155±15 μm. Several layers of green tape were aligned and laminated together at 6.2 MPa at 70^{O}C for 20 min using a uniaxial press (3851; Carver, Wabash, IN). Then laminated green tape was vacuum sealed in a plastic bag, and 6.2 MPa isostatic pressure was applied at 70^{O}C for 15 min using a warm isostatic press (WIP 4.52230, Avure technologies, Inc.). The green tape was cut into squares for sintering experiments. The green tapes were first heated up to 450^{O}C at ramp rate of 1^{O}C/min with 1 h dwell time to completely burn out the organic additives, followed by sintering at different temperatures from 725^{O}C to 900^{O}C with 1, 3, 5 and 10 ^{O}C/min heating rate. Thermogravimetry (TGA) and differential thermal analysis (DTA) of the green tape was analyzed using Netzsch STA 449C instrument. The bulky density and open porosity was measured using Archimedes method. X-ray diffraction (XRD, Model-D500, Siemens, Munich, Germany) was carried out to analyze the phase evolution of the sintered ceramic.

4.3.2 Master Sintering Curve Analysis:

Four different heating rates (1^{O}C/min, 3^{O}C/min, 5^{O}C/min and 10^{O}C/min) were employed up to the sintering temperature and quenched into air for MSC study. The shrinkage of the green tape with sintering temperature was determined by measuring the dimensional change in x and y directions before and after sintering. A single theoretical density was calculated from the density and volume fraction of the glass and ceramic using mixing rule. The sintered density and theoretical density was used to calculate the relative density. Densification of the LTCC at heating rates of 1 ^{O}C/min, 3 ^{O}C/min, 5 ^{O}C/min and 10 ^{O}C/min are used for the construction of MSC curves.

4.3.3 Microstructure and Co-firing with electrode

The compatibility of the green tape with gold paste, TC8101 (Heraeus, Thick Film Division, West Conshohocken, PA), and silver paste, TC0307 (Heraeus, Thick Film Division, West Conshohocken, PA), was also tested by co-firing the green tape with screen printed electrode patterns. The width and length of electrode pattern line were 0.25 mm and 166 mm respectively, and two pads were at the end of the patterned line as contact leads for testing resistance. Ten layers of green tape were laminated together with width 21 mm, length 23 mm and thickness 1.45 mm. Two layers contain electrode patterns. One was on top of the lamination, and the other one was on the bottom of the lamination covered by one layer of green tape leaving two pads open for resistance testing. The laminate was co-fired at 825 ^{O}C for 30 min, and resistance was tested using a multimeter. The microstructure of the fracture surface was analyzed using SEM (S-4300, Hitachi, Tokyo, Japan). The microstructure of the polished surface was analyzed using both SEM and energy-dispersive X-ray spectrometry (EDS, S-3200, Hitachi, Tokyo, Japan). The sintered LTCC with painted conductive Ag electrode (DuPont 6160, Research Triangle Park, NC) was fired at 800^{O}C for 10 min for further measuring of the dielectric characteristics. The dielectric properties analysis was carried out by measuring the capacitance and loss at room temperature using precision LCR meter (Agilent E4980A, Agilent, Santa Clara, CA).

4.3.4 Biocompatibility: Cytotoxicity assay of LTCC leachate

Human umbilical vein endothelial cells (HUVEC) were used to evaluate cytotoxicity of LTCC leachate. For the LTCC leachate study, the sterilization procedure

for the LTCC consisted of sequentially sonication in de-ionized water for 5 min, complete drying in an oven, followed sonication in isopropanol for 5 min and autoclaving at 121^{O}C for 30 min. Finally the LTCC substrates were dried in an oven. After sterilization, and the LTCC was then sprayed with ethanol, placed under the hood in UV light for 1h. Finally the LTCC leachate medium was obtained by soaking the LTCC substrates in 1 ml endothelial growth medium-2 (EGM-2) (Lonza, Allendale, NJ) per square centimeter of LTCC surface area (1 mL/cm^2 EGM-2) in cell culture incubator at 37^{O}C for 5 days. EGM-2 medium was also incubated at the same time to monitor the change during the 5 days incubation, and it was called "blank" for short in the following paragraph. For control experiment, fresh medium without incubation was used. The HUVECs were seeded into 12-well tissue culture-treated polystyrene plate at concentration of 1.25×10^4 cells/cm^2 at passage 6. Three each wells were used for control, blank and LTCC leachate experiments respectively. After one day incubation a LIVE/DEAD assay (Invitrogen, Carlsbad, CA) was conducted to determine viability. Old medium was removed from the wells, and 1ml fresh medium with 0.2 (v/v%) Calcein AM for staining live cells and 0.3 (v/v%) Ethidium Homodimer-1 (EthD-1) for staining dead cells was simultaneously added into each well. After 20 min incubation, images were taken using fluorescence microscope (ECLIPSE LV100, Nikon). Live and dead cells were imaged in green color and red color respectively. The cell number in seven images with surface area 20 mm^3 and five images with surface area 5 mm^3 for each well was counted using software NIS-Elements DR 3.10. The viability of the cells was evaluated by cell density and live cell percent.

4.3.5 Biocompatibility: Endothelial cell adhesion and growth

LTCC substrates were sterilized as described above. Substrate surfaces were modified to promote cell adhesion by coating with fibronectin (a common mediator of cell adhesion). Substrates were randomly placed into three wells in of a 12-well tissue culture-treated polystyrene plate. Half a milliliter of a 25 μg/mL of fibronectin solution (Invitrogen) added to each well containing a substrate and allowed to soak for 2 hr in the incubator. The solution was removed and substrates were gently rinsed with 1mL Dulbecco's phosphate buffered saline solution (DPBS) three times, and the formulation of DPBS used in the experiment was 0.79% NaCl, 0.1% Na_2HPO_4, 0.02% KCl and 0.02% KH_2PO_4 in de-ionized water. HUVEC cells were seeded onto the fibronectin coated LTCC substrate at concentration of 1.25×10^4 cells/cm^2 at passage 6. For the control experiment, HUVECs were also cultured randomly in three additional wells in the same well plate. The cells were incubated for 14 hr for cell adhesion evaluation. The cell density was quantified by counting the cell number after staining the cells as described in above. To evaluate the cell proliferation, the culture medium was replaced every day, and the cells were incubated for 74 hr. The cells were imaged using fluorescence microscopy after the cells were stained, and the cell density was calculated by counting cell number.

Statistical significance was determined using ANOVA and Turkey test. A *p*-value equal to or less than 0.05 was considered to be significant.

4.4 Results and discussion:

4.4.1 LTCC fabrication and sintering

Thermal analysis (TGA/DTA of the prepared tapes was conducted to determine initial processing conditions for organic burnout and sintering, as shown in Figure 4.1.

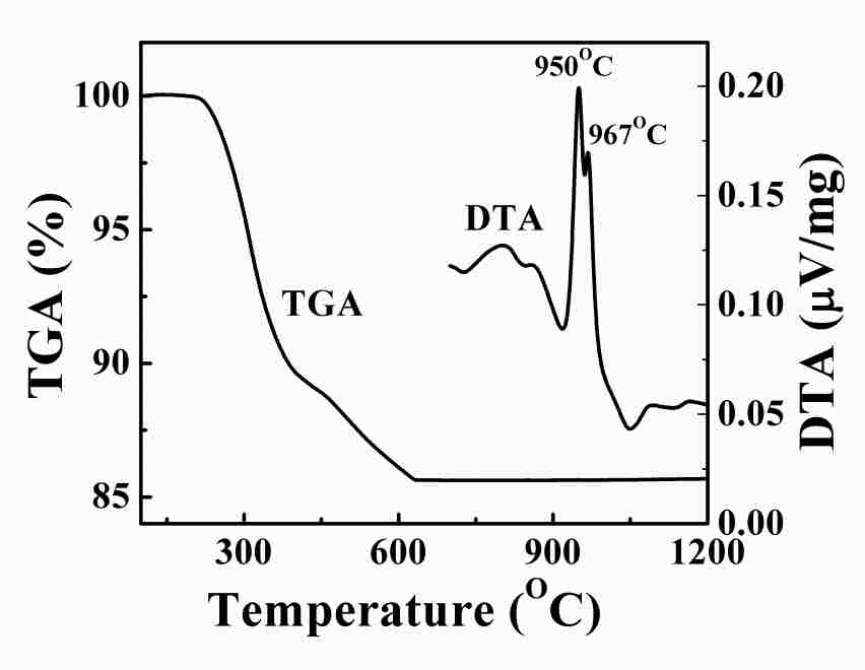

Figure 4.1: TGA and DTA of the green tape at heating rate of 10 ^{O}C/min.

The organic additives decomposed rapidly starting at 200^{O}C continuing to 400^{O}C. Decomposition continued at a reduced rate up to 630^{O}C. The burnt out process was completed by 630^{O}C with a total weight loss of 14.6 wt% at heating rate of 10^{O}C/min. Higher temperature are required to completely burn out the organic additives for faster heating rate. However, the slow burn out process started at around 400^{O}C, which indicates the organic additives can be burnt out at this temperature as long as slow heating rate is employed and enough time is allowed. A slow heating rate of 1^{O}C/min up

to 450^{O}C with 1 h dwell time was applied to burn out the organic additives. Two exothermic crystallization peaks were observed in the DTA curve with two crystallization peaks (T_p) at 950^{O}C and 967^{O}C. The two crystallization peaks were attributed to the β-wollastonite, the low temperature polymorph of $Ca_3Si_3O_9$ and anorthite, $CaAl_2Si_2O_8$ respectively[176].

Figure 4.2 shows the XRD results for specimens sintered at 850^{O}C under heating rate of 1 ^{O}C/min and at 900^{O}C under heating rate of 10 ^{O}C/min.

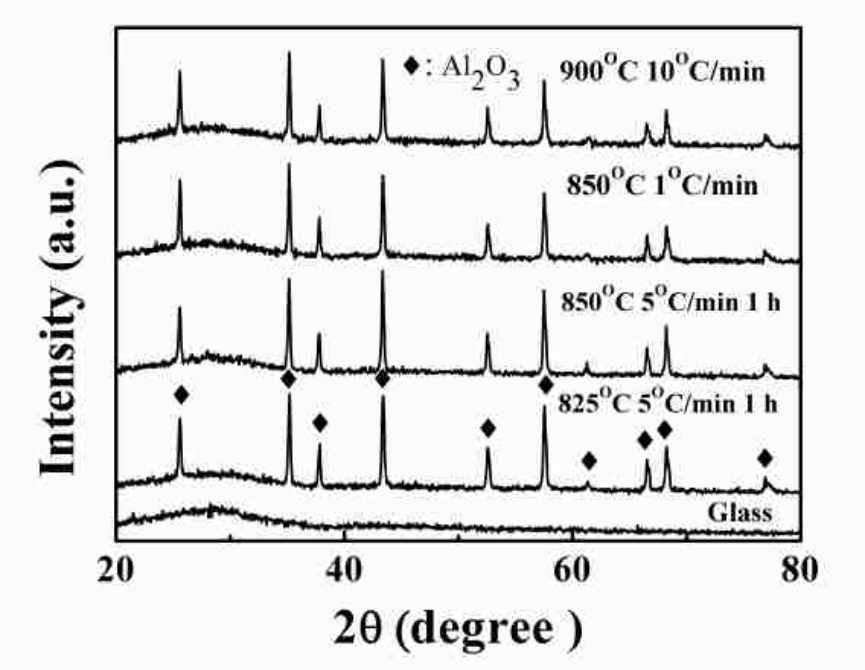

Figure 4.2: XRD of the glass, LTCC sintered at 825^{O}C, 850^{O}C for 1 h with 5 ^{O}C/min heating rate, and LTCC sintered at 850^{O}C with 1 ^{O}C/min heating rate and at 900^{O}C with 10 ^{O}C/min heating rate.

The XRD results indicate only alumina crystal peaks show up in these two samples. In other words, there will be no crystallization for LTCC sintered at temperature up to 850^{O}C with heating rate of 1 ^{O}C/min, 3 ^{O}C/min and 5 ^{O}C/min, and at temperature up to 900^{O}C, with heating rate of 10 ^{O}C/min. No extra crystal peaks show up even for samples

sintered at 825^{O}C and 850^{O}C for 1h. In this experiment, no crystallization occurred in the sintering process, so the MSC approach can be used to accurately predict the viscous sintering densification behavior.

4.4.2 Mater sintering curve study

MSC analysis allows the development of a mathematic model of the densification of the LTCC versus sintering temperature. The densification of the LTCC at different heating rate of 1^{O}C/min, 3^{O}C/min, 5^{O}C/min and 10^{O}C/min are shown in Figure 3. The densification of the LTCC is very sensitive to the heating rate. The LTCC reached full densification at 825^{O}C for heating rate of 1 ^{O}C/min. However, the densification was less than 65% at 825^{O}C for heating rate of 10 ^{O}C/min. The LTCC achieved high densification eventually independent of the heating rate.

Based on the densification data in Figure 4.3, MSC curve was constructed as shown in Figure 4.4 using MSC software[200]. The optimum activation energy is 452.4 kJ/mol, an energy of sintering in this range is consistent with expected values for viscous sintering[184-187].

The MSC curve is unique for a given powder and green-body process independent of the sintering process. Once the MSC curve is constructed, the densification can be predicted under different sintering profile. Heating rate 5 ^{O}C/min was employed to sintering the LTCC at temperature from 725 to 850 ^{O}C. Figure 4.5 presents densification of the LTCC and predicted densification using MSC. The experimental density was very low (<65%) when sintered at 750^{O}C, and increased fast with increasing sintering temperature. The densification of the LTCC was higher than 97% when the sintering

temperature was above 775^{O}C. The highest density was achieved at sintering temperature 825^{O}C. The density decreased with further increase of the sintering temperature, indicating glass blowing due to over firing at temperature higher than 825^{O}C. The predicted densification using constructed MSC curve matched well with experiment value. The experimental densification value was higher than predicted value at temperature 725^{O}C and 750^{O}C, and lower than predicted value at higher temperature. The largest difference between experiment density and predicted value was at temperature 850^{O}C and it implied glass bloating because of over firing. The open porosity of the LTCC also greatly decreased when sintered at temperature 800^{O}C and higher. The shrinkage of the green tape was as high as 17% when sintered at 825^{O}C.

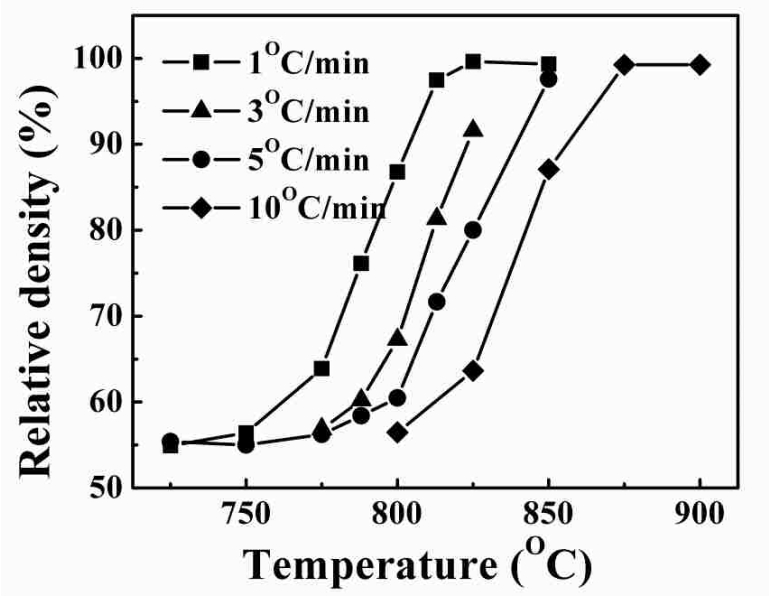

Figure 4.3: The densification of the LTCC versus sintering temperature at heating rates of 1^{O}C/min, 3^{O}C/min, 5^{O}C/min and 10^{O}C/min.

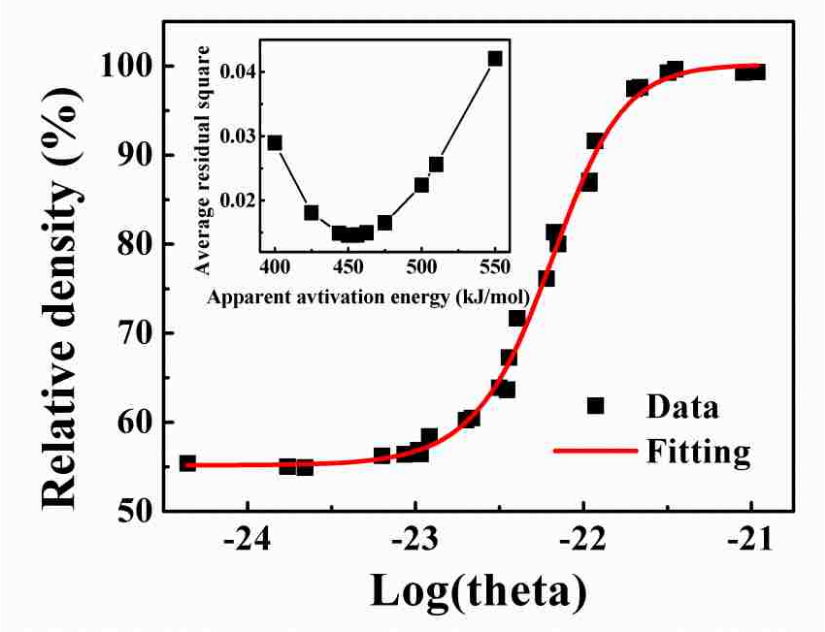

Figure 4.4: Master sintering curve and averaged residual square vs apparent activation energy. The optimum activation energy is 452.4 kJ/mol.

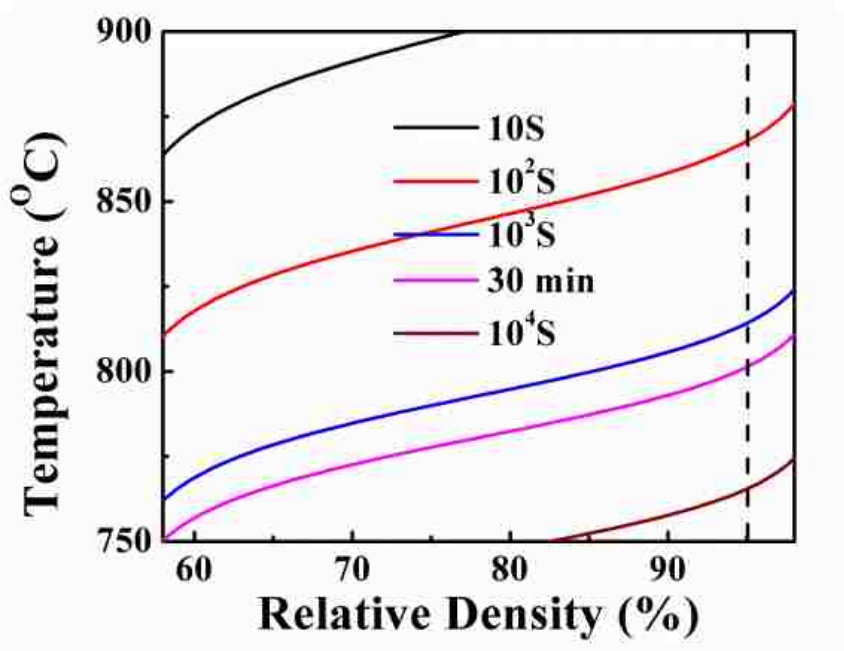

Figure 4. 5: The contour map of the predictions of the sintering time. The dash line is for relative density 95%.

The sintering time required to reach a particular densification at a constant temperature was predicted using the constructed MSC. Figure 6 shows the contour map of the predictions for the sintering time. Less than two minutes were needed to sinter the LTCC with 98% densification at temperature higher than 875^{O}C as shown in Figure 4.6. However, high sintering temperature can easily lead to glass bloating because of high volume of glass phase in LTCC. Certain dwell times are required to co-firing the LTCC and electrode, usually for 20-30 min at peak sintering temperature for commercial available electrode paste. To achieve higher than 95% densification, the sintering temperature for 30 min dwell time predicted by MSC was higher than 800^{O}C.

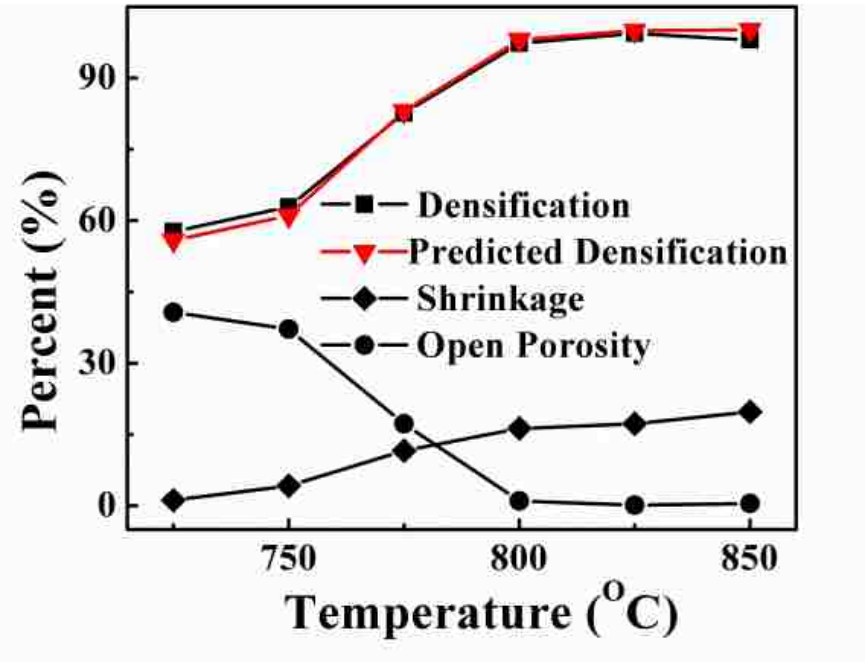

Figure 4.6: Densification, open porosity, shrinkage of the LTCC and predicted densification using constructed MSC curve sintered at different sintering temperature for 30 min.

4.4.3 Microstructure of LTCC and Co-firing with electrode

The microstructure of the LTCC substrate was characterized using SEM. The SEM of the fracture surface of LTCC substrates sintered at 825^{O}C for 30 min are shown in Figure 4.7, revealed dense microstructure. The glass formed interconnected matrix and encapsulated the alumina ceramic particles. Isolated spherical pores with size less than 3 μm were observed in lower magnification micrographs in Figure 4.7(a). These pores were attributed to glass bloating due to over sintering, and this also explains the experimental density was less than the theoretical density calculated using constructed MSC curve as shown in Figure 4.6. Figure 4.8 (a) shows the SEM of the polished fracture surface of the LTCC. Figure (b) and (c) exhibits corresponding alumina and calcium EDS mapping. The bright grains in the SEM were rich in alumina elements. Grey area was rich in calcium. The XRD results in Figure 4.2 demonstrated no crystallization at 825^{O}C, so bright grains were attributed to alumina ceramic and grey area was glass phase.

Compatibility of the LTCC co-fired with electrode was also analyzed. Figure 4.9 shows the interface between the LTCC substrate and the silver (TC0307, Heraeus, Thick Film Division, West Conshohocken, PA) and the interface between the LTCC and gold (TC8101, Heraeus, Thick Film Division, West Conshohocken, PA). No pores, delamination, crack and camber were observed. The smooth interface between the electrode and LTCC indicated no electrode diffusion and reaction happened at this sintering temperature.

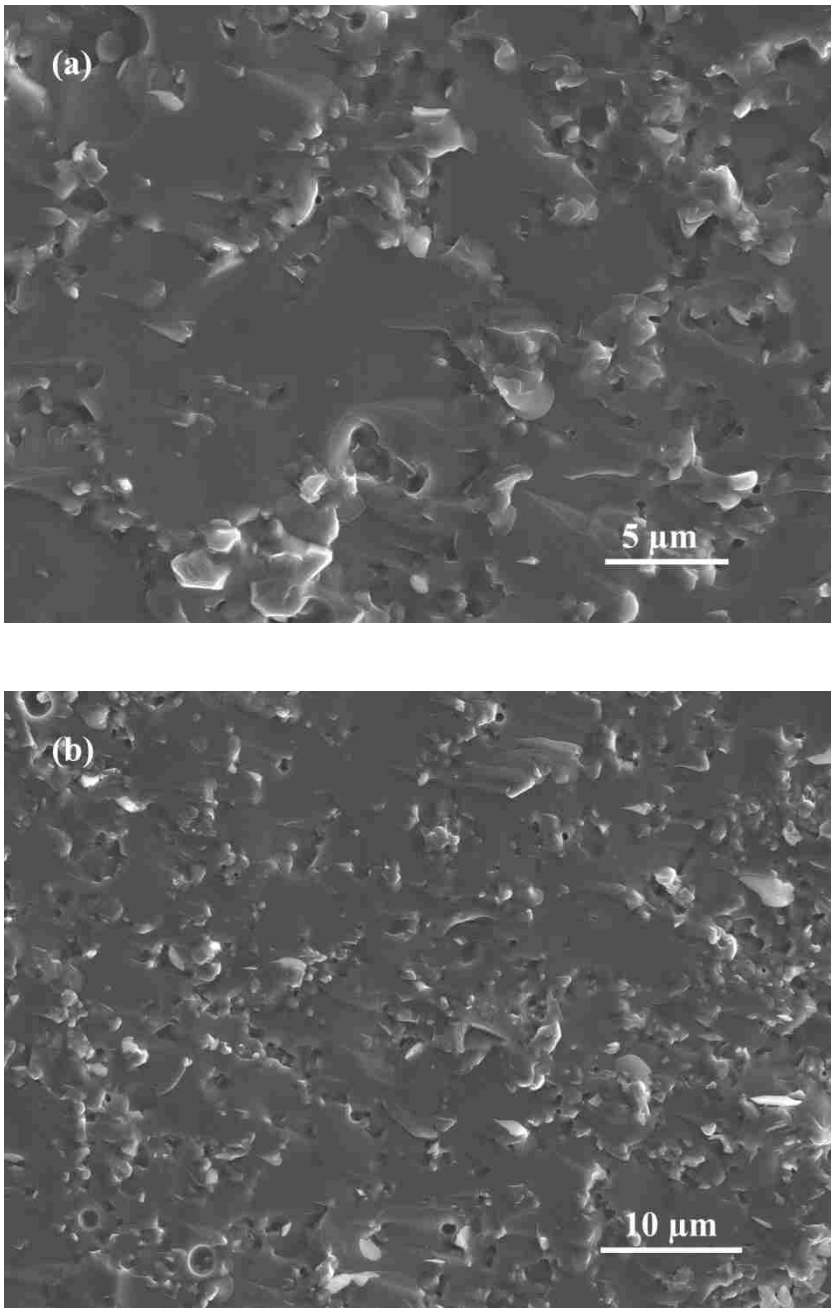

Figure 4.7: SEM of the fracture surface of the LTCC sintered at 825^{O}C for 30 min.

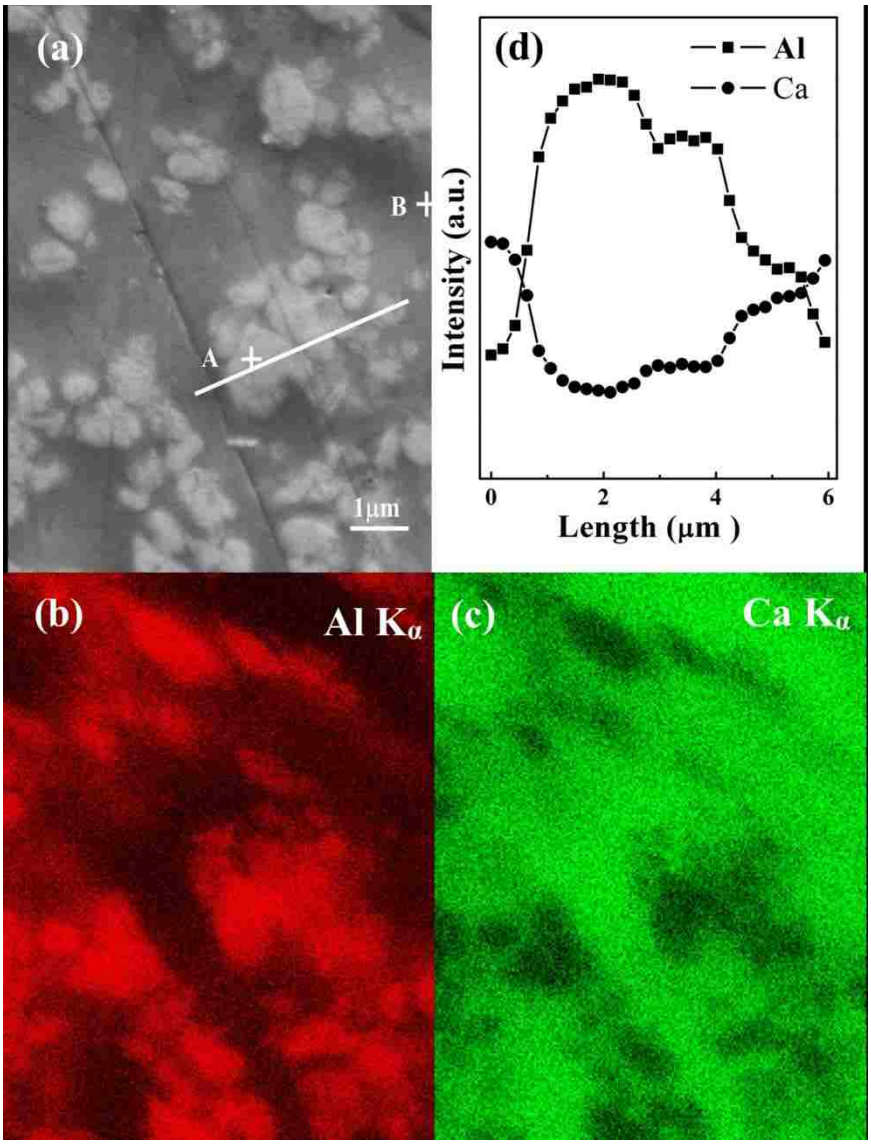

Figure 4.8: (a): SEM of the polished surface of the LTCC sintered at 825^{O}C for 30 min; (b) and (c): the EDS mapping of the element Al and Ca; (d): the intensity of the Al K_α and Ca K_α in the EDS across the line from left to right in the SEM image.

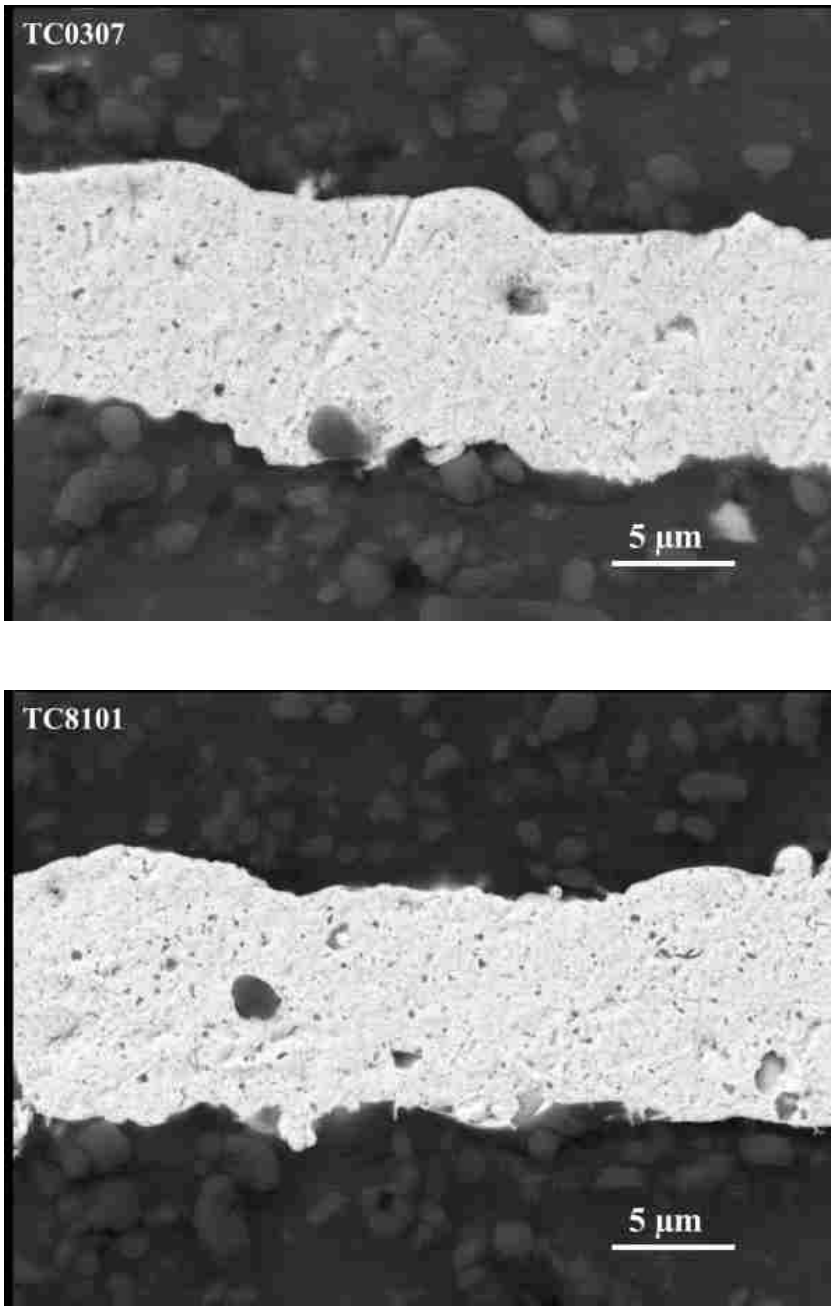

Figure 4.9: Back-Scattered Electron (BSE) images of LTCC cofired with silver (TC0307, Left) and gold (TC8101, Right) at 825^{O}C for 30 min.

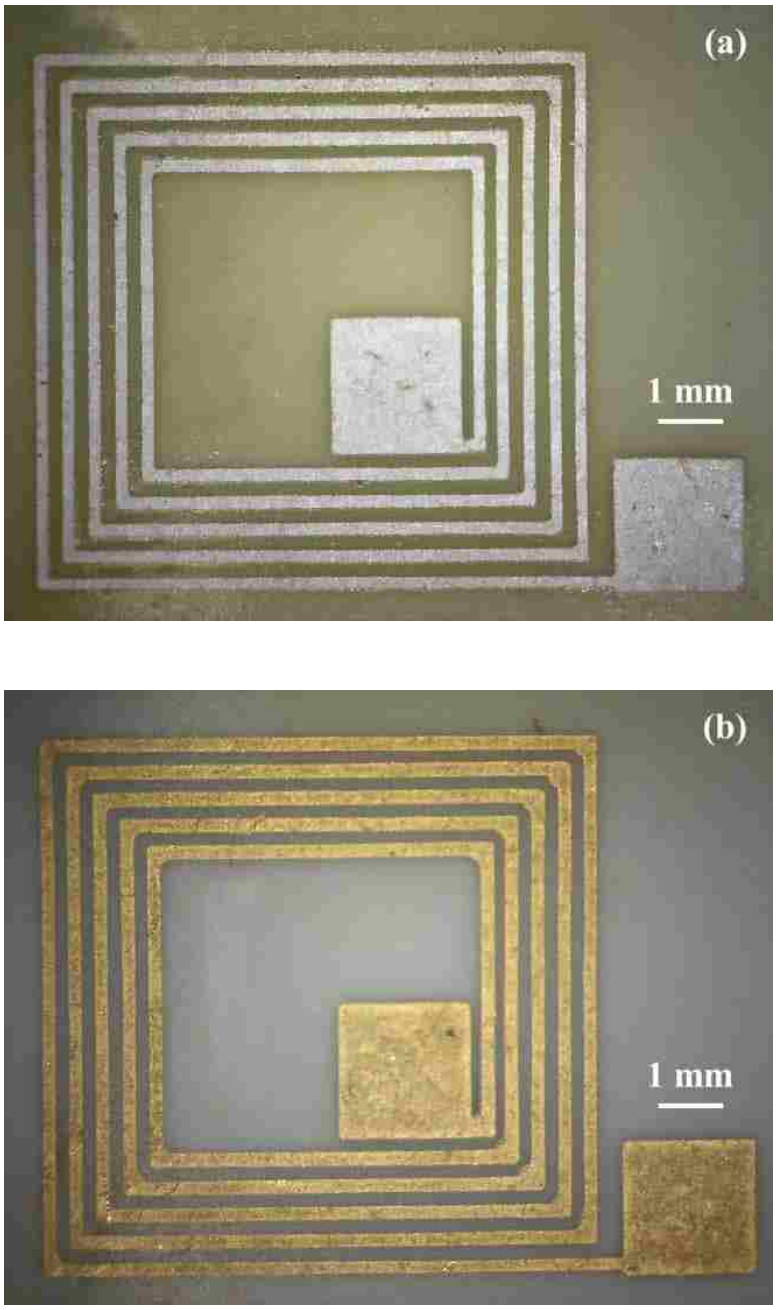

Figure 4.10: Optical images of TC0307 silver (a) and TC8101 gold (b) pattern on LTCC surface after cofired at 825^{O}C for 30 min.

The sheet resistance of these two electrodes was also studied. Silver and gold electrode paste pattern was screen printed with 165 mm length and 250 μm width. The resistances of the electrode lines after co-firing with LTCC at 825^{O}C for 30 min were

measured. The images of the electrode patterns on the surface of LTCC after co-firing were shown in Figure 4.10. Surface resistance was calculated using the following equation:

$$\rho = \frac{RWt}{L}$$

where ρ is the resistivity, and R is the resistance. *W*, t and *L* are the width, thickness and length of the electrode. The results are listed in Table I. The resistivity of gold electrode didn't change much when co-fired on the LTCC surface or buried inside the LTCC. And the resistivity of the silver co-fired in the surface was a little higher than the value of the silver buried in the LTCC. The averaged thicknesses of the silver and gold electrodes buried inside of the LTCC were around 7.4 and 8.3 μm respectively, as shown in Figure 9.

Table 4-1 Surface resistance of the co-fired electrode.

	TC8101	TC0307
Reported Resistivity	$<15\times10^{-8}$ Ω·m	$\leq 4.5\times10^{-8}$ Ω·m
Resistivity on LTCC surface	$9.2\pm0.1\times10^{-8}$ Ω·m	$3.0\pm0.1\times10^{-8}$ Ω·m
Resistivity buried in LTCC	$9.7\pm0.3\times10^{-8}$ Ω·m	$2.5\pm0.1\times10^{-8}$ Ω·m

The dielectric constant was stable at frequency from 1 kHz to 1.5 MHz as shown in Figure 4.11 and it changed from 9.18 at 1 kHz to 9.13 at 1.5 MHz with change less than 1%. Although the dielectric loss increased with increasing frequency, it had value less than 0.15% in the frequency range from 1 kHz to 1.5 MHz. The dielectric constant and loss are comparable to those reported for low loss LTCC[169, 182, 197].

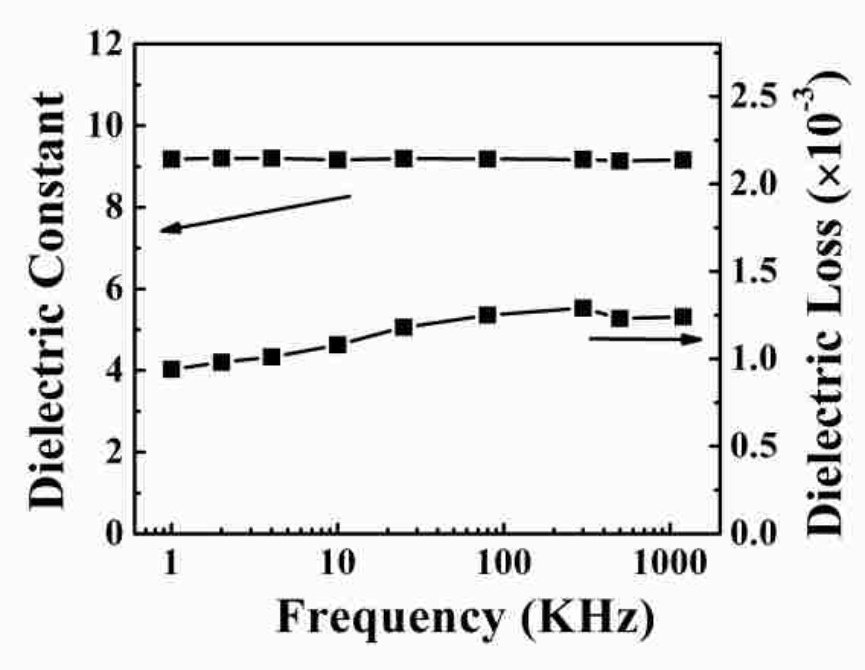

Figure 4.11: Dielectric properties of the LTCC sintered at 825^{O}C for 30 min

4.4.4 Biocompatibility: Cytotoxicity of LTCC leachate

Following procedures described above a standard biocompatibility assay was conducted using the leachate obtained from fresh LTCC substrates following sterilization. LIVE/DEAD results of HUVEC cultured in fresh medium (Control), medium incubated in incubator for 5 days (Blank) and LTCC leachate medium (LTCC) are shown in Figure 4.12. Quantitative image analysis of live cell percent and cell concentration are shown in Figure 4.13. The cell cultured using LTCC leachate medium spread onto the surface. The cell density and live cell percent of LTCC leachate medium are statistically equivalent (p>0.05) between control and LTCC leachate medium.

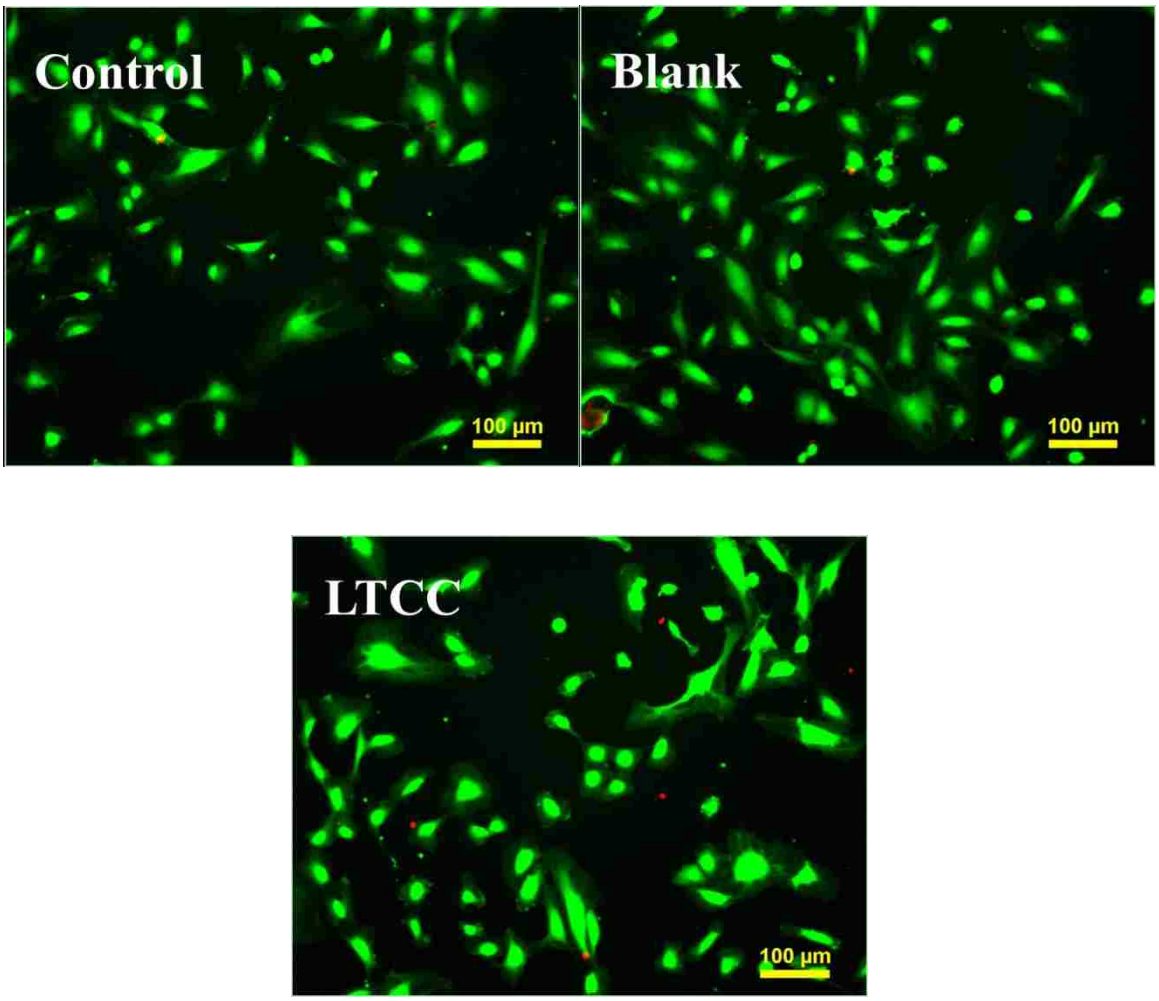

Figure 4.12: LIVE/DEAD images of HUVEC cultured for 1 day using: fresh media (Control), media stored in incubator for 5 days (Blank), or leachate media stored with LTCC in incubator for 5 days (LTCC).

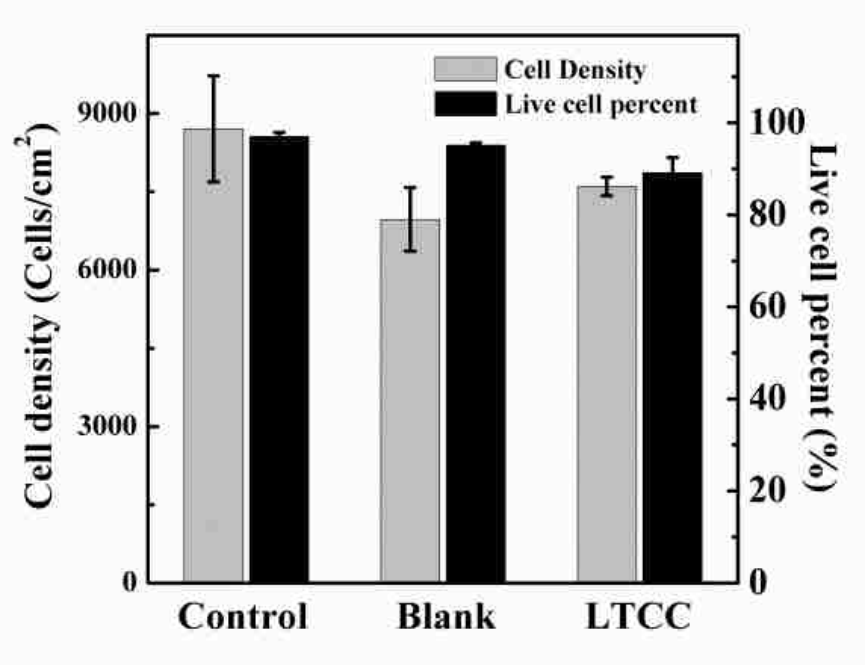

Figure 4.13: Live cell percent and cell concentration from LIVE/DEAD assay of HUVEC cultured for 1 day using: fresh media (Control), media stored in incubator for 5 days (Blank), or leachate media stored with LTCC in incubator for 5 days(LTCC).(Error bars represent standard error). For ANOVA and Turkey test, *p* is 0.02 between control and blank; *p* is 0.65 between control and LTCC, *p* is 0.14 between blank and LTCC.

4.4.5 Biocompatibility: Endothelial cell adhesion and growth

HUVECs were seeded on fibronectin coated LTCC (LTCC) and 24 well tissue culture-treated polystyrene plates (Control). Adhesion was studied after 14 hr, and the proliferation after 74 hr. Cell images on fibronectin coated LTCC and control at 14 hr and 74 hr are shown in Figure 4.14. Cells attached and spread both on control and LTCC after 14 hr and cells proliferated on both samples after 74 hr. Quantitative image analysis of the cell density and live cell percent at 14 hr and 74 hr are shown in Figure 4.15. Although more dead cell exhibited on LTCC after 14 hr, the live cell density of LTCC was statistically equivalent ($P>0.05$) to that of control after 14 hr. The cell concentration on control and fibronectin coated LTCC substrate significantly increased after 74 hr. Live

cell percent on LTCC surface were statistically equivalent to that of control with value higher than 99% after 74 hr. The cell number on fibronectin coated LTCC were higher than that of control after 74 hr.

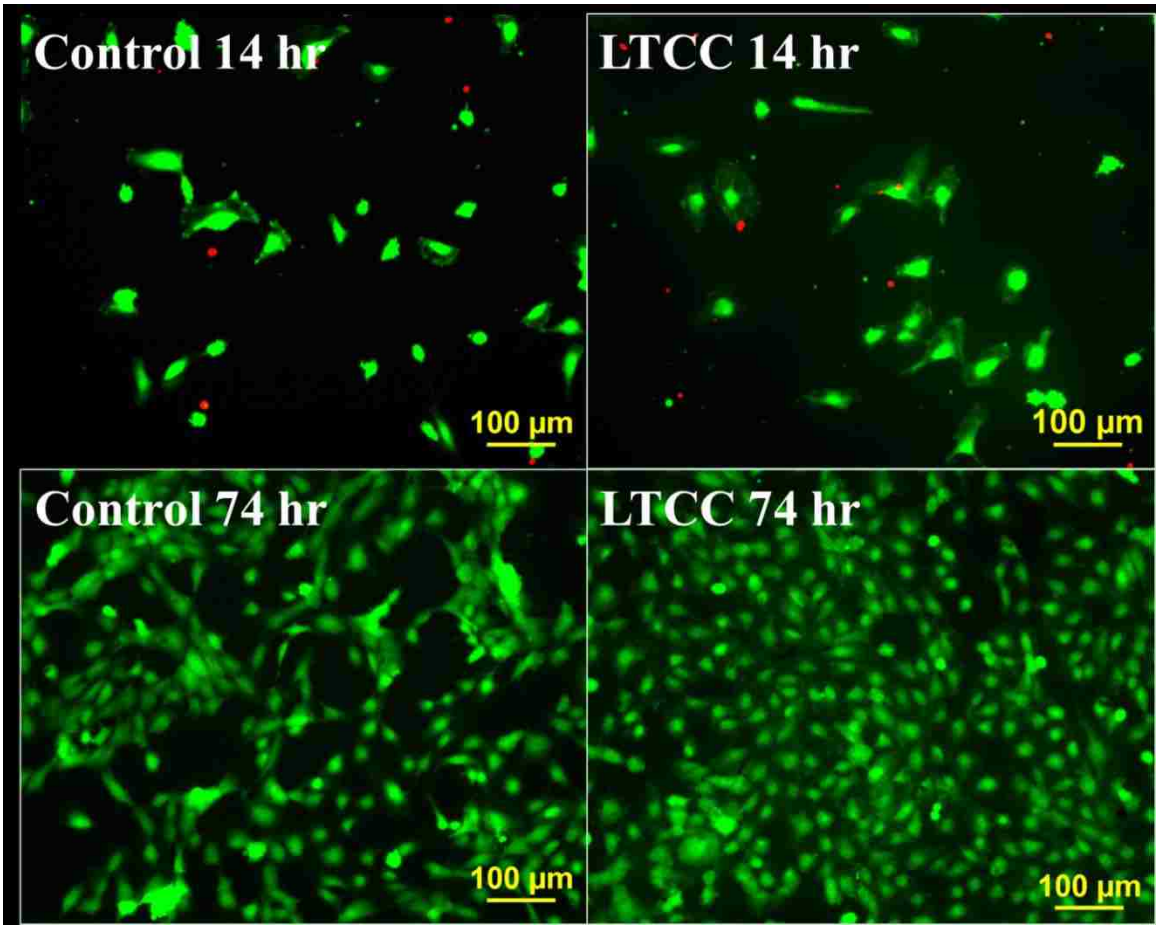

Figure 4.14: Pictures of the cultured cells on the well plate (control), and on the fibronectin coated LTCC surface (LTCC) for 14 hr and 74 hr.

The higher proliferation rate observed on LTCC substrate may be due to surface morphology and element leachate. First the rough surface of LTCC in this experiment may be beneficial to the proliferation of HUVECs. The roughness of the surface effects the growth of all kinds of cells and the topographies of the surfaces on LTCC may be related with the improved HUVECs growth[205]. Second enhanced proliferation may be

likely due to dissoluted ions from the glass phase, such as Ca^{2+}. The calcium leachate rate of HL2000 LTCC in physiological solution has been reported to be 1.48×10^{-2} μg/cm^{2}h [37]. Dissolution of calcium from the glass phase may stimulate the HUVECs differentiation and proliferation in this experiment. And this may also explain the cell concentration in LTCC leachate medium were a little higher than blank in cytotoxicity study of the LTCC as shown in Figure 4.12 and 4.13. More experiments are needed to analyze the glass dissolution and effects of ion dissolution on HUVECs proliferation.

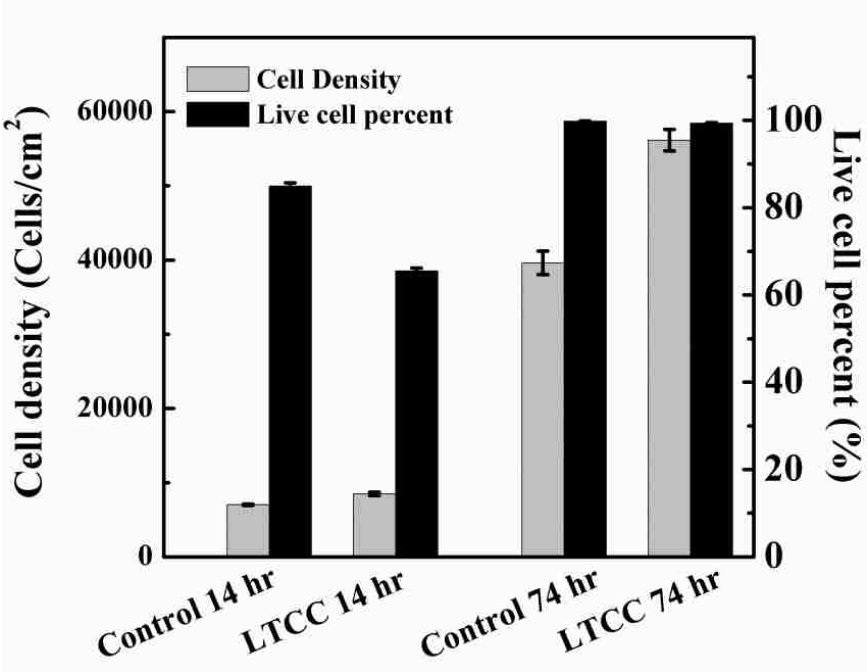

Figure 4.15: Live cell percent and cell concentration of the cultured cells on the well plate (control), and on the fibronectin coated LTCC surface (LTCC) for 14 hr and 74 hr. For ANOVA and Turkey test, *p* is less than 0.001 between control and blank after 14 h cell culture; *p* is less than 0.001 between control and LTCC for 74 h cell culture.

4.5 Conclusion

An LTCC with 75 vol% borosilicate glass frit and 25 vol% alumina was fabricated using tape casting method. DTA and XRD results indicated no formation of secondary

crystalline phase at sintering temperature less than 900^{O}C. MSC curve was constructed to analyze the densification behavior and apparent activation energy of the LTCC for optimization of the sintering process, and the apparent activation energy was estimated to be ~ 452.4 kJ/mol. The densification predicted using constructed MSC was in good agreement with experimental value. The dielectric properties of the LTCC were also studied, demonstrating dielectric properties suitable for low dielectric constant LTCC materials. The dielectric constant of full sintered LTCC was stable, with value less than 9.5, and the dielectric loss was less than 0.15% in the frequency range from 1 kHz to 1.5 MHz. Biocompatibility was demonstrated by seeding of endothelial cells (HUVEC) in LTCC leachate medium and on fibronectin coated LTCC substrate. The cell density and percentage of live cells cultured after 1 day in LTCC leachate were comparative with those of control. The cells attached, spread and proliferated on fibronectin coated LTCC. The results indicate developed LTCC are biocompatible and can be regarded as a potential candidate in the microfluidic and lab on the chip application using live cell sensing.

Chapter 5 A low temperature co-fired ceramic (LTCC) microfluidic Clark-type oxygen sensor for real-time oxygen sensing

5.1 Introduction

In this work, we present a design and development of a microfluidic LTCC based Clark-type oxygen sensor for the real-time assessment of localized dissolved oxygen. LTCC materials were chosen because of its ease fabrication, rapid prototyping, fast incorporation of electronic and microfluidic components. The microfluidic oxygen sensor consisted of an LTCC substrate with electrodes for detecting electrochemical signals, solid-state electrolyte, oxygen permeable membrane, and a fluidic microchannel sealed to a glass slide. A solid proton conductive electrolyte was chosen instead of liquid electrolyte and microfluidic function was realized easily in this system. Since the reduced current was detected with testing solution flowing in microchannel and the old solution was replaced by new solution during the testing, the problem of the oxygen consumption was solved in this microfluidic oxygen sensor. And it can also be used to monitor the change of dissolved oxygen over time. The usage of solid-state proton conductive matrix (PCM) membrane also provides mechanical support to gas permeable membrane and eventually extends the lifetime of the membrane. Clark-type oxygen sensor reported in the literature only detected dissolved oxygen in static fluids in biological environment, and flowing of the testing samples would lead to signal shift or change[39, 40, 142]. The developed device was capable of oxygen delivery and real-time detection of dissolved

oxygen in a flowing medium at various flow rates. Incorporation of microfluidic function to the integrated Clark-type oxygen sensor is a unique improvement for the potential application in biological assays and bioreactor.

The delivery of oxygen supply and accurate measurement of dissolved oxygen concentration are very important in the environmental monitoring, biological assays, bioreactors and other applications[40, 41, 93, 97, 106, 108, 148]. Oxygen sensing has been frequently used to monitor the cellular metabolic activity and rapidly determine the cell viability [40, 93]. Adequate supply of oxygen plays a key role in cell proliferation and differentiation, and abnormal supply of oxygen may lead to a diseased state[206]. Monitoring cellular oxygen consumption rates and cellular respiration provides important information for metabolism, apoptosis, mitochondrial function, toxicological responses to various drugs in the critical biochemical study[106, 206]. There is an increasing need for the development of low-cost, flexible oxygen sensor with easy and rapid fabrication as the integrated microfluidic devices for biological applications.

Two common techniques for sensing dissolved oxygen in microfluidic applications are luminescent optical sensing and electrochemical sensing. Both demonstrate high sensitivity to oxygen at low concentration[101]. The mechanism of luminescent optical sensing is based on the excitation of fluorescent dyes encapsulated in a polymer matrix and that the luminescent intensity and lifetime are related with oxygen concentration[102]. Fluorescent oxygen sensing (such as the XF Extracellular Flux Analyzer recently commercialized by Seahorse Biosciences) has seen widespread adoption due to its inherent stability[207]. However, the applications of this technique are limited by the complicated fabrication and expensive lifetime-sensing apparatus[105, 142, 208]. Fluorescent

sensing also has a longer response time than electrochemical oxygen sensors. Electrochemical sensors are widely used and available in a number of styles from various manufacturers[142, 209]. The most common embodiment of the electrochemical sensor is the Clark-type configuration, incorporating a cathode, anode, electrolyte solution and a gas permeable membrane. The majority of these sensors require large sample volumes (10's-100's mL), employing macroscopic probe style electrodes which must be immersed into the specimen of interest. The principle of amperometric devices is to take advantages of electrochemical reaction of dissolved oxygen and detect reduced current which is proportional to the dissolved oxygen concentration. The advantages of Clark type dissolved oxygen sensor are easy fabrication, low cost and fast response compared with luminescent sensing technique. However, those sensors also have some limitations and suffer from problems such as consumption of dissolved oxygen at the working electrode which results in the change of oxygen concentration in the sample solution. Due to the consumption and local depletion of the dissolved oxygen mechanical agitation or circulation of the testing sample may be required[40, 142]. Thin gas permeable membrane suspended on top of liquid electrolyte in the Clark-type oxygen sensor also lead to susceptibility of membrane failure by mechanical agitation. It is also difficult to adapt the functionality of this type of sensor to continuous monitoring, automation and high-throughput measurements[210]. However, several microfabricated sensors are available for microfluidic and high throughput sensing. These include probe style sensors (such as from Strathkelvin Instruments) incorporating microelectrodes to reduce oxygen consumption and sample volume requirements (~100 μL), and single or multiwell plates,

up to 90 wells (from Bionas GMBH), incorporating printed microelectrodes. In the current work, these concepts are expanded upon for use in a microfluidic flow cell.

5.2 Sintering of LTCC: Self-constrained sintering

One of the limitation of the LTCC process is shrinkage in the x, y directions during the sintering process[45], typically from 10 % to 15 %. The shrinkage in x, y directions is identical to or slightly different from that in z direction. Shrinkage variation in lateral direction occurs in free sintered composites, which is up to 0.5%. This leads to the difficulty to control the geometric precision, and further limits the capability to large volume production of modules in the LTCC[211-213]. Zero shrinkage technology is an option, which limits the transverse shrinkage to a great extent and only allows longitudinal shrinkage. The technology used in LTCC sintering includes self-constrained sintering, pressure-assisted sintering, pressureless-assisted sintering and LTCC-M method, which uses metal as substrate[213-216]. HeraLock^{TM} HL2000 tape has been developed using self-constrained sintering method, and it has shrinkage 0.2 % in x, y direction and tolerance ±0.02% after sintering[211, 212]. This tape was processed without sacrificial layer and sintered without pressure.

This tape contains three layers of tape sintering at different temperature intervals. The top and bottom layers have regular LTCC formulation with ceramic filler and a glass. The middle layer is the self-constraining layer and consists of a refractory ceramic and a wetting agent that help the glass phase in top and bottom layers diffuse into the porous in the middle layer[211]. Figure 5.1 shows 178 mm × 280 mm LTCC laminate cut in half with

and without sintering. The low shrinkage and shrinkage tolerance of the HL2000 LTCC enable production of LTCC components with large panel sizes.

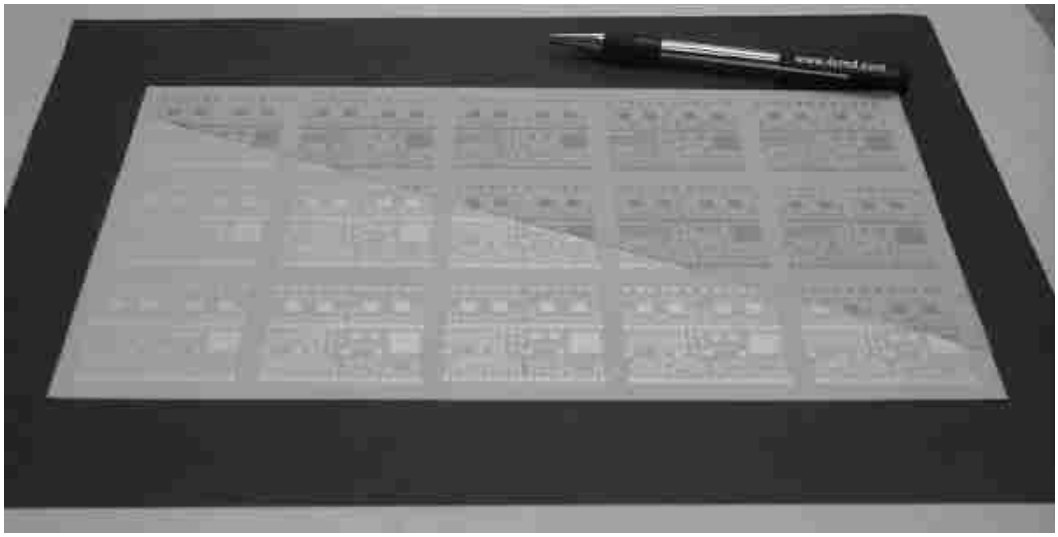

Figure 5.1: Image of the HL2000 LTCC with plenty of electrical circuits before and after sintering to demonstrate zero shrinkage in x,y direction. Reprinted from the reference[211].

5.3 Experimental:

5.3.1 Geometry and design of microfluidic flow cell incorporating Clark-type electrodes

This LTCC based Clark type oxygen sensor was mainly composed of LTCC substrate with three electrodes (Au working electrode, Au counter electrode and Ag/AgCl reference electrode), Nafion solid-state electrolyte, PDMS gas-permeable membrane, a PDMS storage channel for testing sample and glass cover sealed to the channel. The inlet and outlet connected with microfluidic channel for the sample solution was included in the LTCC substrate layer. Figure 5.2 shows the basic structure of Clark type oxygen sensor.

PDMS was chosen as oxygen permeable membrane in this device because of its high permeability to oxygen gas[101]. In addition, the hydrophobic PDMS membrane also isolated the electrolyte and electrode from the sample medium, which prevents the interference of other reactive and electroactive species. DPMS was also used as the material for the microfluidic channel due to its non-toxicity and easy fabrication with soft lithography rapid prototyping techniques. The disposable PDMS microfluidic layer allowed easy reconfiguration using soft lithographic techniques without requirement for the change of LTCC substrate. Various channel sizes can be employed using the same reusable electrode substrate. PDMS material used both as gas-permeable membrane and microfluidic channel improved the adhesion between LTCC substrate and the microfluidic layer under mechanical fixation.

The final dimension of the sintered LTCC substrate with total thickness 0.7 mm was 3.8×3.6 mm. The surface area of working, counter and counter electrode were 0.2 mm^2, 0.75 mm^2 and 1.5 mm^2 respectively.

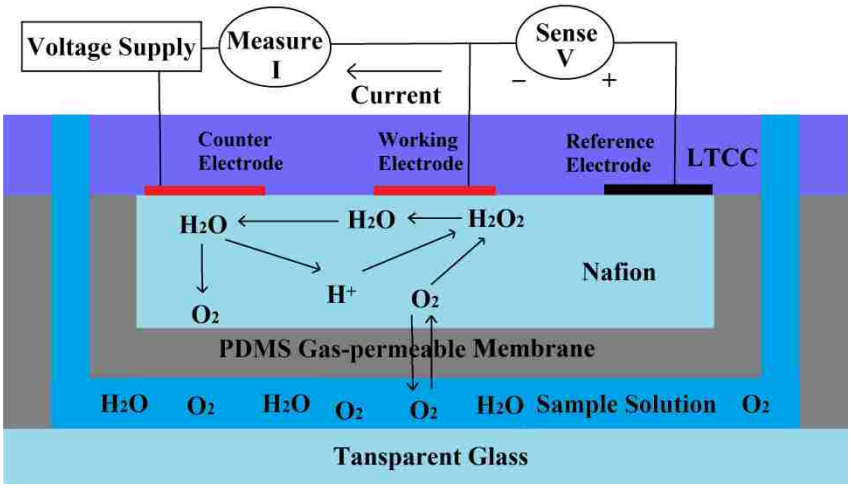

Figure 5.2: Schematic illustration of the reaction mechanism and conceptual presentation of the microfluidic LTCC based Clark-type oxygen sensor.

5.3.2 Fabrication of LTCC substrate with Clark-type electrodes

Fabrication of microfluidic flow chambers and microelectrodes was performed using typical multilayer co-fired ceramic processing methods. For prototyping purposes, commercially available HL2000 green tapes (Heraeus, Thick Film Division, West Conshohocken, PA) were used as substrate materials. Electrical conductors were printed using TC8101 gold paste (Heraeus) for working and counter electrodes, and TC0307 silver paste (Heraeus) for fabrication of reference electrode. The cavities (inlet and outlet) and channels in the green tapes were cut using a CO_2-laser milling system (VLS 3.50, Univer-sal Laser Systems, Scottsdale, AZ). Green tapes were then laminated together under pressure 6.1 MPa at 75 ^{0}C for 10 min using a uniaxial press (3851, Carver, Wabash, IN). Subsequently, another layer of green tape (layer 7) was laminated on top under pressure 6.1 MPa at 75 ^{0}C for 20 min as an insulator layer to define the sensitive area of the electrodes. The consolidated laminate was trimmed with a razor blade and sintered following manufacturer's guidelines, 1 ^{0}C/min up to 450 ^{0}C then 7 ^{0}C/min up to 875 ^{0}C with a 30 min hold followed by inertial cooling. Chemical oxidation with aqueous $FeCl_3$ (Fisher Scientific) was used to produce AgCl. A 0.1 M $FeCl_3$ was applied to sintered Ag electrode for 10 min at room temperature. DI water was used to clean the substrate.

5.3.3 Incorporation of solid-state electrolyte and oxygen permeable membrane

A polymeric proton conducting membrane (PCM) was used as solid electrolyte. The PCM solution consisted of a mixture of one part of 5 wt.% Nafion 117 (Aldrich) solution and one part of 1.25 wt.% polyvinylpyrrolydone (PVP360, Sigma) and 0.04 wt.% addition of 2,6-bis(azidobenzylidene)-4-Methylcyclohexanone)) (Santa Cruz

Biotechnology). Nafion provides the required proton conductivity and PVP improved adhesion between the electrode and LTCC surface.

To prepare the surface, the LTCC substrate was dipped into a mixture of 3-(trimethoxysilyl) propyl methacrylate (Acros), ethanol and dilute acetic acid (1:10 glacial acetic acid:water) in a ratio of 1:200:6 for 3 min. The substrate then was rinsed with ethanol to remove any residual reagent, and dried thoroughly at 60 ^{0}C for 5 min. The PCM solution was pipetted on the device surface and dried at 70 ^{0}C for 1 h. The thickness of the PCM membrane was ~8.4 µm, observed using optical microscopy.

The PCM membrane was then covered by an oxygen permeable membrane (OPM). The OPM was prepared from a mixture of PDMS (polydimethylsiloxane, Sylgard 184, Dow Corning) with curing agent in a weight ratio 10:1. Xylene was used to adjust the viscosity in order to obtain uniform PDMS membrane with desired thickness. The LTCC substrate was spun at 2000 rpm and the xylene-PDMS mixture (1: 3, v/v) was spread on the surface for 1 min. And the PDMS was cured at 60 ^{0}C for 2 h and the thickness was ~ 20.8 µm observed under optical microscopy.

5.3.4 Fabrication of PDMS channel and its bonding to LTCC substrate

The channel layer was fabricated from 1 mm thick PDMS The channel, with width 2.2 mm and length 23 mm, was cut using CO_2-laser milling system. A transparent glass was cut into suitable size and cleaned in isopropanol and dried. Both the glass and PDMS-channel layer were treated with O_2 plasma, and the plasma treated surface of the PDMS was pressed against on the plasma treated surface of the glass. Irreversible cross-linking between PDMS and glass surface results in strong adherence of the two materials.

The LTCC substrate with PCM membrane and OPM was placed on top of boiled water for 1 h in order to saturate the PCM membrane with water. The LTCC substrate and PDMS-glass substrate were manually aligned and mechanically secured with spring clips. Figure 5.3 shows the image of the bonded microfluidic LTCC based Clark-type oxygen sensor.

5.3.5 Characterization of the LTCC based oxygen sensor

Commercially available dissolved oxygen meter was purchased from Milwaukee (MW600) to monitor the dissolved oxygen in the solution. Both cyclic voltammetry and chronoamperometry measurement were used to obtain the calibration curves and quantify the oxygen concentration by measuring the reduced oxygen currents. To get sample solution with specific oxygen concentration, N_2 gas was flown into the solution for 10 min and 0.1 wt.% sodium sulfite was added to stabilized oxygen concentration of the solution at open environment. And then the solution was magnetically stirred, and dissolved oxygen meter was used to monitor the oxygen concentrations. And stirring should stop when the oxygen centration reached expected value. Oxygen depleted solution was prepared by adding 0.1 M sodium sulfite. The electrochemical measurements and characterization were performed using a potentiostat (MPG-2, Bio-logic) with computerized control and data acquisition software (EC-Lab V10.32).

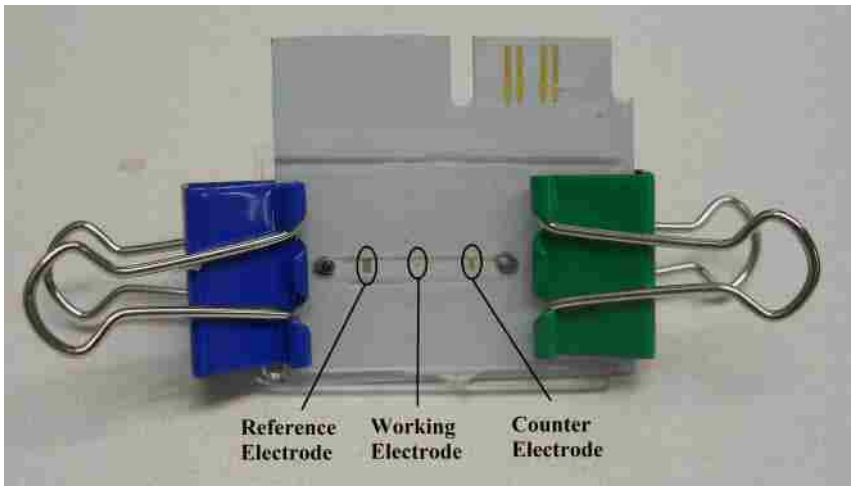

Figure 5.3 Image of the bonded microfluidic LTCC based Clark-type oxygen sensor.

5.4 Results and discussion:

5.4.1 Theory of operation

The reaction mechanism of Clark type oxygen sensor is based on the electrochemical reduction of the dissolved oxygen which diffuses through gas permeable membrane to the electrolyte at the working electrode. Figure 5.2 shows the reaction mechanism at the working and counter electrode. The reduction of dissolved oxygen at the working electrode is a two-process step[98]. The reaction was summarized by:

$$O_2+2H^++2e^-\rightarrow H_2O_2 \quad (6.1)$$

$$H_2O_2+2H^++2e^-\rightarrow 2H_2O \quad (6.2)$$

The reaction at the counter electrode was production of oxygen:

$$2H_2O\rightarrow O_2+4H^++4e^- \quad (6.3)$$

5.4.2 Cyclic voltammetry of the sensor

Cyclic voltammetry measurements were used to determine the bias point for oxygen reduction and verify that there is no other competitive reaction at the selected bias point. Cyclic voltammetry measurements for oxygen reduction in oxygen saturated DI water was performed over a voltage range from 0 V to -1.0 V with scanning rate 100 mv/s, as shown in Figure 5.4. With the initial application of a negative voltage (starting from 0 V), a commensurate change in the current was observed, consisting with a kinetically limited reaction. The plateau current started to appear around an applied voltage of -0.75 V. The diffusion controlled region for oxygen reduction was observed to be in the range of -0.75 V to -1.0 V, and no other competitive reaction was observed. The subsequently chronoamperometric reduction currents measured at an applied voltage -0.75 V were used to characterize the oxygen concentration.

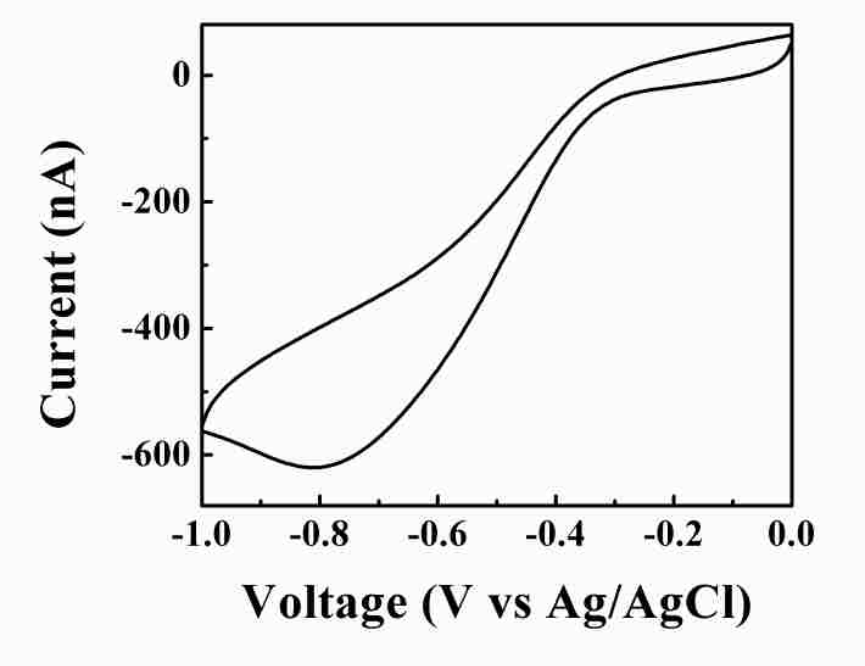

Figure 5.4: Cyclic voltammetry of the DI water

5.4.3 Oxygen sensing and flow rate effects

Initial evaluation focused on the dynamic range of the developed sensor for oxygen saturated and oxygen depleted solutions of Dulbecco's phosphate-buffered saline (DPBS, 4 g NaCl, 0.5 g Na_2HPO_4, 0.1 KCl and 0.1 g KH_2PO_4 in 500 mL DI water), as shown in Figure 5.5. Chronoamperometry was used to determine the dynamic behavior of the device. The measurement was obtained by applying a step voltage change from -0 V to -0.75 V and measuring the current response for 1 min. DPBS was saturated with oxygen by bubbling with O2 gas for 5 min. Dissolved oxygen in DPBS can be easily depleted by adding sodium sulfite (Na_2SO_3). The averaged current detected in oxygen depleted DPBS in static condition was -4.9±1.7 nA (mean ± SD), and no big change was observed for flow rate 0.2, 0.5, 1.0 ml/min.

The current values greatly increased for oxygen saturated DPBS compared with oxygen depleted solution, and the higher current response corresponded to higher flow rate. The current values gradually decreased after the application of a voltage step for oxygen saturated DPBS when the solution was not flowing. The averaged currents measured in chronoamperometry curves from 55 s to 58 s were -306.5±5.3 nA (mean ± SEM, n=6). However, the current value reached a steady state for flow rate 0.2, 0.5, 1.0 mL/min. The times for the current to reach the plateau were 10 s, 11 s and 14 s for flow rate 0.2, 0.5, 1.0 mL/min respectively. The averaged currents at steady state measured in chronoamperometry curves were -418.9±1.8 nA, -469.3±2.2 nA and -502.7±2.4 nA (mean ± SEM, n=6) for flow rate 0.2, 0.5, 1.0 mL/min respectively.

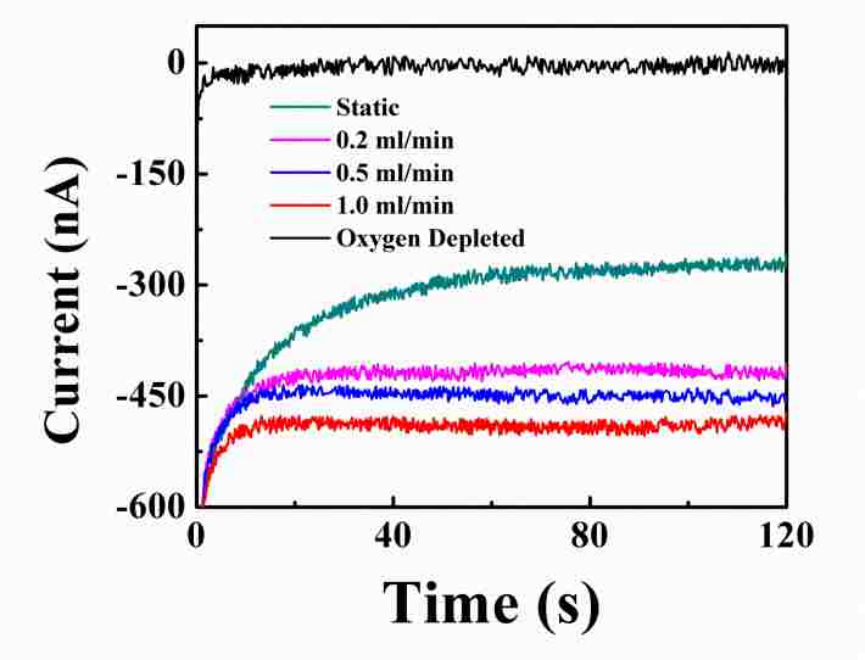

Figure 5.5: Chronoamperometry of oxygen saturated DPBS under different flow rate, and chronoamperometry of oxygen depleted DPBS

5.4.4 Medium effects on measured oxygen concentrations

Oxygen concentrations in the DI water and DPBS with the same dissolved oxygen were tested using developed oxygen sensor. The chronoamperometry curves of DI water and DPBS demonstrated the similar trend as shown in Figure 5.6, which indicates the positive and negative ions in DPBS showed no effects on the chronoamperometry results under static and flow conditions.

Nafion membranes have a wide application due to their high ion conductivity[217]. However a trace amount of cations, such as Na^+, Ca^{2+}, Li^+ and K^+ will contaminate the Nafion membrane. These cationic ions will replace protons in Nafion, because these cationic ions have higher affinity with sulfonic acid group ($-SO_3-$) in Nafion than protons, which will further results in considerably different conductivities[218]. Nafion electrolyte

will easily be contaminated by the reagent in the sample solution if the Nafion electrolyte was directly contacted with testing sample, which will leads to discontinuity between different solution and unexpected interference signal. The advantage of the fabricated sensor was that the solid state Nafion membrane was coated with a gas permeable membrane, PDMS. PDMS was not only permeable to gas but also acted as protective layer for Nafion electrolyte. At the same time, the solid-state PCM electrolyte also provides mechanical support for PDMS oxygen permeable membrane, and prevents the mechanical failure during the usage, which increasing lifetime of the membrane.

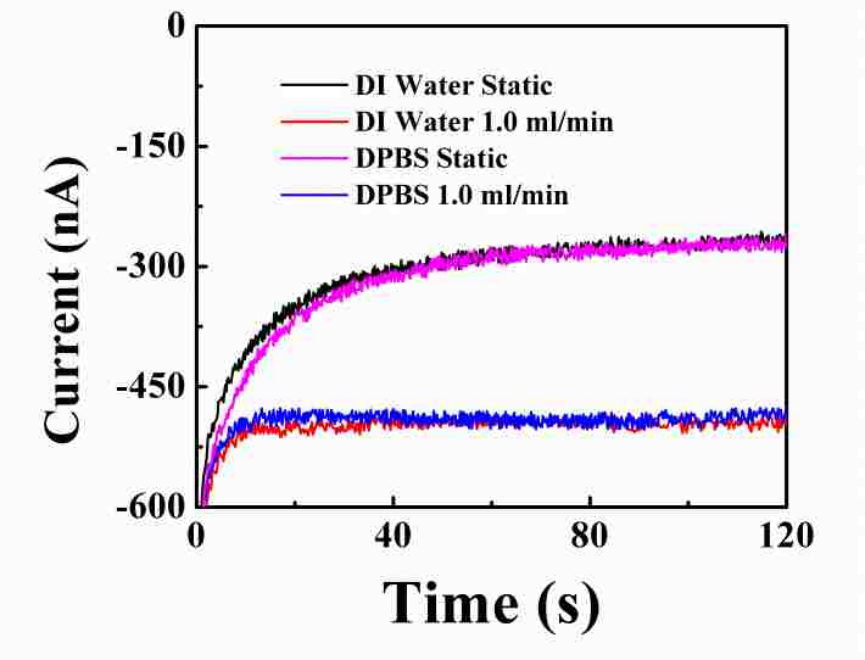

Figure 5.6 Chronoamperometry of the oxygen saturated DI water, DPBS under different flow rate.

5.4.5 Calibration curve

The oxygen in DI water was depleted through bubbling N_2 gas, and 0.06 wt.% sodium sulfite was added to stabilize the oxygen concentration in the open environment and the dissolved oxygen concentration was adjusted through magnetically stirring the DI water. Solutions of different dissolved oxygen concentration were introduced into the sensor at various flow rates to obtain chronoamperometry curves. Figure 5.7 to Figure 5.11 shows the resulting calibration curves under flow rates of 0.0, 0.2, 0.5, 1.0 mL/min. Higher current values in chronoamperometry curves corresponded to larger dissolved oxygen concentration. The dissolved oxygen concentrations tested were in the range from 0.0 to 8.1 mg/L. All fitted calibration curves demonstrated a good linear relationship, with correlation coefficients 99.77%, 99.54%, 99.66%, 99.67% for flow rate of 0.0, 0.2, 0.5, 1.0 mL/min respectively, which indicate negligible or no crosstalking between electrodes. The slope coefficient and residual currents of the fitted calibration curves were shown in table I. The slope coefficient increased with the increase of flow rate. The averaged residual current for oxygen depleted solution measured in oxygen depleted solution were 3.4%, 1.0%, 1.0% and 2.0% of the current measured in oxygen saturated solution for flow rate 0.0, 0.2, 0.5, 1.0 ml/min respectively. The residual currents measured in this experiment were comparable to that of the Wu et al.' works[39] and Suzuki's studies[122, 130].

The reduced currents in DPBS were also measured to verify the calibration curve, and the data were also fitted well into the calibration curve under different flow rates. The developed oxygen sensor can be used to detect the dissolved oxygen in real time regardless of the ions in the testing sample

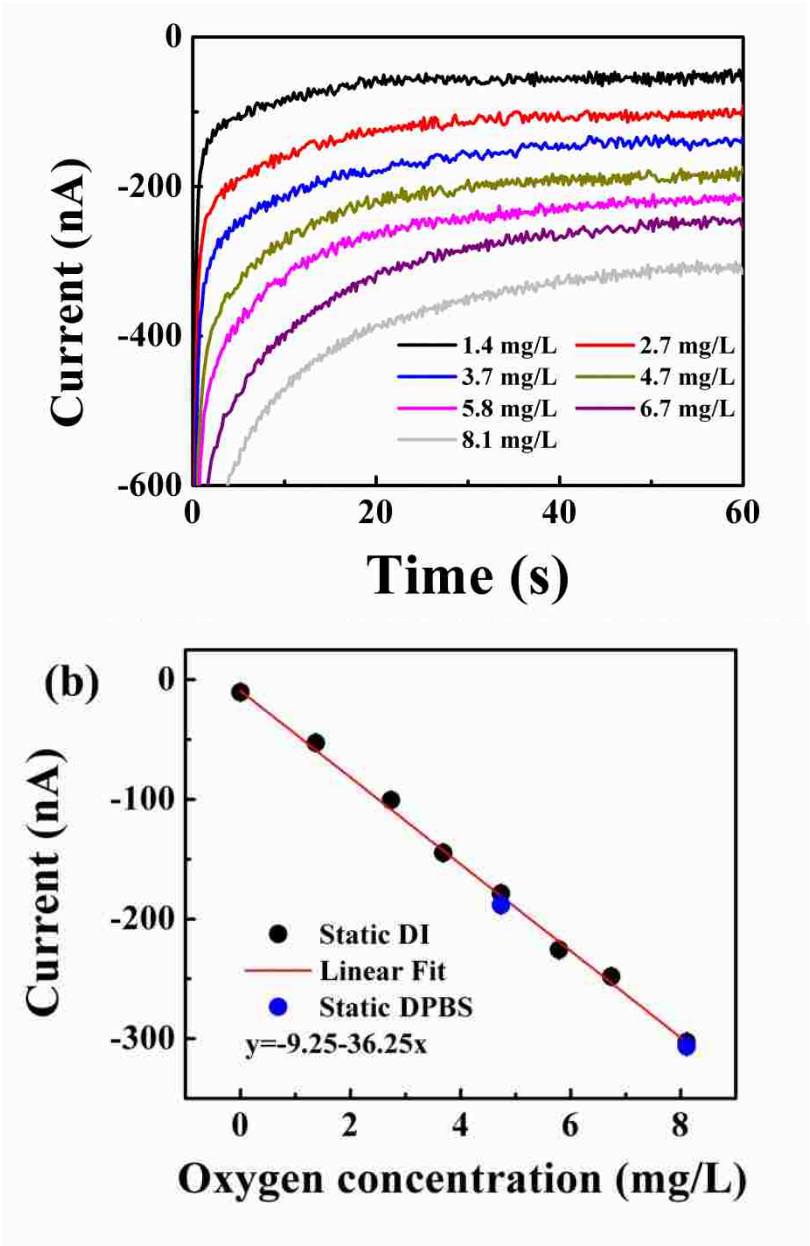

Figure 5.7: CA curves (a) of the DI water with different oxygen concentration under static condition, and calibration curve (b) obtained using the results of CA. The Current values in the CA curves of DPBS were shown in the calibration curve for comparison. (Reported oxygen concentrations determined by hand held oxygen meter Milwaukee MW600).

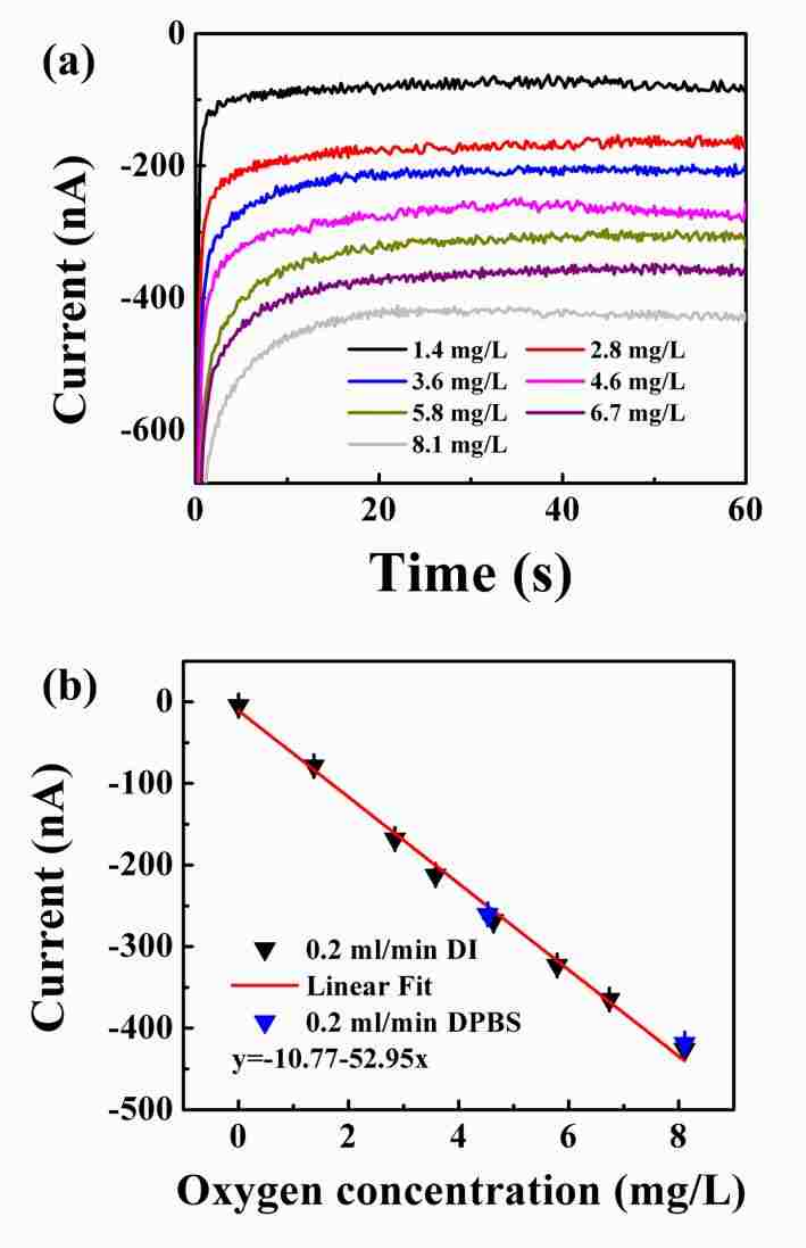

Figure 5.8: CA curves (a) of the DI water with different oxygen concentration under flow 0.2 ml/min, and calibration curve (b) obtained using the results of CA. The Current values in the CA curves of DPBS were shown in the calibration curve for comparison.

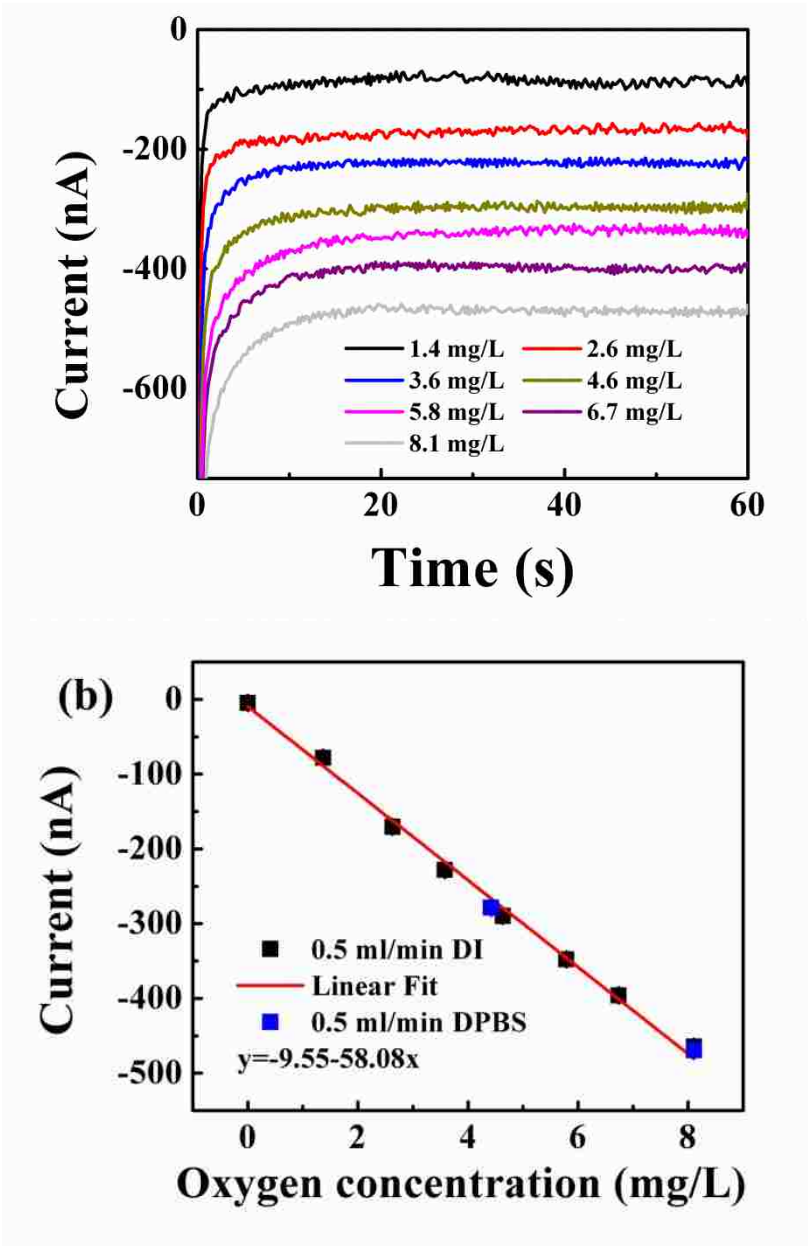

Figure 5.9: CA curves (a) of the DI water with different oxygen concentration under flow 0.5 ml/min, and calibration curve (b) obtained using the results of CA. The Current values in the CA curves of DPBS were shown in the calibration curve for comparison.

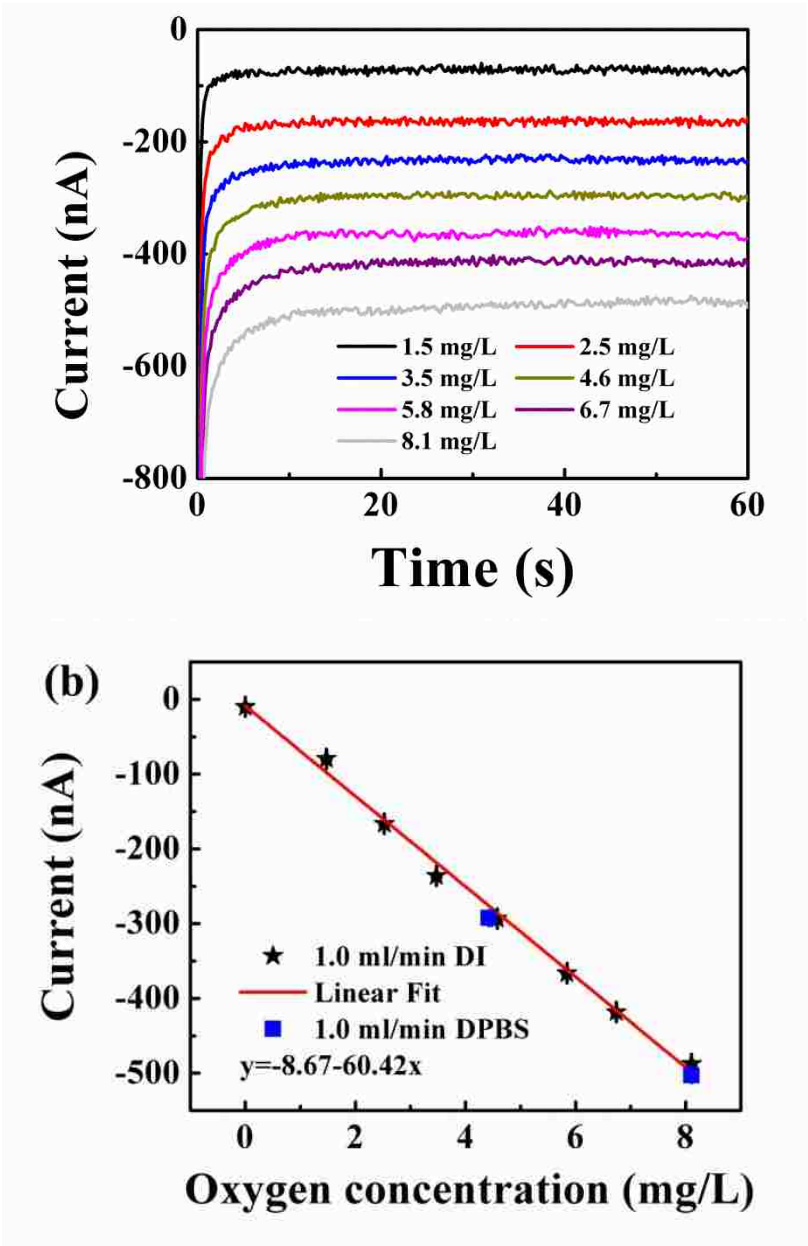

Figure 5.10: CA curves (a) of the DI water with different oxygen concentration under flow 1.0 ml/min, and calibration curve (b) obtained using the results of CA. The Current values in the CA curves of DPBS were shown in the calibration curve for comparison.

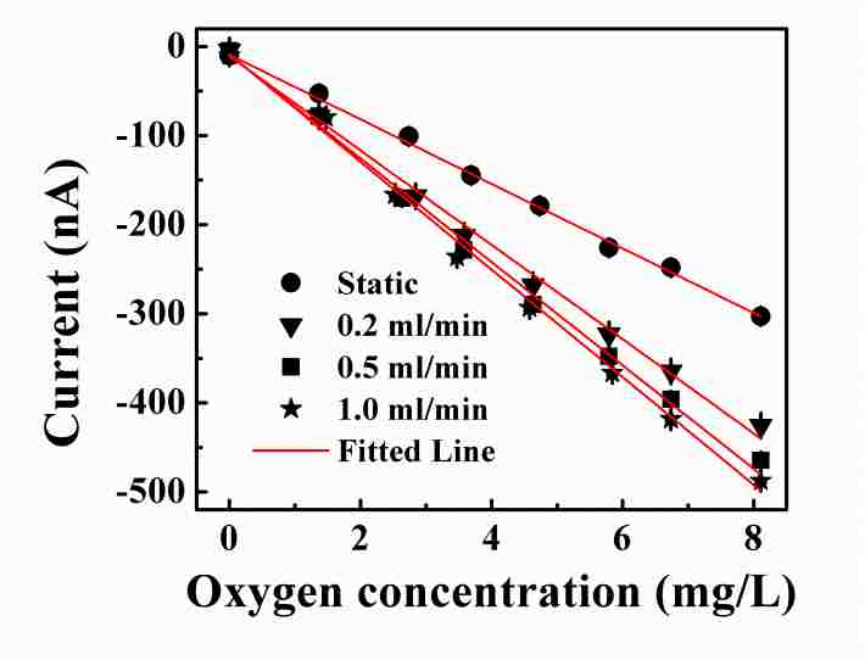

Figure 5.11: Calibration curves obtained from the results of chronoamperometry of DI water with different dissolved oxygen under flow rate 0.0, .02, 0.5, 1.0 mL/min.

Table 5 - 1: Slop coefficients and residual currents of the linear fitted calibration curves under different flow rates.

Flow rate (mL/min)	0.0 (n=6)	0.2 (n=6)	0.5 (n=6)	1.0 (n=6)
Slope coefficient (nA/(mg/L)) (mean ± SE)	-36.25±0.31	-52.95±0.26	-58.08±0.30	-60.42±0.25
Residual current (nA) (mean ± SE)	-9.25±1.22	-10.78±1.07	-9.56±1.20	-8.68±1.10

5.4.6 Response time

The response time of the LTCC based Clark type oxygen sensor was measured using chronoamperometry at -0.75 V through injection of 0.1 M sodium sulfite. A 90%

response time was defined as the time for the current decreased 90% of the value measured at oxygen saturated state when the sensor changed from oxygen saturated state to oxygen depleted state. The Figure 5.12 shows the current change when 0.1 M sodium sulfite was pipetted into the air-filled channel. 0.1 M sodium sulfite solution was used in order to effectively remove oxygen around the sensitive area of working electrode. The current measured in air-filled channel was -692.6±2.1 nA (mean ± SD), which was much higher than that measured when the channel was filled with oxygen saturated DI water or DPBS. This was due to higher solubility of oxygen in Nafion than that of water. The solubility of oxygen in Nafion is 159.4 mg/l[219], almost twenty times of that in water. The current values stayed constant when air filled the channel in the sensor, which indicated that a balance reached between the diffusion of oxygen from air to working electrode and the reaction of oxygen at working electrode. When the 0.1 M sodium sulfite was injected into the channel, the current value decreased to -6.6 ± 1.4 nA (mean ± SD). The measured response time was 10.9 ± 0.6 s (mean ± SEM, n=7). The diffusion time for the dissolved oxygen through the membrane can be estimated by square of membrane thickness (t) divided by diffusion coefficient of oxygen in the membrane (D)[142]. For the oxygen transport from testing solution, it diffused through PDMS oxygen permeable membrane and Nafion electrolyte. Since the diffusion coefficient of PDMS (3.55×10^{-5} cm^2/s) was much higher than that of Nafion electrolyte (0.4×10^{-6} cm^2/s)[219, 220], and the thickness of PDMS was in the same scale with that of Nafion electrolyte, the diffusion time of oxygen through PDMS was negligible. The response time of the developed oxygen sensor can be estimated by the diffusion time of oxygen through Nafion electrolyte. After considering

30 % maximum swell of Nafion electrolyte saturated with water[217], the calculated diffusion time is 5.6 s, which is similar to the response time obtained experimentally.

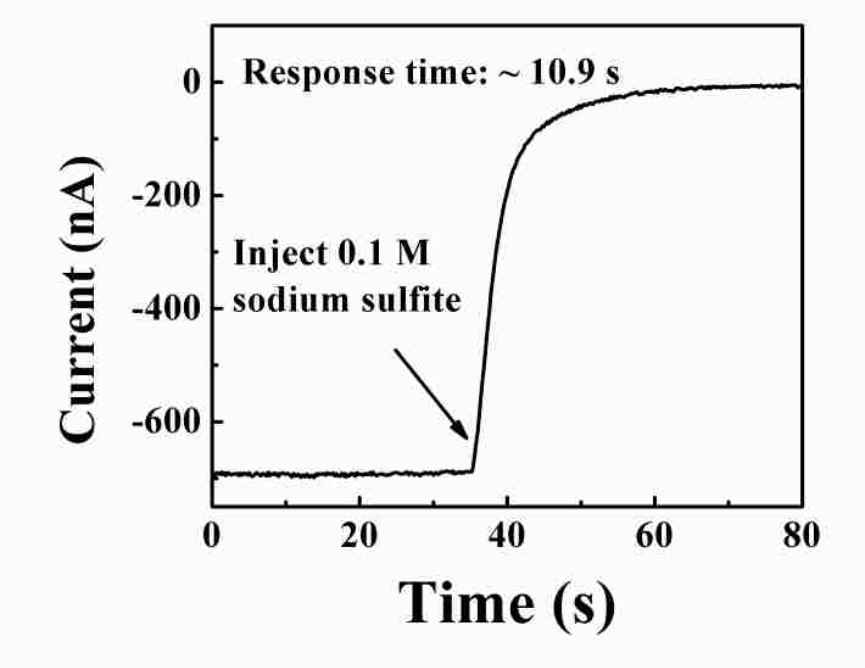

Figure 5.12: Response curve of Clark-type oxygen sensor were tested by injection of the zero -oxygen solution, 0.1 M sodium sulfite.

5.4.7 Lifetime and stability of the sensor

The Ag/AgCl electrode has been extensively used as reference electrode in the microelectronic circuit application due to its stable potential, low dependence on temperature and independence on pH value of the electrolyte[39]. However, the dissolution of AgCl was a big issue, which results in limited lifetime of Clark-type oxygen sensor[40, 131]. One common used method to slow down the dissolution of AgCl was through coating of a gel or polymer materials[221, 222]. Nafion coating has been used to slow down the degradation of Ag/AgCl reference electrode and improve the stability for long time implantation[223]. Solid state Nafion used as electrolyte instead of the liquid electrolyte in

the oxygen sensor also acted as a diffusion layer for AgCl and extend the lifetime of the the Ag/AgCl reference electrode. And the hydrophobic PDMS membrane was a barrier layer which prevents further dissolution of AgCl to the sample solution. A relatively constant concentration of chloride ions will be formed gradually at around Ag/AgCl electrode[221], which will eventually extended the lifetime of Ag/AgCl electrode.

Before the first usage of the oxygen sensor, the Nafion membrane needed to be hydrated with water. PDMS was not permeable to liquid water but water gas. If the oxygen sensor was stored in dry environment, and the Nafion membrane will be dried gradually and be completely dried eventually. Rehydration was needed for next experiment. To prevent the dehydration of water in Nafion, and the LTCC substrate was stored in water for further usage. Figure 5.13 shows the chronoamperometry results tested in DI water before and after the oxygen sensor stored in DI water for eight day. Mismatch was observed in chronoamperometry curves of the dissolved oxygen sensors tested for 16 s, and the current value was higher after the sensor was stored for 8 days. However, the current values in chronoamperometry curves matched well with that of the fresh sensor after 16 s, which indicates the sensor can be used to measure the dissolved oxygen concentration at least for 8 days without rehydration.

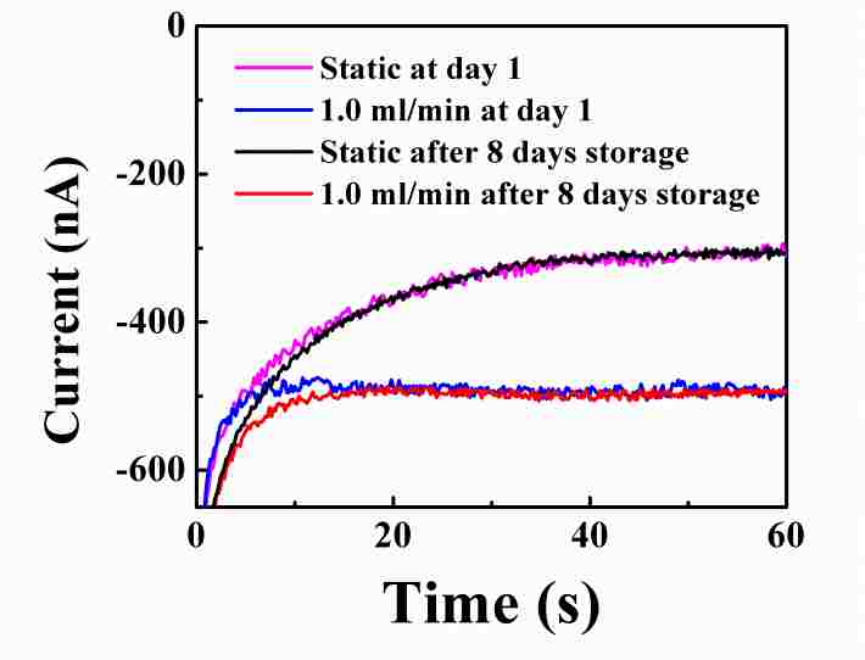

Figure 5.13: Chronoamperometry of the oxygen saturated DI water under static condition and flow rate 1.0 ml/min tested using developed oxygen sensor before and after the sensor stored in DI water for eight days

The properties of the other Clark-type oxygen sensor are summarized in Table 5-1. The LTCC based microfluidic oxygen sensor developed in this work provided comparable response time and residual current compared with the other Clark-type oxygen sensors. In addition, a solid state Nafion electrolyte and PDMS gas permeable membrane were integrated in LTCC package. Microfluidic function was realized in Clark-type oxygen sensor with the capability of real-time monitoring of the dissolved oxygen, which also reduces the effects of the consumption of the localized dissolved oxygen at the sensitive area of working electrode. In addition, it offered rapid and inexpensive fabrication and a more flexible platform for detecting dissolved oxygen.

Table 5 - 1: Comparison of the properties of LTCC based microfluidic Clark-type oxygen sensor and other Clark-type oxygen sensor. PP: Polypropylene; FEP: Fluorinated ethylene propylene.

Response time (s)	Residual current	Electrolyte	OPM membrane	Type of geometry	Testing Method	Reference
10.9	<3.5%	Nafion	PDMS	Planar	Flowing	This work
6.8	~18%	Liquid	PDMS	Planar	Dipping	40
13.4	~1.0%	Liquid	PDMS	Planar	Dipping	39
4.9	~2%	Liquid	PDMS PP FEP	Planer	Dipping	43
9.4	~1.3%	Liquid	PDMS	Planer	Dipping	142
20	0.7%	Liquid	Silicone Rubber	Microprobe	Dipping	143
20-50	-	Liquid	Silicone Rubber	Microprobe	Dipping	41
-	~3%	Nafion	PTFE	Microprobe	Dipping	98
-	40%	Nafion	No Membrane	Microprobe	Dipping	44

5.5 Conclusion

This work describes design, fabrication and characterization of a microfluidic LTCC based Clark-type oxygen sensor. Precise oxygen determination and real-time detection of dissolved oxygen was realized in this integrated microfluidic devices. The devices were characterized by using cyclic voltammetry and chronoamperometry measurement in both DI water and DPBS, and no effects of ions in the testing sample on the results was observed. The calibration curves of the oxygen sensor shows good linearity with correlation coefficient higher than 99.5% for flow rates 0.0, 0.2, 0.5, 1.0 mL/min. The 90% response time of the developed oxygen sensor was 10.9 s. The fast response of the oxygen sensor is beneficial to monitor variation of the oxygen concentration in the biological samples. The usage of the solid-state electrolyte extended

the lifetime of the oxygen sensor and realized the microfluidic function in the Clark-type oxygen sensor. The amperomatric performance of the developed oxygen sensor is comparable to the sensors described in the literature, with rapid and inexpensive fabrication and a more flexible platform for detecting of dissolved oxygen. The developed oxygen sensor can be applied in long term measurement and monitoring of the local oxygen concentration in biological applications, which include cell culturing in a microfluidic configuration, real-time detection of dissolved oxygen in biological fluids.

Chapter 6 Summary and future work

6.1 Summary

This section summarizes the research work present in this thesis, which includes the development of low temperature co-fired ceramic and biocompatibility evaluation of produced materials corresponding to the contents in chapter 3 and 4, and the design, fabrication and characterization of LTCC based Clark-type oxygen sensor corresponding to the work present in chapter 5.

6.1.1 Development of a biocompatible low temperature co-fired ceramic substrate using a commercially available soda-lime-silicate glass and Al_2O_3 ceramic filler

Commercial LTCC systems are not designed for biomedical applications, and have unknown biocompatibility. In the current work an LTCC tape has been developed starting with materials of known composition and biocompatibility, specifically a commercially available soda-lime-silicate glass and alumina. The main components of the glass are CaO, Na_2O, K_2O, Al_2O_3, and SiO_2. The formulation of the LTCC is 46 wt% glass and 54 wt% alumina ceramic. The organic additives used to bind the ceramic particles in green tapes can be burnt out at temperature lower than 500 ^{O}C. Tapes achieve high density for sintering temperatures compatible with LTCC processing ($850<T<1000^{O}C$). A second crystalline phase, anorthite $CaAl_2Si_2O_8$, nucleated as sintering temperature reaches 900^{O}C. The LTCC also exhibits low dielectric constant (K = 9.3) and dielectric loss (tan d < 0.005). A commercial gold electrode paste has also been co-fired with the LTCC, with no delamination, cracks nor camber observed. *In-vitro*

biocompatibility was subsequently evaluated using human umbilical vein endothelial cells (HUVECs). HUVECs are observed to attach and spread on fibronectin coated LTCC substrates, and also in the leachate obtained by soaking LTCC in cell media for seven days. These results establish that the developed LTCC material is biocompatible and suitable for *in-vitro* applications utilizing live cells.

6.1.2 Sintering behavior and biocompatibility of a low temperature co-fired ceramic developed using an experimentally fabricated calcium alumina borosilicate glass and Al_2O_3 ceramic filler

A lime-borosilicate (LBS) glass-alumina low temperature co-fired ceramic (LTCC) has been formulated and evaluated for use *in-vitro* microfluidic sensors and cell culture experiments. The advantage of this formulation is lack of sodium. The release of sodium gives rise to an increase in pH and in osmotic pressure in its vicinity, which will influence the viability of living cells and microorganisms[147]. In aqueous environment, the release rate of sodium in glass is much higher than other elements, including calcium, aluminum and strontium, almost ten times of that for calcium[224, 225].

The sintering behavior was studied using master sintering curve (MSC) theory. The apparent activation energy of the sintering for viscous flow was ~ 452.4 kJ/mol obtained from the MSC results. The sintering and microstructure of the LTCC during firing was studied using differential thermal analysis (DTA), X-ray diffraction (XRD), scanning electron microscopy (SEM) and energy-dispersive X-ray spectrometry (EDS). Using a 75/25 vol % glass to alumina ratio, high density, with no secondary phase, was achieved for sintering temperatures < 900^{O}C. The organic additives added to the green tapes can be

burnt out at temperature lower than 630 ^{O}C obtained from the DTA results. The fabricated LTCC exhibited full densification. Commercial gold and silver electrode pastes were co-fired with the LTCC, and no reaction with the electrode was observed. The resulting LTCC demonstrated dielectric properties with dielectric constant, 9.2, and dielectric loss, 0.12%, at the frequency 1.5 MHz. *In-vitro* biocompatibility of LTCC was evaluated using human umbilical vein endothelial cells (HUVECs). The cell density cultured in leachate medium obtained by soaking LTCC in cell medium for five days was statistically equivalent to that of control. The HUVECs also attached on fibronectin coated LTCC after 14 hr and proliferated after 74 hr. On the basis of these results the current LTCC formulation is viable candidate for the continued development of LTCC based microfluidic biosensors.

6.1.4 A microfluidic LTCC based Clark-type oxygen sensor for real-time oxygen sensing

A microfluidic platform for real-time monitoring of dissolved oxygen was designed and developed in a flowing microfluidic environment fabricated using LTCC technology. The fabricated Clark-type oxygen sensor consisted of three electrodes (working electrode, counter electrode and Ag/AgCl reference electrode), a solid-state proton conductive matrix (Nafion 117 membrane) and polydimethylsiloxane (PDMS) as the oxygen permeable membrane. The usage of a solid-state proton conductive matrix as the electrolyte in the design of the oxygen sensor makes it feasible to integrate this device in a typical LTCC fabrication process. Cyclic voltammetry and chronoamperometry measurement were used to characterize electrochemical properties of the developed oxygen sensor. The reduced current was linearly related with the dissolved oxygen

concentration ranging from 0-8.1 mg/L under different flow conditions (0.0-1 mL/min). The residual currents of the oxygen sensor were less than 3.5% of that measured in oxygen saturated state, and the average response time was 10.9 s. The current device represents an improved Clark-type oxygen sensor with the advantages of easy fabrication, flexible configuration, fast response time, incorporation of microfluidic analyte introduction and real-time detection of dissolved oxygen. The potential applications include material synthesis, cell culture, biological assays incorporating controlled introduction of reagents or analytes and real-time monitoring of dissolved oxygen in a microfluidic environment.

7.2 Future work

The work described in this thesis includes the development of biocompatible LTCC materials and fabrication of LTCC based Clark-type oxygen sensor. In addition to the research covered in this thesis, more efforts to this research are to be done. Some suggestions for further work are listed:

1. The peak sintering temperature of the LTCC material made using 75 vol% calcium alumina borosilicate glass and 25 vol% Al_2O_3 ceramic filler described in chapter 4 is 825 ^{O}C. There is a need to make the peak sintering temperature in the range of 850 – 875^{O}C, because the sintering temperatures of most commercial available electrode paste are in this range. The sintering temperature of the LTCC can be adjusted by varying the ratio of the glass and ceramic phase. To make the sintering temperature higher, more ceramic filler can be added.

2. The permanent bonding the LTCC based Clark-type oxygen sensor as a whole chip is needed. Binder clips are used to bond all elements together. A method to bond all elements together is needed to be investigated, so the penetration of oxygen from the outside environment can be limited. Oxygen plasma can be used to treat the surface of PDMS membrane and PDMS channel, and irreversible bonding between them can be achieved by pressing treated surface against each other.
3. There is a need to miniaturization of the LTCC based Clark-type oxygen sensor. The optimum distance of the working, counter and reference electrode should be investigated, so the crosstalk between three electrodes can be limited and further miniaturization of the sensor is realized.
4. The effects of the thickness of solid state electrolyte on the properties of the Clark-type oxygen sensor should be studied. A better understanding how the electrochemical properties of the sensor change with thickness of the electrolyte can improve the reproducibility. Response time can be shortened by reducing the thickness of the electrolyte.
5. The effects of the surface area of working electrode on the electrochemical properties of sensors should be also investigated. The measured reduced current increases with the increase of surface area in working electrode, and detailed studies would be useful.

Reference

1 P. Yager, T. Edwards, E. Fu, K. Helton, K. Nelson, M. R. Tam, and B. H. Weigl, "Microfluidic diagnostic technologies for global public health," *Nature,* 442 412-418 (2006).

2 G. M. Whitesides, "The origins and the future of microfluidics," *Nature,* 442 368-373 (2006).

3 Q. F. Xue, F. Foret, Y. M. Dunayevskiy, P. M. Zavracky, N. E. McGruer, and B. L. Karger, "Multichannel microchip electrospray mass spectrometry," *Analytical Chemistry,* 69 426-430 (1997).

4 P. S. Dittrich and A. Manz, "Lab-on-a-chip: microfluidics in drug discovery," *Nature Reviews Drug Discovery,* 5 210-218 (2006).

5 A. R. Wheeler, W. R. Throndset, R. J. Whelan, A. M. Leach, R. N. Zare, Y. H. Liao, K. Farrell, I. D. Manger, and A. Daridon, "Microfluidic device for single-cell analysis," *Analytical Chemistry,* 75 3581-3586 (2003).

6 P. S. Dittrich and A. Manz, "Single-molecule fluorescence detection in microfluidic channels - the Holy Grail in mu TAS?," *Analytical and Bioanalytical Chemistry,* 382 1771-1782 (2005).

7 S. K. Sia and G. M. Whitesides, "Microfluidic devices fabricated in poly(dimethylsiloxane) for biological studies," *Electrophoresis,* 24 3563-3576 (2003).

8 B. G. Chung, L. A. Flanagan, S. W. Rhee, P. H. Schwartz, A. P. Lee, E. S. Monuki, and N. L. Jeon, "Human neural stem cell growth and differentiation in a gradient-generating microfluidic device," *Lab on a Chip,* 5 401-406 (2005).

9 Z. Du, N. Colls, K. H. Cheng, M. W. Vaughn, and L. Gollahon, "Microfluidic-based diagnostics for cervical cancer cells," *Biosensors & Bioelectronics,* 21 1991-1995 (2006).

10 E. P. Kartalov, J. F. Zhong, A. Scherer, S. R. Quake, C. R. Taylor, and W. F. Anderson, "High-throughput multi-antigen microfluidic fluorescence immunoassays," *Biotechniques,* 40 85-90 (2006).

11 A. Bhattacharyya and C. A. Klapperich, "Microfluidics-based extraction of viral RNA from infected mammalian cells for disposable molecular diagnostics," *Sensors and Actuators B-Chemical,* 129 693-698 (2008).

12 A. Obubuafo, S. Balamurugan, H. Shadpour, D. Spivak, R. L. McCarley, and S. A. Soper, "Poly(methyl methacrylate) microchip affinity capillary gel electrophoresis of aptamer-protein complexes for the analysis of thrombin in plasma," *Electrophoresis,* 29 3436-3445 (2008).

13 K. S. Lee, S. H. Park, S. Y. Won, and Y. B. Shim, "Electrophoretic total analysis of trace tetracycline antibiotics in a microchip with amperometry," *Electrophoresis,* 30 3219-3227 (2009).

14 C. L. Walsh, B. M. Babin, R. W. Kasinskas, J. A. Foster, M. J. McGarry, and N. S. Forbes, "A multipurpose microfluidic device designed to mimic microenvironment gradients and develop targeted cancer therapeutics," *Lab on a Chip,* 9 545-554 (2009).

15 P. S. Doyle, J. Bibette, A. Bancaud, and J. L. Viovy, "Self-assembled magnetic matrices for DNA separation chips," *Science,* 295 2237-2237 (2002).

16 C. S. Martinez-Cisneros, N. Ibanez-Garcia, F. Valdes, and J. Alonso, "Miniaturized total analysis systems: Integration of electronics and fluidics using low-temperature co-fired ceramics," *Analytical Chemistry,* 79 8376-8380 (2007).

17 M. Gongora-Rubio, L. M. Sola-Laguna, P. J. Moffett, and J. J. Santiago-Aviles, "The utilization of low temperature co-fired ceramics (LTCC-ML) technology for meso-scale EMS, a simple thermistor based flow sensor," *Sensors and Actuators a-Physical,* 73 215-221 (1999).

18 C. S. Martinez-Cisneros, Z. da Rocha, M. Ferreira, F. Valdes, A. Seabra, M. Gongora-Rubio, and J. Alonso-Chamarro, "A Monolithic Continuous-Flow Microanalyzer with Amperometric Detection Based on the Green Tape Technology," *Analytical Chemistry,* 81 7448-7453 (2009).

19 L. J. Golonka, T. Zawada, J. Radojewski, H. Roguszczak, and M. Stefanow, "LTCC microfluidic system," *International Journal of Applied Ceramic Technology,* 3 150-156 (2006).

20 L. J. Golonka, H. Roguszczak, T. Zawada, J. Radojewski, I. Grabowska, M. Chudy, A. Dybko, Z. Brzozka, and D. Stadnik, "LTCC based microfluidic system with optical detection," *Sensors and Actuators B-Chemical,* 111 396-402 (2005).

21 K. Malecha, D. G. Pijanowska, L. J. Golonka, and P. Kurek, "Low temperature co-fired ceramic (LTCC)-based biosensor for continuous glucose monitoring," *Sensors and Actuators B-Chemical,* 155 923-929 (2011).

22 K. Malecha, D. G. Pijanowska, L. J. Golonka, and W. Torbicz, "LTCC microreactor for urea determination in biological fluids," *Sensors and Actuators B-Chemical,* 141 301-308 (2009).

23 E. S. Fakunle, Z. P. Aguilar, J. L. Shultz, A. D. Toland, and I. Fritsch, "Evaluation of screen-printed gold on low-temperature co-fired ceramic as a substrate for the immobilization of electrochemical immunoassays," *Langmuir,* 22 10844-10853 (2006).

24 M. Goldbacha, H. Axthelm, and M. Keusgen, "LTCC-based microchips for the electrochemical detection of phenolic compounds," *Sensors and Actuators B-Chemical,* 120 346-351 (2006).

25 X. Llopis, N. Ibanez-Garcia, S. Alegret, and J. Alonso, "Pesticide determination by enzymatic inhibition and amperometric detection in a low-temperature cofired ceramics microsystem," *Analytical Chemistry,* 79 3662-3666 (2007).

26 M. R. Gongora-Rubio, M. B. A. Fontes, Z. M. da Rocha, E. M. Richter, and L. Angnes, "LTCC manifold for heavy metal detection system in biomedical and environmental fluids," *Sensors and Actuators B-Chemical,* 103 468-473 (2004).

27 N. Ibanez-Garcia, R. D. M. Goncalves, Z. M. da Rocha, M. R. Gongora-Rubio, A. C. Seabra, and J. A. Chamarro, "LTCC meso-analytical system for chloride ion determination in drinking waters," *Sensors and Actuators B-Chemical,* 118 67-72 (2006).

28 R. Alves-Segundo, N. Ibanez-Garcia, M. Baeza, M. Puyol, and J. Alonso-Chamarro, "Towards a monolithically integrated microsystem based on the green tape ceramics technology for spectrophotometric measurements. Determination of chromium (VI) in water," *Microchimica Acta,* 172 225-232 (2011).

29 R. Olive-Monllau, C. S. Martinez-Cisneros, J. Bartroli, M. Baeza, and F. Cespedes, "Integration of a sensitive carbon nanotube composite electrode in a ceramic microanalyzer for the amperometric determination of free chlorine," *Sensors and Actuators B-Chemical,* 151 416-422 (2011).

30 N. Ibanez-Garcia, M. Baeza, M. Puyol, R. Gomez, M. Batlle, and J. Alonso-Chamarro, "Biparametric Potentiometric Analytical Microsystem Based on the Green Tape Technology," *Electroanalysis,* 22 2376-2382 (2010).

31 S. A. A. Almeida, E. Arasa, M. Puyol, C. S. Martinez-Cisneros, J. Alonso-Chamarro, M. C. B. S. M. Montenegro, and M. G. F. Sales, "Novel LTCC-potentiometric microfluidic device for biparametric analysis of organic compounds carrying plastic antibodies as ionophores: Application to sulfamethoxazole and trimethoprim," *Biosensors & Bioelectronics,* 30 197-203 (2011).

32 P. Bembnowicz, M. Malodobra, W. Kubicki, P. Szczepanska, A. Gorecka-Drzazga, J. Dziuban, A. Jonkisz, A. Karpiewska, T. Dobosz, and L. Golonka, "Preliminary studies on LTCC based PCR microreactor," *Sensors and Actuators B-Chemical,* 150 715-721 (2010).

33 D. J. Sadler, R. Changrani, P. Roberts, C. F. Chou, and F. Zenhausern, "Thermal management of BioMEMS: Temperature control for ceramic-based PCR and DNA detection devices," *Ieee Transactions on Components and Packaging Technologies,* 26 309-316 (2003).

34 P. Bembnowicz, P. Herbut, M. Malodobra, A. Karpiewska, L. J. Golonka, A. Jonkisz, and T. Dobosz, "The low temperature co-fired ceramics (LTCC) chip for polymerase chain reaction (PCR) application," *Optica Applicata,* 41 471-480 (2011).

35 S. N. Brahmasandra, V. M. Ugaz, D. T. Burke, C. H. Mastrangelo, and M. A. Burns, "Electrophoresis in microfabricated devices using photopolymerized polyacrylamide gels and electrode-defined sample injection," *Electrophoresis,* 22 300-311 (2001).

36 W. K. Jones, Y. Liu, B. Larsen, P. Wang, and M. Zampino, "Chemical, structural and mechanical properties of the LTCC tapes," *The International Journal of Microcircuits and Electronic Packaging,* 23 5 (2000).

37 W. L. Zhang and R. E. Eitel, "Biostability of Low-Temperature Co-Fired Ceramic Materials for Microfluidic and Biomedical Devices," *International Journal of Applied Ceramic Technology,* 9 60-66 (2012).

38 J. X. Liu, D. Z. Yang, F. Shi, and Y. J. Cai, "Sol-gel deposited TiO2 film on NiTi surgical alloy for biocompatibility improvement," *Thin Solid Films,* 429 225-230 (2003).

39 C. C. Wu, H. N. Luk, Y. T. T. Lin, and C. Y. Yuan, "A Clark-type oxygen chip for in situ estimation of the respiratory activity of adhering cells," *Talanta,* 81 228-234 (2010).

40 C. C. Wu, T. Yasukawa, H. Shiku, and T. Matsue, "Fabrication of miniature Clark oxygen sensor integrated with microstructure," *Sensors and Actuators B-Chemical,* 110 342-349 (2005).

41 H. Suzuki, T. Hirakawa, I. Watanabe, and Y. Kikuchi, "Determination of blood pO(2) using a micromachined Clark-type oxygen electrode," *Analytica Chimica Acta*, 431 249-259 (2001).
42 Y. Cui, J. P. Barford, and R. Renneberg, "Development of an interference-free biosensor for glucose-6-phosphate using a bienzyme-based Clark-type electrode," *Sensors and Actuators B-Chemical*, 123 696-700 (2007).
43 J. Park, Y. K. Pak, and J. J. Pak, "A microfabricated reservoir-type oxygen sensor for measuring the real-time cellular oxygen consumption rate at various conditions," *Sensors and Actuators B-Chemical*, 147 263-269 (2010).
44 P. Wang, Y. Liu, H. D. Abruna, J. A. Spector, and W. L. Olbricht, "Micromachined dissolved oxygen sensor based on solid polymer electrolyte," *Sensors and Actuators B-Chemical*, 153 145-151 (2011).
45 L. J. Golonka, "Technology and applications of Low Temperature Cofired Ceramic (LTCC) based sensors and microsystems," *Bulletin of the polish academy of sciences techinical sciences*, 54 11 (2006).
46 M. R. Gongora-Rubio, P. Espinoza-Vallejos, L. Sola-Laguna, and J. J. Santiago-Aviles, "Overview of low temperature co-fired ceramics tape technology for meso-system technology (MsST)," *Sensors and Actuators a-Physical*, 89 222-241 (2001).
47 Y. Imanaka, *Multilayered Low Temperature Cofired Ceramics (LTCC) Technology*. New York, NY: Springer Science+Business Media Inc., 2005.
48 H. W. Stetson, "Method of making multilayer circuits," US Patent, 1965.
49 W. J. Gyuvk, "Methods for manufacturing multilayered monolithic ceramic bodies," US Patent, 1965.
50 R. R. Tummala, "Ceramic and Glass-Ceramic Packaging in the 1990s," *Journal of the American Ceramic Society*, 74 895-908 (1991).
51 W. L. Zhang, "High Performance Piezoelectric Materials And Devices For Multilayer Low Temperature Co-Fired Ceramic Based Microfluidic Systems," Ph.D, University of Kentucky, 2011.
52 D. M. Materials, "DuPont Green Tape™ Material System Design and Layout Guidelines," E.I. du Pont de Nemours and Company, Wilmington, DE2003.
53 T. Hu, "BST-Based Low Temperature Co-Fired Ceramic (LTCC) Modules for Microwave Tunable Components," Ph.D, University of Oulu, 2002.
54 H. Jantunen, "A Novel Low Temperature Co-Firing Ceramic (LTCC) Material for Telecommunication Devices," Ph.D, University of Oulu, 2001.
55 H. Birol, "Fabrication of Low Temperature Co-fired Ceramic (LTCC)-Based Sensor and Micro-fluidic Structures," Ph.D, Éole Polytechnique Federale De Lausanne (EPFL), 2007.
56 C. R. Chang and J. H. Jean, "Crystallization kinetics and mechanism of low-dielectric, low-temperature, cofirable CaO-B2O3-SiO2 glass-ceramics," *Journal of the American Ceramic Society*, 82 1725-1732 (1999).
57 S. X. H. Dai, R. F. Huang, and D. L. Wilcox, "Use of titanates to achieve a temperature-stable low-temperature cofired ceramic dielectric for wireless applications," *Journal of the American Ceramic Society*, 85 828-832 (2002).

58 C. L. Lo, J. G. Duh, B. S. Chiou, and W. H. Lee, "Low-temperature sintering and microwave dielectric properties of anorthite-based glass-ceramics," *Journal of the American Ceramic Society,* 85 2230-2235 (2002).

59 O. Dernovsek, A. Naeini, G. Preu, W. Wersing, M. Eberstein, and W. A. Schiller, "LTCC glass-ceramic composites for microwave application," *Journal of the European Ceramic Society,* 21 1693-1697 (2001).

60 H. Jantunen, R. Rautioaho, A. Uusimaki, and S. Leppavuori, "Compositions of MgTiO3-CaTiO3 ceramic with two borosilicate glasses for LTCC technology," *Journal of the European Ceramic Society,* 20 2331-2336 (2000).

61 S. J. Bethke, R. A. Miesem, W. W. Chiou, and R. G. Pastor, "Ceramic composition," *United States Patent,* Patent Number: 5821181 (1981).

62 T. Thelemann, H. Thust, and M. Hintz, "Using LTCC for microsystems," *Microelectronics International,* 19 19-23 (2002).

63 K. A. Peterson, K. D. Patel, C. K. Ho, S. B. Rohde, C. D. Nordquist, C. A. Walker, B. D. Wroblewski, and M. Okandan, "Novel microsystem applications with new techniques in low-temperature co-fired ceramics," *International Journal of Applied Ceramic Technology,* 2 345-363 (2005).

64 N. Ibanez-Garcia, C. S. Martinez-Cisneros, F. Valdes, and J. Alonso, "Green-tape ceramics. New technological approach for integrating electronics and fluidics in microsystems," *Trac-Trends in Analytical Chemistry,* 27 24-33 (2008).

65 C. Q. Scrantom and J. C. Lawson, "LTCC technology where we are and where we're going," *Institute of Electrical and Electronics Engineers,* 8 (1999).

66 G. A. Gross, T. Thelemann, S. Schneider, D. Boskovic, and J. M. Kohler, "Fabrication and fluidic characterization of static micromixers made of low temperature cofired ceramic (LTCC)," *Chemical Engineering Science,* 63 2773-2784 (2008).

67 C. F. Chou, R. Changrani, P. Roberts, D. Sadler, J. Burdon, F. Zenhausern, S. Lin, A. Mulholland, N. Swami, and R. Terbrueggen, "A miniaturized cyclic PCR device - modeling and experiments," *Microelectronic Engineering,* 61-2 921-925 (2002).

68 W. Smetana, B. Balluch, G. Stangl, E. Gaubitzer, M. Edetsberger, and G. Kohler, "A multi-sensor biological monitoring module built up in LTCC-technology," *Microelectronic Engineering,* 84 1240-1243 (2007).

69 W. Smetana, B. Balluch, I. Atassi, P. Kügler, E. Gaubitzer, M. Edetsberger, and G. Köhler, "A ceramic microfluidic device for monitoring complex biochemical reactive systems," in *Biomedical engineering systems and technologies,* Porto, Portugal, 2009, pp. 110-123.

70 E. Darko, K. B. Thurbide, G. C. Gerhardt, and J. Michienzi, "Characterization of Low-Temperature Cofired Ceramic Tiles as Platforms for Gas Chromatographic Separations," *Analytical Chemistry,* 85 5376-5381 (2013).

71 P. Ciosek, K. Zawadzki, J. Lopacinska, M. Skolimowski, P. Bembnowicz, L. J. Golonka, Z. Brzozka, and W. Wroblewski, "Monitoring of cell cultures with LTCC microelectrode array," *Analytical and Bioanalytical Chemistry,* 393 2029-2038 (2009).

72 K. Malecha, M. Czok, A. Hetnar, A. Pawlik, H. Sztajer, and L. J. Golonka, "Micro Ceramic Cell Analyzer (MCCA) - Preliminary results," *Microelectronics Reliability*, 51 1250-1252 (2011).
73 S. Kemethmuller, M. Hagymasi, A. Stiegelschmitt, and A. Roosen, "Viscous flow as the driving force for the densification of low-temperature co-fired ceramics," *Journal of the American Ceramic Society*, 90 64-70 (2007).
74 K. G. Ewsuk, "Ceramic-Filled-Glass Composite Sintering," *Ceramic Transaction Materials Processes Microelectronic System*, 15 279-295 (1989).
75 K. G. Ewsuk, L. W. Harrision, and F. J. Walczak, "Sintering Glass-Filled Ceramic Composites; Effects of Glass Properties," *Ceramic Transaction Ceramic Powder Science II*, 1 967-975 (1987).
76 T. A. Ring, *Fundamentals of ceramic powder processing and synthesis*. San Diego: Academic press, 1996.
77 M. N. Rahaman, *Ceramic processing and sintering*, Second ed. Boca Raton, FL: CRC press, 2003.
78 R. M. Cannon and W. C. Carter, "Interplay of Sintering Microstructures, Driving Forces, and Mass-Transport Mechanisms," *Journal of the American Ceramic Society*, 72 1550-1555 (1989).
79 W. D. Kingery, K. H. Bowen, and D. R. Uhlmann, *Introduction to ceramics*, Second Edition ed. New York: A Wiley-Interscience Publication, 1976.
80 A. W. Adamson, *Physical chemistry of surfaces*, Six ed. New York: John Wiley & Sons, 1997.
81 R. M. German, *Liquid phase sintering*. New York: Plenum Press, 1985.
82 W. D. Kingery, "Densification during Sintering in the Presence of a Liquid Phase .1. Theory," *Journal of Applied Physics*, 30 301-306 (1959).
83 W. D. Kingery and M. D. Narasimhan, "Densification during Sintering in the Presence of a Liquid Phase .2. Experimental," *Journal of Applied Physics*, 30 307-310 (1959).
84 R. German, P. Suri, and S. Park, "Review: liquid phase sintering," *Journal of Materials Science*, 44 1-39 (2009).
85 R. M. German and K. S. Churn, "Sintering Atmosphere Effects on the Ductility of W-Ni-Fe Heavy-Metals," *Metallurgical Transactions a-Physical Metallurgy and Materials Science*, 15 747-754 (1984).
86 E. M. Rabinovich, "Preparation of Glass by Sintering," *Journal of Materials Science*, 20 4259-4297 (1985).
87 G. C. Kuczynski, "Study of the Sintering of Glass," *Journal of Applied Physics*, 20 1160-1163 (1949).
88 D. Crowdy, "Viscous sintering of unimodal and bimodal cylindrical packings with shrinking pores," *European Journal of Applied Mathematics*, 14 421-445 (2003).
89 J. Frenkel, "Viscous Flow of Crystalline Bodies," *Zhurnal Eksperimentalnoi I Teoreticheskoi Fiziki*, 16 29-38 (1946).
90 G. W. Scherer, "Sintering of Low-Density Glasses .1. Theory," *Journal of the American Ceramic Society*, 60 236-239 (1977).

91 G. W. Scherer and D. L. Bachman, "Sintering of Low-Density Glasses .2. Experimental-Study," *Journal of the American Ceramic Society,* 60 239-243 (1977).
92 J. K. Mackenzie and R. Shuttleworth, "A Phenomenological Theory of Sintering," *Proceedings of the Physical Society. Section B,* 62 833-852 (1949).
93 R. I. Dmitriev and D. B. Papkovsky, "Optical probes and techniques for O-2 measurement in live cells and tissue," *Cellular and Molecular Life Sciences,* 69 2025-2039 (2012).
94 K. Kellner, G. Liebsch, I. Klimant, O. S. Wolfbeis, T. Blunk, M. B. Schulz, and A. Gopferich, "Determination of oxygen gradients in engineered tissue using a fluorescent sensor," *Biotechnology and Bioengineering,* 80 73-83 (2002).
95 Z. Rosenzweig and R. Kopelman, "Development of a Submicrometer Optical-Fiber Oxygen Sensor," *Analytical Chemistry,* 67 2650-2654 (1995).
96 H. Suzuki, A. Sugama, and N. Kojima, "Micromachined Clark Oxygen Electrodes and Biosensors," *Fujitsu Scientific & Technical Journal,* 28 393-401 (1992).
97 Z. Yang, S. Sasaki, I. Karube, and H. Suzuki, "Fabrication of oxygen electrode arrays and their incorporation into sensors for measuring biochemical oxygen demand," *Analytica Chimica Acta,* 357 41-49 (1997).
98 G. W. McLaughlin, K. Braden, B. Franc, and G. T. A. Kovacs, "Microfabricated solid-state dissolved oxygen sensor," *Sensors and Actuators B-Chemical,* 83 138-148 (2002).
99 X. W. Wang, H. Suzuki, T. Hachiya, T. Kaneko, and K. Sunagawa, "Microfabricated Needle-Type Sensors for pO2, pCO2, and pH," *IEEE sensors journal,* 6 8 (2006).
100 J. N. Demas, B. A. DeGraff, and P. B. Coleman, "Oxygen sensors based on luminescence quenching," *Analytical Chemistry,* 71 793a-800a (1999).
101 A. P. Vollmer, R. F. Probstein, R. Gilbert, and T. Thorsen, "Development of an integrated microfluidic platform for dynamic oxygen sensing and delivery in a flowing medium," *Lab on a Chip,* 5 1059-1066 (2005).
102 M. E. Lippitsch, J. Pusterhofer, M. J. P. Leiner, and O. S. Wolfbeis, "Fibre-Optic Oxygen Sensor with the Fluorescence Decay Time as the Information Carrier," *Analytica Chimica Acta,* 205 1-6 (1988).
103 C. Preininger, I. Klimant, and O. S. Wolfbeis, "Optical-Fiber Sensor for Biological Oxygen-Demand," *Analytical Chemistry,* 66 1841-1846 (1994).
104 S. M. Grist, L. Chrostowski, and K. C. Cheung, "Optical Oxygen Sensors for Applications in Microfluidic Cell Culture," *Sensors,* 10 9286-9316 (2010).
105 P. Hartmann, W. Ziegler, G. Holst, and D. W. Lubbers, "Oxygen flux fluorescence lifetime imaging," *Sensors and Actuators B-Chemical,* 38 110-115 (1997).
106 S. H. Huang, Y. H. Hsu, C. W. Wu, and C. J. Wu, "Light-addressable measurements of cellular oxygen consumption rates in microwell arrays based on phase-based phosphorescence lifetime detection," *Biomicrofluidics,* 6 (2012).
107 T. C. O'Riordan, D. Buckley, V. Ogurtsov, R. O'Connor, and D. B. Papkovsky, "A cell viability assay based on monitoring respiration by optical oxygen sensing," *Analytical Biochemistry,* 278 221-227 (2000).

108 A. V. Kondrashina, D. B. Papkovsky, and R. I. Dmitriev, "Measurement of cell respiration and oxygenation in standard multichannel biochips using phosphorescent O-2-sensitive probes," *Analyst,* 138 4915-4921 (2013).
109 R. H. W. Lam, M. C. Kim, and T. Thorsen, "Culturing Aerobic and Anaerobic Bacteria and Mammalian Cells with a Microfluidic Differential Oxygenator," *Analytical Chemistry,* 81 5918-5924 (2009).
110 T. W. Molter, S. C. McQuaide, M. T. Suchorolski, T. J. Strovas, L. W. Burgess, D. R. Meldrum, and M. E. Lidstrom, "A microwell array device capable of measuring single-cell oxygen consumption rates," *Sensors and Actuators B-Chemical,* 135 678-686 (2009).
111 J. R. Etzkorn, W. C. Wu, Z. Y. Tian, P. Kim, S. H. Jang, D. R. Meldrum, A. K. Y. Jen, and B. A. Parviz, "Using micro-patterned sensors and cell self-assembly for measuring the oxygen consumption rate of single cells," *Journal of Micromechanics and Microengineering,* 20 (2010).
112 A. Sin, K. C. Chin, M. F. Jamil, Y. Kostov, G. Rao, and M. L. Shuler, "The design and fabrication of three-chamber microscale cell culture analog devices with integrated dissolved oxygen sensors," *Biotechnology Progress,* 20 338-345 (2004).
113 Z. Lin, T. Cherng-Wen, P. Roy, and D. Trau, "In-situ measurement of cellular microenvironments in a microfluidic device," *Lab on a Chip,* 9 257-262 (2009).
114 D. B. Papkovsky, "Methods in optical oxygen sensing: Protocols and critical analyses," *Oxygen Sensing,* 381 715-735 (2004).
115 A. Sharma and O. S. Wolfbeis, "Fiberoptic Oxygen Sensor Based on Fluorescence Quenching and Energy-Transfer," *Applied Spectroscopy,* 42 1009-1011 (1988).
116 D. A. Nivens, M. V. Schiza, and S. M. Angel, "Multilayer sol-gel membranes for optical sensing applications: single layer pH and dual layer CO2 and NH3 sensors," *Talanta,* 58 543-550 (2002).
117 J. Wang, *Analytical Electrochemistry,* Second Edition ed. New York: Wiley-VCH, 2000.
118 A. J. Bard and L. R. Faulkner, *Electrochemical Methods. Fundamentals and Applications,* Second Edition ed. New York: John Wiley & Sons, 2001.
119 G. W. McLaughlin, "Microfluidic and biosensor applications of fluoropolymer films," Ph.D, Electrical Engineering, Stanford University, 2001.
120 G. Eden, G. F. Inbar, I. Timortritsch, and H. I. Bicher, "Miniaturized Electrode for Online Po2 Measurements," *Ieee Transactions on Biomedical Engineering,* Bm22 275-280 (1975).
121 P. R. Warburton, R. S. Sawtelle, A. Watson, and A. Q. Wang, "Failure prediction for a galvanic oxygen sensor," *Sensors and Actuators B-Chemical,* 72 197-203 (2001).
122 H. Suzuki, H. Ozawa, S. Sasaki, and I. Karube, "A novel thin-film Ag/AgCl anode structure for microfabricated Clark-type oxygen electrodes," *Sensors and Actuators B-Chemical,* 53 140-146 (1998).
123 L. C. Clark, "Monitor and Control of Blood and Tissue Oxygen Tensions," *Transactions American Society for Artificial Internal Organs,* 2 41-& (1956).

124 Y. Miyahara, F. Matsu, S. Shiokawa, T. Moriizumi, H. Matsuoka, I. Karube, and S. Suzuki, "Biosensor using anisotropic etching of Si," *Proc. 3rd Sensor Symp.*, 6 (1983).
125 M. Koudelka, "Performance-Characteristics of a Planar Clark-Type Oxygen Sensor," *Sensors and Actuators*, 9 249-258 (1986).
126 H. Suzuki, "Advances in the microfabrication of electrochemical sensors and systems," *Electroanalysis*, 12 703-715 (2000).
127 H. Suzuki, A. Sugama, and N. Kojima, "Miniature Clark-Type Oxygen-Electrode with a 3-Electrode Configuration," *Sensors and Actuators B-Chemical*, 2 297-303 (1990).
128 H. Suzuki, A. Sugama, and N. Kojima, "Effect of Anode Materials on the Characteristics of the Miniature Clark-Type Oxygen-Electrode," *Analytica Chimica Acta*, 233 275-280 (1990).
129 H. Suzuki, N. Kojima, A. Sugama, and F. Takei, "Development of a Miniature Clark-Type Oxygen-Electrode Using Semiconductor Techniques and Its Improvement for Practical Applications," *Sensors and Actuators B-Chemical*, 2 185-191 (1990).
130 H. Suzuki, A. Sugama, and N. Kojima, "Micromachined Clark Oxygen-Electrode," *Sensors and Actuators B-Chemical*, 10 91-98 (1993).
131 H. Suzuki, H. Shiroishi, S. Sasaki, and I. Karube, "Microfabricated liquid junction Ag/AgCl reference electrode and its application to a one-chip potentiometric sensor," *Analytical Chemistry*, 71 5069-5075 (1999).
132 H. Suzuki, H. Arakawa, and I. Karube, "Fabrication of a sensing module using micromachined biosensors," *Biosensors & Bioelectronics*, 16 725-733 (2001).
133 G. Jobst, G. Urban, A. Jachimowicz, F. Kohl, O. Tilado, I. Lettenbichler, and G. Nauer, "Thin-Film Clark-Type Oxygen Sensor-Based on Novel Polymer Membrane Systems for in-Vivo and Biosensor Applications," *Biosensors & Bioelectronics*, 8 123-128 (1993).
134 P. Arquint, M. Koudelkahep, N. F. Derooij, H. Buhler, and W. E. Morf, "Organic Membranes for Miniaturized Electrochemical Sensors - Fabrication of a Combined Po2, Pco2 and Ph Sensor," *Journal of Electroanalytical Chemistry*, 378 177-183 (1994).
135 P. Arquint, A. Vandenberg, B. H. Vanderschoot, N. F. Derooij, H. Buhler, W. E. Morf, and L. F. J. Durselen, "Integrated Blood-Gas Sensor for Po2, Pco2 and Ph," *Sensors and Actuators B-Chemical*, 13 340-344 (1993).
136 H. Suzuki, A. Sugama, N. Kojima, F. Takei, and K. Ikegami, "A Miniature Clark-Type Oxygen-Electrode Using a Polyelectrolyte and Its Application as a Glucose Sensor," *Biosensors & Bioelectronics*, 6 395-400 (1991).
137 K. Tsukada, Y. Miyahara, Y. Shibata, and H. Miyagi, "An Integrated Chemical Sensor with Multiple Ion and Gas Sensors," *Sensors and Actuators B-Chemical*, 2 291-295 (1990).
138 W. Gumbrecht, D. Peters, W. Schelter, W. Erhardt, J. Henke, J. Steil, and U. Sykora, "Integrated Po2, Pco2, Ph Sensor System for Online Blood Monitoring," *Sensors and Actuators B-Chemical*, 19 704-708 (1994).
139 "Micro flow cell for blood gas analysis realizing very small sample volume ".

140 Y. Miyahara, K. Tsukada, and Y. Watanabe, "Long-Life Planar Oxygen Sensor," *Sensors and Actuators B-Chemical,* 20 89-94 (1994).
141 S. Shoji and M. Esashi, "Micro Flow Cell for Blood-Gas Analysis Realizing Very Small Sample Volume," *Sensors and Actuators B-Chemical,* 8 205-208 (1992).
142 J. Park, H. Nam, S. Y. Ahn, Y. K. Pak, and J. J. Pak, "A reservoir-type oxygen sensor with 2 x 3 array for measuring cellular respiration levels," *Sensors and Actuators B-Chemical,* 176 913-920 (2013).
143 H. Suzuki, T. Hirakawa, S. Sasaki, and I. Karube, "An integrated module for sensing pO(2), pCO(2), and pH," *Analytica Chimica Acta,* 405 57-65 (2000).
144 C. Diepart, J. Verrax, P. B. Calderon, O. Feron, B. F. Jordan, and B. Gallez, "Comparison of methods for measuring oxygen consumption in tumor cells in vitro," *Analytical Biochemistry,* 396 250-256 (2010).
145 T. Henning, M. Brischwein, W. Baumann, R. Ehret, I. Freund, R. Kammerer, M. Lehmann, A. Schwinde, and B. Wolf, "Approach to a multiparametric sensor-chip-based tumor chemosensitivity assay," *Anti-Cancer Drugs,* 12 21-32 (2001).
146 E. R. Motrescu, A. M. Otto, M. Brischwein, S. Zahler, and B. Wolf, "Dynamic analysis of metabolic effects of chloroacetaldehyde and cytochalasin B on tumor cells using bioelectronic sensor chips," *Journal of Cancer Research and Clinical Oncology,* 131 683-691 (2005).
147 A. M. Otto, M. Brischwein, A. Niendorf, T. Henning, E. Motrescu, and B. Wolf, "Microphysiological testing for chemosensitivity of living tumor cells with multiparametric microsensor chips," *Cancer Detect Prev,* 27 291-6 (2003).
148 D. von Heimburg, K. Hemmrich, S. Zachariah, H. Staiger, and N. Pallua, "Oxygen consumption in undifferentiated versus differentiated adipogenic mesenchymal precursor cells," *Respiratory Physiology & Neurobiology,* 146 107-116 (2005).
149 G. Sjogren, G. Sletten, and J. E. Dahl, "Cytotoxicity of dental alloys, metals, and ceramics assessed by Millipore filter, agar overlay, and MTT tests," *Journal of Prosthetic Dentistry,* 84 229-236 (2000).
150 A. I. Y. Tok, F. Y. C. Boey, and K. A. Khor, "Tape casting of high dielectric ceramic composite substrates for microelectronics application," *Journal of Materials Processing Technology,* 90 508-512 (1999).
151 I. Zhitomirsky and A. Petric, "Electrophoretic deposition of ceramic materials for fuel cell applications," *Journal of the European Ceramic Society,* 20 2055-2061 (2000).
152 R. E. Mistler and E. R. Twiname, *Tape Casting: Theory and Practice*. Westerville, OH: American Ceramics Society, 2000.
153 Dimarcel.Fv, J. C. Williams, and P. L. Key, "Preferred Orientation in Al2o3 Substrates," *Journal of the American Ceramic Society,* 55 509-& (1972).
154 H. T. Yang and P. Jiang, "Large-Scale Colloidal Self-Assembly by Doctor Blade Coating," *Langmuir,* 26 13173-13182 (2010).
155 M. N. Rahaman, "Ceramic processing and sintering," (2003).
156 Available: http://www.paperandfilm.com/tapecasting.aspx
157 A. Kristoffersson, E. Roncari, and C. Galassi, "Comparison of different binders for water-based tape casting of alumina," *Journal of the European Ceramic Society,* 18 2123-2131 (1998).

158 F. Doreau, G. Tari, C. Pagnoux, T. Chartier, and J. M. F. Ferreira, "Processing of aqueous tape-casting of alumina with acrylic emulsion binders," *Journal of the European Ceramic Society,* 18 311-321 (1998).
159 C. Pagnoux, T. Chartier, M. D. Granja, F. Doreau, J. M. Ferreira, and J. F. Baumard, "Aqueous suspensions for tape-casting based on acrylic binders," *Journal of the European Ceramic Society,* 18 241-247 (1998).
160 Y. T. Chou, Y. T. Ko, and M. F. Yan, "Fluid-Flow Model for Ceramic Tape Casting," *Journal of the American Ceramic Society,* 70 C280-C282 (1987).
161 B. D. Ratner and S. J. Bryant, "Biomaterials: Where we have been and where we are going," *Annual Review of Biomedical Engineering,* 6 41-75 (2004).
162 S. Ozawa and S. Kasugai, "Evaluation of implant materials (hydroxyapatite, glass-ceramics, titanium) in rat bone marrow stromal cell culture," *Biomaterials,* 17 23-29 (1996).
163 S. Deb, R. Mandegaran, and L. Di Silvio, "A porous scaffold for bone tissue engineering/45S5 Bioglass(A (R)) derived porous scaffolds for co-culturing osteoblasts and endothelial cells," *Journal of Materials Science-Materials in Medicine,* 21 893-905 (2010).
164 U. Hersel, C. Dahmen, and H. Kessler, "RGD modified polymers: biomaterials for stimulated cell adhesion and beyond," *Biomaterials,* 24 4385-4415 (2003).
165 C. Piconi, G. Maccauro, F. Muratori, and E. BRACH DEL PREVER, "Alumina and zirconia ceramics in joint replacements," *Journal of applied biomaterials & biomechanics,* 1 14 (2003).
166 C. J. Kirkpatrick, F. Bittinger, M. Wagner, H. Kohler, T. G. van Kooten, C. L. Klein, and M. Otto, "Current trends in biocompatibility testing," *Proceedings of the Institution of Mechanical Engineers Part H-Journal of Engineering in Medicine,* 212 75-84 (1998).
167 S. Rajesh, H. Jantunen, M. Letz, and S. Pichler-Willhelm, "Low Temperature Sintering and Dielectric Properties of Alumina-Filled Glass Composites for LTCC Applications," *International Journal of Applied Ceramic Technology,* 9 52-59 (2012).
168 C. J. D. Kumar, E. K. Sunny, N. Raghu, N. Venkataramani, and A. R. Kulkarni, "Synthesis and characterization of crystallizable anorthite-based glass for a low-temperature cofired ceramic application," *Journal of the American Ceramic Society,* 91 652-655 (2008).
169 M. T. Sebastian and H. Jantunen, "Low loss dielectric materials for LTCC applications: a review," *International Materials Reviews,* 53 57-90 (2008).
170 H. B. de Torres, C. Rensch, M. Fischer, A. Schober, M. Hoffmann, and J. Muller, "Thick film flow sensor for biological microsystems," *Sensors and Actuators a-Physical,* 160 109-115 (2010).
171 A. H. Feingold, M. Heinz, and R. L. Wahlers, "Compliant dielectric and magnetic materials for buried components," *Proceedings of IMAPS Denver,* 4931 6 (2002).
172 D. G. Georgiev, T. Sultana, A. Mian, G. Auner, H. Herfurth, R. Witte, and G. Newaz, "Laser fabrication and characterization of sub-millimeter joints between polyimide and Ti-coated borosilicate glass," *Journal of Materials Science,* 40 5641-5647 (2005).

173 K. S. Parthasarathy, Y. C. N. Cheng, J. P. McAllister, Y. Shen, J. Li, K. Deren, E. M. Haacke, and G. W. Auner, "Biocompatibilities of sapphire and borosilicate glass as cortical neuroprostheses," *Magnetic Resonance Imaging,* 25 1333-1340 (2007).

174 B. Asoo, J. M. McNaney, Y. Mitamura, and R. O. Ritchie, "Cyclic fatigue-crack propagation in sapphire in air and simulated physiological environments," *Journal of Biomedical Materials Research,* 52 488-491 (2000).

175 I. S. Kim, M. Baek, and S. J. Choi, "Comparative Cytotoxicity of Al2O3, CeO2, TiO2 and ZnO Nanoparticles to Human Lung Cells," *Journal of Nanoscience and Nanotechnology,* 10 3453-3458 (2010).

176 R. Muller, R. Meszaros, B. Peplinski, S. Reinsch, M. Eberstein, W. A. Schiller, and J. Deubener, "Dissolution of Alumina, Sintering, and Crystallization in Glass Ceramic Composites for LTCC," *Journal of the American Ceramic Society,* 92 1703-1708 (2009).

177 C. H. Ahn, J. W. Choi, G. Beaucage, J. H. Nevin, J. B. Lee, A. Puntambekar, and J. Y. Lee, "Disposable Smart lab on a chip for point-of-care clinical diagnostics," *Proceedings of the Ieee,* 92 154-173 (2004).

178 D. Erickson and D. Q. Li, "Integrated microfluidic devices," *Analytica Chimica Acta,* 507 11-26 (2004).

179 S. L. Zhang and S. J. Haswell, "Materials Matter in Microfluidic Devices," *Materials Research Society Bulletin,* 31 114-120 (2006).

180 A. Vasudev, A. Kaushik, K. Jones, and S. Bhansali, "Prospects of low temperature co-fired ceramic (LTCC) based microfluidic systems for point-of-care biosensing and environmental sensing," *Microfluidics and Nanofluidics,* 14 683-702 (2013).

181 D. F. Williams, "On the mechanisms of biocompatibility," *Biomaterials,* 29 2941-2953 (2008).

182 H. H. Su and D. L. Johnson, "Master sintering curve: A practical approach to sintering," *Journal of the American Ceramic Society,* 79 3211-3217 (1996).

183 S. J. Park, J. M. Martin, J. F. Guo, J. L. Johnson, and R. M. German, "Densification behavior of tungsten heavy alloy based on master sintering curve concept," *Metallurgical and Materials Transactions a-Physical Metallurgy and Materials Science,* 37A 2837-2848 (2006).

184 A. Mohanram, G. L. Messing, and D. J. Green, "Densification and sintering viscosity of low-temperature co-fired ceramics," *Journal of the American Ceramic Society,* 88 2681-2689 (2005).

185 W. B. Lim, Y. S. Cho, Y. J. Seo, and J. G. Park, "Shrinkage behavior of LTCC hetero-laminates," *Journal of the European Ceramic Society,* 29 711-716 (2009).

186 R. J. Xie, R. Z. Zuo, E. Aulbach, U. Mackens, N. Hirosaki, and H. Rodel, "Uniaxial viscosity of low-temperature cofired ceramic (LTCC) powder compacts determined by loading dilatometry," *Journal of the European Ceramic Society,* 25 417-424 (2005).

187 W. L. Zhang and R. E. Eitel, "Sintering Behavior, Properties, and Applications of Co-Fired Piezoelectric/Low Temperature Co-Fired Ceramic (PZT-SKN/LTCC) Multilayer Ceramics," *International Journal of Applied Ceramic Technology,* 10 354-364 (2013).

188 M. Liu, H. Q. Zhou, H. K. Zhu, Z. X. Yue, and J. X. Zhao, "Microstructure and dielectric properties of glass/Al2O3 composites with various low softening point borosilicate glasses," *Journal of Materials Science-Materials in Electronics,* 23 2130-2139 (2012).

189 H. K. Zhu, M. Liu, H. Q. Zhou, L. Q. Li, and A. Lv, "Study on properties of CaO-SiO2-B2O3 system glass-ceramic," *Materials Research Bulletin,* 42 1137-1144 (2007).

190 K. B. Shim, N. T. Cho, and S. W. Lee, "Silver diffusion and microstructure in LTCC multilayer couplers for high frequency applications," *Journal of Materials Science,* 35 813-820 (2000).

191 J. H. Jean and C. R. Chang, "Camber development during cofiring Ag-based low-dielectric-constant ceramic package," *Journal of Materials Research,* 12 2743-2750 (1997).

192 C. R. Chang and J. H. Jean, "Effects of silver-paste formulation on camber development during the cofiring of a silver-based, low-temperature-cofired ceramic package," *Journal of the American Ceramic Society,* 81 2805-2814 (1998).

193 Y. G. Wang, G. N. Zhang, and J. S. Ma, "Research of LTCC/Cu, Ag multilayer substrate in microelectronic packaging," *Materials Science and Engineering B-Solid State Materials for Advanced Technology,* 94 48-53 (2002).

194 R. L. Coble, "Sintering Crystalline Solids .1. Intermediate and Final State Diffusion Models," *Journal of Applied Physics,* 32 787-& (1961).

195 W. D. Kingery and M. Berg, "Study of the Initial Stages of Sintering Solids by Viscous Flow, Evaporation-Condensation, and Self-Diffusion," *Journal of Applied Physics,* 26 1205-1212 (1955).

196 D. L. Johnson, "New Method of Obtaining Volume Grain-Boundary and Surface Diffusion Coefficients from Sintering Data," *Journal of Applied Physics,* 40 192-& (1969).

197 H. H. Su and D. L. Johnson, "A practical approach to sintering," *American Ceramic Society Bulletin,* 76 72-76 (1997).

198 J. D. Hansen, R. P. Rusin, M. H. Teng, and D. L. Johnson, "Combined-Stage Sintering Model," *Journal of the American Ceramic Society,* 75 1129-1135 (1992).

199 D. C. Blaine, J. D. Gurosik, S. J. Park, D. F. Heaney, and R. M. German, "Master sintering curve concepts as applied to the sintering of molybdenum," *Metallurgical and Materials Transactions a-Physical Metallurgy and Materials Science,* 37A 715-720 (2006).

200 M. H. Teng, Y. C. Lai, and Y. T. Chen, "A program of master sintering curve model to accurately predict the sintering results," *Western Pacific Earth Sciences,* 2 171-180 (2002).

201 S. J. Park, J. M. Martin, J. F. Guo, J. L. Johnson, and R. M. German, "Grain growth behavior of tungsten heavy alloys based on the master sintering curve concept," *Metallurgical and Materials Transactions a-Physical Metallurgy and Materials Science,* 37A 3337-3346 (2006).

202 M. Mazaheri, A. Simchi, M. Dourandish, and F. Golestani-Fard, "Master sintering curves of a nanoscale 3Y-TZP powder compacts," *Ceramics International,* 35 547-554 (2009).
203 T. R. G. Kutty, K. B. Khan, P. V. Hegde, A. K. Sengupta, S. Majumdar, and H. S. Kamath, "Determination of activation energy of sintering of ThO2-U3O8 pellets using the master sintering curve approach," *Science of Sintering,* 35 125-132 (2003).
204 K. G. Ewsuk, D. T. Ellerby, and C. B. DiAntonio, "Analysis of nanocrystalline and microcrystalline ZnO sintering using master sintering curves," *Journal of the American Ceramic Society,* 89 2003-2009 (2006).
205 T. W. Chung, D. Z. Liu, S. Y. Wang, and S. S. Wang, "Enhancement of the growth of human endothelial cells by surface roughness at nanometer scale," *Biomaterials,* 24 4655-4661 (2003).
206 R. I. Dmitriev, A. V. Zhdanov, G. Jasionek, and D. B. Papkovsky, "Assessment of Cellular Oxygen Gradients with a Panel of Phosphorescent Oxygen-Sensitive Probes," *Analytical Chemistry,* 84 2930-2938 (2012).
207 A. A. Gerencser, A. Neilson, S. W. Choi, U. Edman, N. Yadava, R. J. Oh, D. A. Ferrick, D. G. Nicholls, and M. D. Brand, "Quantitative Microplate-Based Respirometry with Correction for Oxygen Diffusion," *Analytical Chemistry,* 81 6868-6878 (2009).
208 D. A. Chang-Yen and B. K. Gale, "An integrated optical oxygen sensor fabricated using rapid-prototyping techniques," *Lab on a Chip,* 3 297-301 (2003).
209 P. Mestres and A. Morguet, "The Bionas technology for anticancer drug screening," *Expert Opinion on Drug Discovery,* 4 785-797 (2009).
210 G. Mehta, K. Mehta, D. Sud, J. W. Song, T. Bersano-Begey, N. Futai, Y. S. Heo, M. A. Mycek, J. J. Linderman, and S. Takayama, "Quantitative measurement and control of oxygen levels in microfluidic poly(dimethylsiloxane) bioreactors during cell culture," *Biomedical Microdevices,* 9 123-134 (2007).
211 T. Rabe, W. A. Schiller, T. Hochheimer, C. Modes, and A. Kipka, "Zero shrinkage of LTCC by self-constrained sintering," *International Journal of Applied Ceramic Technology,* 2 374-382 (2005).
212 F. Lautzenhiser and E. Amaya, "Self-constrained LTCC tape," *American Ceramic Society Bulletin,* 81 27-32 (2002).
213 A. Mohanram, S. H. Lee, G. L. Messing, and D. J. Green, "Constrained sintering of low-temperature co-fired ceramics," *Journal of the American Ceramic Society,* 89 1923-1929 (2006).
214 J. B. Ollagnier, O. Guillon, and J. Rodel, "Constrained Sintering of a Glass Ceramic Composite: I. Asymmetric Laminate," *Journal of the American Ceramic Society,* 93 74-81 (2010).
215 J. B. Ollagnier, D. J. Green, O. Guillon, and J. Rodel, "Constrained Sintering of a Glass Ceramic Composite: II. Symmetric Laminate," *Journal of the American Ceramic Society,* 92 2900-2906 (2009).
216 C. C. Huang and J. H. Jean, "Stress required for constrained sintering of a ceramic-filled glass composite," *Journal of the American Ceramic Society,* 87 1454-1458 (2004).

217 K. A. Mauritz and R. B. Moore, "State of understanding of Nafion," *Chemical Reviews*, 104 4535-4585 (2004).
218 K. Hongsirikarn, J. G. Goodwin, S. Greenway, and S. Creager, "Effect of cations (Na+, Ca2+, Fe3+) on the conductivity of a Nafion membrane," *Journal of Power Sources*, 195 7213-7220 (2010).
219 A. T. Haug and R. E. White, "Oxygen diffusion coefficient and solubility in a new proton exchange membrane," *Journal of the Electrochemical Society*, 147 980-983 (2000).
220 M. E. Cox and B. Dunn, "Oxygen Diffusion in Poly(Dimethyl Siloxane) Using Fluorescence Quenching .1. Measurement Technique and Analysis," *Journal of Polymer Science Part a-Polymer Chemistry*, 24 621-636 (1986).
221 B. J. Polk, A. Stelzenmuller, G. Mijares, W. MacCrehan, and M. Gaitan, "Ag/AgCl microelectrodes with improved stability for microfluidics," *Sensors and Actuators B-Chemical*, 114 239-247 (2006).
222 T. Matsumoto, A. Ohashi, and N. Ito, "Development of a micro-planar Ag/AgCl quasi-reference electrode with long-term stability for an amperometric glucose sensor," *Analytica Chimica Acta*, 462 253-259 (2002).
223 F. Moussy and D. J. Harrison, "Prevention of the Rapid Degradation of Subcutaneously Implanted Ag/Agcl Reference Electrodes Using Polymer-Coatings," *Analytical Chemistry*, 66 674-679 (1994).
224 P. Stoor, E. Soderling, and J. I. Salonen, "Antibacterial effects of a bioactive glass paste on oral microorganisms," *Acta Odontologica Scandinavica*, 56 161-165 (1998).
225 H. Forss, "Release of Fluoride and Other Elements from Light-Cured Glass Ionomers in Neutral and Acidic Conditions," *Journal of Dental Research*, 72 1257-1262 (1993).

Vita

Name: Jin Luo Place of Birth: Chenzhou, Hunan, China

Education

- Ph.D. candidate, Materials Science and Engineering
  University of Kentucky, Lexington, KY, August 2010 – August 2014
- Master of Engineering, Materials Science and Engineering
  Zhejiang University, Hangzhou, Zhejiang, China, 2009
- Bachelor of Engineering, Materials Chemistry
  Wuhan University of Technology, Wuhan, Hubei, China, 2006

Honors and Awards

- Graduate poster contest winner at MS&T'11 conference, 2011
- USEC Inc. Graduate Fellowship, 2011
- Kentucky Opportunity Fellowship, 2010
- Outstanding M.S. thesis of Zhejiang Province, 2009
- Outstanding Graduate of Wuhan University of Technology, 2006
- Excellent Study Scholarship, 2005, 2004, 2003
- National Excellent Scholarship, 2004

Publications and Proceedings

1. **J. Luo** and R. E. Eitel, "A low temperature co-fired ceramic (LTCC) microfluidic Clark-type oxygen sensor for real-time oxygen sensing", **in preparation**.
2. **J. Luo** and R. E. Eitel, "Densification, compatibility with electrode and biocompatibility of a low temperature co-fired ceramic", **in preparation**.
3. **J. Luo** and R. E. Eitel, "A biocompatible low temperature co-fired ceramic substrate for biosensor", ***International Journal of Applied Ceramic Technology,*** DOI: 10.1111/ijac.12206.
4. **J. Luo** and R. E. Eitel, "Biocompatible low temperature co-fired ceramic for biosensors", ***IMAPS/ACerS 9th International Conference and Exhibition on Ceramic Interconnect and Ceramic Microsystems Technologies (CICMT2013) proceeding***, Orlando, Florida, 183-186, 2013
5. **J. Luo**, S. Zhou, B. Wu, H. Yang, S. Ye, B. Zhu and J. Qiu "Greatly enhanced broadband near-infrared emission due to energy transfer from Cr^{3+} to Ni^{2+} in

transparent magnesium aluminosilicate glass ceramics" ***Journal of Materials Research***, 24, 310, 2009

6. **J. Luo**, B. Wu, B. Zhu, S. Zhou, H. Yang, S. Ye, G. Lakshminarayana and J. Qiu "Energy transfer between Cr^{3+} and Ni^{2+} in transparent glass-ceramics containing β-Ga_2O_3 nanocrystals" ***Journal of Applied Physics***, 106, 053527, 2009
7. Y. Zhuang, **J. Luo**, Y. Teng, S. Ye, B. Zhu, and J. Qiu, "Broadband infrared luminescence of Cr^{3+}-doped $LiInSiO_4$ phosphors", ***Journal of Materials Research***, 24, 310, 2009
8. Y. Zhuang, Y. Teng, **J. Luo**, B. Zhu, Y. Chi, E Wu, H. Zeng, and J. Qiu, "Broadband optical amplification in silicate glass ceramics containing Li_2ZnSiO_4: Cr^{4+} nanocrystals", ***Applied Physics Letters***, 95, 111913, 2009
9. S. Ye, B. Zhu, **J. Luo**, Y. Teng, J. Chen, G. Lakshminarayana, G. Qian and J. Qiu "Energy transfer between silicon-oxygen-related defects and Yb^{3+} in transparent glass ceramics containing $Ba_2TiSi_2O_8$ nanocrystals" ***Applied Physics Letters***, 93, 181110, 2008
10. S. Ye, B. Zhu, **J. Luo**, J. Chen, G. Lakshminarayana, and J. Qiu "Enhanced cooperative quantum cutting in Tm^{3+}-Yb^{3+} codoped glass ceramics containing LaF_3 nanocrystals" ***Optics Express***, 16, 8989, 2008
11. S. Ye, B. Zhu, J. Chen, **J. Luo**, and J. Qiu "Infrared quantum cutting in Tb^{3+},Yb^{3+} codoped transparent glass ceramics containing CaF_2 nanocrystals" ***Applied Physics Letters***, 92, 141112, 2008

Conference presentations and posters

1. **J. Luo** and R. E. Eitel, "Biocompatible low temperature co-fired ceramic for biosensors", *IMAPS/ACerS 9th International Conference and Exhibition on Ceramic Interconnect and Ceramic Microsystems Technologies (CICMT2013)*, Orlando, Florida, 2013. (Presentation and Poster)
2. **J. Luo** and R. E. Eitel: "Biocompatible multilayer co-fired ceramic for biomedical lab on chip applications", *Biomaterials Day*, Lexington, KY, 2012. (Poster)
3. **J. Luo** and R. E. Eitel, "Integration of a microfluidic oxygen sensor into LTCC for in-vitro diagnostics," *Materials Science & Technology 2011 (MS&T 2011) Conference & Exhibition*, Columbus, OH, 2011. (Poster)